UNIVERSIDADE FEDERAL DE SANTA CATARINA
PROGRAMA DE PÓS-GRADUAÇÃO EM
ENGENHARIA MECÂNICA

LOURIVAL JORGE MENDES NETO

ANÁLISE DA DEPOSIÇÃO, CRESCIMENTO E TRANSFERÊNCIA DE CALOR EM DEPÓSITOS DE CINZAS EM TUBOS CILÍNDRICOS

Florianópolis, Março de 2010

UNIVERSIDADE FEDERAL DE SANTA CATARINA
PROGRAMA DE PÓS-GRADUAÇÃO EM
ENGENHARIA MECÂNICA

ANÁLISE DA DEPOSIÇÃO, CRESCIMENTO E TRANSFERÊNCIA DE CALOR EM DEPÓSITOS DE CINZAS EM TUBOS CILÍNDRICOS

Tese submetida à

UNIVERSIDADE FEDERAL DE SANTA CATARINA

para a obtenção do grau de

DOUTOR EM ENGENHARIA MECÂNICA

LOURIVAL JORGE MENDES NETO

Florianópolis, Março de 2010

Catalogação na fonte pela Biblioteca Universitária da
Universidade Federal de Santa Catarina

M534a Mendes Neto, Lourival Jorge
Análise da deposição, crescimento e transferência de calor em depósitos de cinzas em tubos cilíndricos [tese] / Lourival Jorge Mendes Neto; orientador, Edson Bazzo. – Florianópolis, SC, 2010.
138 p.: grafs., tabs.

Tese (doutorado) – Universidade Federal de Santa Catarina, Centro Tecnológico. Programa de Pós-Graduação em Engenharia Mecânica.

Inclui referências

1. Engenharia mecânica. 2. Caldeiras. 3. Depósito de cinzas. 4. Microscopia eletrônica de varredura. 5. Dimensão fractal. 6. Transferência de calor. I. Bazzo, Edson. II. Universidade Federal de Santa Catarina. Programa de Pós-Graduação em Engenharia Mecânica. III. Título.

CDU 621

UNIVERSIDADE FEDERAL DE SANTA CATARINA
PROGRAMA DE PÓS-GRADUAÇÃO EM
ENGENHARIA MECÂNICA

ANÁLISE DA DEPOSIÇÃO, CRESCIMENTO E TRANSFERÊNCIA DE CALOR EM DEPÓSITOS DE CINZAS EM TUBOS CILÍNDRICOS

LOURIVAL JORGE MENDES NETO

Esta tese foi julgada adequada para a obtenção do título de

DOUTOR EM ENGENHARIA

ESPECIALIDADE ENGENHARIA MECÂNICA
sendo aprovada em sua forma final.

Edson Bazzo, Dr. Eng. – Orientador.

Eduardo Alberto Fancello, Dr. Sc. – Coordenador do Curso.

BANCA EXAMINADORA

Edson Bazzo, Dr. Eng. – (Presidente).

Fernando E. Milioli, Ph.D. – Relator.

Carlos A. Gurgel Veras, Dr. Eng.

Amir A. M. Oliveira Jr, Ph.D.

Cesar José Deschamps, Ph.D.

Aos meus pais Lourival e Ivonete.
Aos meus irmãos Leandro e Theodora.
À minha amada esposa Érica.

AGRADECIMENTOS

Felizmente tive a sorte de contar com diversos amigos durante o desenvolvimento deste trabalho, porém, infelizmente, será impossível agradecer a todos. Entretanto, há algumas pessoas das quais não posso deixar de agradecer. Dentre elas meu orientador e amigo professor Edson Bazzo, que sem a enorme ajuda e dedicação eu não poderia ter desenvolvido este doutorado, muito obrigado pelo apoio e incentivo no tema que tanto discutimos.

Também não posso deixar de agradecer ao professor Wagner Figueiredo do departamento de Física/UFSC pelo excelente apoio no desenvolvimento e discussão dos modelos de crescimento de superfície, bem como ao professor Celso Fernandes, LMPT/UFSC, pela enorme ajuda no desenvolvimento da caracterização das estruturas porosas, ao professor Amir Oliveira, LabCet/UFSC, pelas excelentes discussões sobre transferência de calor e ao professor Felix Sharipov do departamento de Física da UFPR pelas discussões sobre condições de contorno modificadas.

Parte deste trabalho foi desenvolvida no Instituto Superior Técnico em Lisboa, Portugal, do qual tive todo apoio no caminhar da tese e aonde tive o prazer de ser orientado pelo amigo e professor João Toste de Azevedo, muito obrigado pelas excelentes discussões técnicas e apoio durante a minha estadia em Portugal.

Agradeço também aos meus amigos do LabCet que tanto me ajudaram nas dúvidas e questionamentos, tanto técnicos quanto pessoais, da mesma forma aos meus amigos do IST que me apoiaram na dificuldade da língua de Camões.

Agradeço também à Tractebel Energia S.A. pela ajuda em desenvolver parte do trabalho na caldeira de Jorge Lacerda em Capivari de Baixo, SC. Em especial, quero agradecer ao engenheiro Luiz Felippe por acreditar no desenvolvimento do trabalho e no apoio essencial nas coletas e análise das amostras.

Ao Departamento de Engenharia Mecânica e ao Programa de Pós Graduação em Engenharia Mecânica pelo acesso aos professores de excelente qualidade e ao CNPq pelo suporte financeiro, sem o qual não seria possível realizar este trabalho.

Viver, e não ter a vergonha de ser feliz
Cantar e cantar e cantar
A beleza de ser um eterno aprendiz
Ah meu Deus eu sei, eu sei
Que a vida devia ser bem melhor e será.
(Gonzaguinha, O que é o que é, 1982)

RESUMO

A crescente demanda por combustíveis alternativos vem aumentando em grande parte devido às exigências de uma tecnologia de geração de energia limpa com menores emissões de gases de efeito estufa, como no caso do CO_2. Porém o aumento da eficiência de equipamentos que utilizem combustíveis fósseis minimiza a emissão de gases de efeito estufa ao mesmo tempo em que aumenta a disponibilidade de energia. Dentre estes equipamentos a caldeira de carvão pulverizado é o equipamento mais comum na geração termelétrica

A queima de carvão pulverizado em caldeiras apresenta diversos desafios, dentre eles a deposição de cinzas, que isola os tubos de troca de calor diminuindo a eficiência do equipamento, aumentando o consumo de carvão e conseqüentemente a emissão de CO_2. Visando avaliar a influência do depósito de cinza na eficiência da caldeira, este trabalho apresenta um estudo dos mecanismos envolvidos na deposição de partículas de cinza, crescimento e transferência de calor no depósito de cinza. O objetivo do presente trabalho é apresentar os mecanismos de deposição de cinzas em um tubo do superaquecedor e, em seguida, desenvolver um modelo de crescimento do depósito e avaliar a transferência de calor na estrutura gerada pelo modelo de deposição.

Isto será feito via técnica de mecânica dos fluidos computacional (CFD – *Computer Fluid Dynamics*), utilizando simulações de grandes escalas. Os mecanismos macros, como o transporte de partículas, via abordagem Lagrangeana, são resolvidos para um tubo representativo dos superaquecedores, visando avaliar a distribuição de partículas ao redor do mesmo. Além disso, um modelo foi desenvolvido baseado no conceito de crescimento de superfície e os resultados gerados por estes modelos foram comparados com um típico depósito da caldeira de Jorge Lacerda, Capivari de Baixo, SC, via microscópio eletrônico de varredura. O modelo proposto apresentou bons resultados quando comparados com as características macros tais como porosidade e dimensões fractais, mas deve ser melhorado quando analisada a distribuição de tamanho de poro.

A estrutura gerada pelo modelo proposto foi avaliada via código TEACH C modificado, visando avaliar os efeitos de rarefação. Dessa forma, uma nova correlação é proposta entre porosidade e condutividade térmica efetiva baseada na estrutura gerada pelo modelo de crescimento apresentando bons resultados.

Palavras-chave: Caldeira, Depósito de Cinzas, Simulação de Grandes Escalas, Microscópio Eletrônico de Varredura, Dimensão Fractal, Transferência de Calor.

ABSTRACT

The growing demand for renewable fuel is mostly due to the strict requirements for a clean technology with low greenhouse gas emission effect, as with CO_2. Besides raising the efficiency of equipment that uses fossil fuel also helps reduce the harmful greenhouse effect of gas emissions while offering more energy. Among several alternatives, the pulverized coal boiler is the most commonly used equipment for energy conversion of solid fuels in thermal generation.

The burning of pulverized coal presents several challenges, including the ash deposition that isolates the heat transfer tubes, thus lowering the equipment efficiency, raising the coal consumption and consequently the CO_2 emission. Aiming at evaluating the influence of the ash deposit on equipment efficiency, this work presents a study of the mechanisms involved in the ash particles deposition, growing and heat transfer on ash deposits. The objective of the present work is to present the mechanisms involved in particle deposition, to develop a growing model of the ash deposit and evaluate the heat transfer on the porous structure generated by the model developed.

The computer fluid dynamics technique (CFD) was used in conjunction with Large Eddy Simulation, and the macro mechanisms, as the ash particles transportation via Lagrangean approach, are solved for a representative tube of the superheaters in order to evaluate the particle distribution around one tube of the tube bundle. A model has also been developed based on the concepts of surface growing. The results generated by this model are compared with a typical ash deposit from the Jorge Lacerda thermal power plant, Capivari de Baixo, SC, via scanning electron microscopy. The model proposed here shows good results when compared to the macro quantities such as porosity and fractal dimension. However, when the pore size distribution is analyzed it indicates a need for improvement.

The structure generated by the ash deposition model was evaluated via the modified TEACH C code in order to evaluate the rarefaction effects. A new relation between porosity and effective thermal conductivity is proposed, based on the structures generated by the model developed here with good results.

Key words: Boiler, Ash Deposit, Large Eddy Simulation, Scanning Electron Microscope, Fractal Dimension, Heat Transfer.

LIST OF FIGURES

LIST OF TABLES

NOMENCLATURE

Latin letters

A+	van Driest constant	[-]
A	Area	[m^2]
Bi	Biot Number	[-]
C	Constant on Eq. 4.2	[-]
C_D	Drag Coefficient	[-]
C_{Pb}	Back Pressure Coefficient	[-]
C_f	Skin Friction Coefficient	[-]
C_S	Smagorinsky Constant	[-]
C(u)	Covariogram	[-]
d	Distance to the Closest Wall or Molecular Mean Diameter	[m]
d_{3-4}	Metric Defined in Section 3.4	[-]
D	Cylinder Diameter or Dimension	[m, -]
E	Constant in Eq. 2.16	[-]
F	Force in the equation for the particle motion	[N]
F	View Factor in Eq. 4.4	[-]
g	Gravity	[m/s^2]
$G(\mathbf{r})$	LES Filter Function	[-]
$\hat{G}(\kappa)$	Transfer Function	[-]
h	Height of the Surface	[m]
k	Thermal Conductivity	[W/m/K]
Kn	Knudsen Number	[-]
K_{th}	Thermophoretic Coefficient	[$m^2/s/K$]
l	Characteristic Scale	[m]
l1	Height of the First cell at the Cylinder Surface	[m]
L_{ij}	Germano's Identity or Resolved Stress	[m^2/s^2]
L_r	Recirculation Length	[m]
L	Length of Strings or Characteristic Length	[m]
m	Mass or Constant in Eq. 4.2	[kg or -]
M	Molecular Mass of the Gas	[kg/kmol]
n	Constant in Eq. 4.2	[-]
N	Total Number of Particles	[-]
N_A	Avogadro Constant	[-]
N_d	Number of Particles Deposited on the Wall	[-]
Nu	Nusselt Number	[-]

p	Pressure	[Pa]
Pr	Prandtl Number	[-]
q	Heat Flux	[W/m^2]
Q	Heat Rate	[W]
r	Radius	[m]
R	Thermal Resistance	[K/W]
$\overline{R}$	Universal Gas Constant	[-]
Re	Reynolds Number	[-]
St	Stokes Number	[-]
$\overline{S}_{ij}$	Filtered Rate of Strain	[1/s]
t	Time	[s]
T	Temperature	[ºC or K]
u	Displacement of Image	[pixels]
U	Velocity Vector	[m/s]
U_0	Free Stream Velocity	[m/s]
V	Volume	[m^3]
V_d	Particle Deposition Rate or Deposition Velocity	[m/s]
w	Interface Width	[m]
x	Position Vector	[m]
y+	Distance from the Wall Normalized by the Viscous Length Scale	[-]
z	Dynamic Exponent	[-]

Greek letters

α	Absorptivity or Roughness Exponent	[-]
β	Growth Exponent	[-]
δ_{ij}	Kronecker Delta	[-]
Δ	Filter Width	
Δt	Time Step	[s]
$\Delta\varepsilon$	Correction Factor, Eq 4.9	[-]
ε	Emissivity	[-]
ζ_T	Temperature Jump Coefficient	[-]
κ	Wavenumber or von Kármán Constant	[-]
κ_B	Boltzmann Constant	[-]
κ_C	Filter Cut Off Wavenumber	[-]
κ_{vK}	von Kármán Constant	[-]
λ	Taylor Microscale or Mean Free Path	[m, Å]
λ_L	Quantity of Order of Mean Free Path	[m]
μ	Viscosity	[kg/m/s]
ν	Kinematic Viscosity	[m^2/s]

ν_0	Most Probable Molecular Velocity	[m/s]
ρ	Density / Reflectivity	[kg/m^3] /[-]
τ	Tortuosity	[-]
τ_p	Particle Response Time Particle Relaxation Time	[s]
τ_F	Time Characteristic of Fluid Motion	[s]
τ_w	Wall Shear Stress	[Pa]
τ_{ij}^R	Residual Stress Tensor (SGS)	[m^2/s^2]
τ_{ij}^r	Anisotropic Residual Stress Tensor (SGS)	[m^2/s^2]
ϕ	Porosity	[-]
ω	Vorticity	[1/s]

Superscript

$\bar{\mathbf{U}}$	Filtered Quantity (Filter Width Δ or Grid Filter) or Mean Quantity
$\overline{AB}$	Straight Line between points A and B
$\overset{\frown}{BC}$	Arc Segment between points B and C
$\tilde{\mathbf{U}}$	Filtered Quantity (Filter Width $\tilde{\Delta}$ or Test Filter)
$\mathbf{u}'$	Residual Quantity from Filtering Operation
*	Dimensionless Quantity

Subscript

c	Carbon Dioxide
cond	Conduction
cross	Sum of the Length of the Cross String
d	Deposit
D	Drag
ec	External Convection
eff	Effectiveness
eq	Equivalent
erad	Emitted Radiation
E	Embedded
f	Fractal
g	Gas
H	Hydrodynamic Regime
irad	Incident Radiation
iplane	Average Irradiation from the Inlet Plane
min	Minimum

max	Maximum
p	Inlet Plane
P	Particle
rerad	Reflected Radiation
R	Rarefaction Regime
RP	Rayleigh Model considering the deposit as a particulate cluster
RS	Rayleigh Model considering the deposit as a slag
s	Surface / Solid Phase
t	Tube
uncrossed	Sum of the Length of the Uncrossed String
x	Crossover
w	Water Vapor or Wall
λ	Spectral

Acronyms

ANEEL	Brazilian Electricity Regulatory Agency
BBO	Basset-Boussinesq-Oseen
BD	Ballistic Deposition
BEI	Back Scattered Electron Imaging
CBC	Convection Boundedness Criterion
CDS	Central Differencing Scheme
CFD	Computer Fluid Dynamic
CPU	Central Processing Unit
DNS	Direct Numerical Simulation
EDX	Energy Dispersive X-ray
FSM	Fractional Step Method
HLPA	Hybrid Linear/Parabolic Approximation
IEA	International Energy Agency
LCM	Microstructure Characterization Laboratory
LES	Large Eddy Simulation
LES-NWM	Large Eddy Simulation with Near Wall Modeling
LES-NWR	Large Eddy Simulation with Near Wall Resolution
LMPT	Laboratory of Physical Properties and Porous Material
MIT	Massachusetts Institute of Technology
NITA	Non Iterative Time Advanced Scheme
NSE	Navier Stokes Equations
NVD	Normalized Variable Diagram
PRESTO	PreREssure STaggering Option
RANS	Reynolds Average Navier Stokes
RD	Random Deposition
SEM	Scanning Electronic Microscopy
SGS	SubGrid Scale
UFSC	Federal University of Santa Catarina

TOE	Tonne of Oil Equivalent
TPE	Tonne Petroleum Equivalent
XRD	X-ray Diffraction

SUMMARY

CHAPTER 1 - INTRODUCTION

1.1 Motivation.

The economic growth of a country is mostly based on a reliable and affordable energy supply. The energy available must meet the country's demand. It must also be efficient and follow environmental and social requisites for sustainability. Nowadays, high efficiency and environmental impact add to another challenge, the planet warming. This is a huge challenge since 80% of the world's energy demand is fulfilled by fossil fuels, IEA (2008) which are considered the main sources for the CO_2 emissions, causing anthropogenic greenhouse effects.

Today, the world's fossil fuel consumption is divided into 26% coal, 34% oil and 20% natural gas. This scenario describes how dependent on fossil fuel the world energy is, and how difficult it will be to reduce this dependency in favor of renewable energy. According to a recent study about the future of coal, MIT (2007), there are five broad options for reducing carbon emissions from combustion of fossil fuel:

- Improvements in the efficiency of energy use, specially transportation and electricity generation;
- Increased use of renewable energy such as wind, solar and biomass;
- Expanded electricity production from nuclear energy;
- Switching to less carbon intensive fossil fuel;
- Continued combustion of fossil fuels, especially coal, combined with CO_2 capture and storage.

Improvement of energy use is the most direct action to reduce fuel consumption. The estimated reduction in energy consumption due to the application of efficiency measures in the USA is estimated to be close to 10%, MIT (2007). However, they require, besides the replacement of old hardware and appliances, a change in the users' habits and use of energy. This change is bound to take a few generations. In the short run, the rational use of the available fossil fuels will provide the energy buffer required for a smooth transition to more sustainable energy sources and uses. The use of coal is believed to increase in any foreseeable scenario because it is cheap and abundant. According to the MIT study, MIT (2007), in the USA, coal can provide usable energy at a cost ranging from 1$ to 2$ per MMBtu (43$ to 86$

per tpe) compared to 6$ to 12$ per MMBtu (257$ to 514$ per tpe) for oil and gas. Also, coal is found all over the world, which is not true for oil and gas. In addition, according to the International Energy Agency (IEA), Fig 1.1, the expected world energy growth demand will expand by 45% between 2008 and 2030 with an average increase of 1.6% per year, with coal accounting for more than one third of the overall rise, IEA (2009).

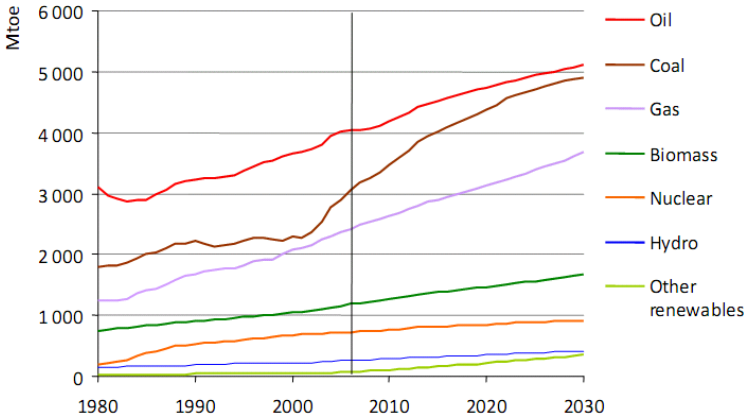

Figure 1.1 – World energy demand from 1980 to 2030, IEA (2009). (1 toe = 1.07 tep = 42 GJ).

The main disadvantages of coal are the environmentally adverse effects of its mining, transportation, storage and combustion. Coal combustion results in higher CO_2 emission than the energy generated from natural gas (per unity of power output). Besides, coal is not a pure material, its composition, structure and properties differ considerably among mining locations, which has a great influence in the coal combustion process.

Differently from most other countries, the main energy source in Brazil comes from hydro power. According to ANEEL (2008), 73% of the electrical energy generated in Brazil is hydraulic, the rest is generated mostly by thermal plants (about 22%). Still according to ANEEL (2008) the new power plants under construction with government authorization, should change this energy matrix scenario by raising the thermal power plants to 35%. Also, 35% of the thermal power plants planned are coal based. Coal is expected to become a real important energy source.

The use of coal as an energy source via combustion implies several difficulties. Besides the environmental problems related to coal mining, processing, storage and emissions, the efficiency and availability of the boiler is strongly affected by the coal composition. According to Reinaldo *et al* (2005), boiler tube failures cause about 40% of the unplanned outages in a coal fired utility. About 50% of failures in superheaters and reheaters tubes are due to creep strain at high temperatures resulting from poor boiler design and operation at off-design conditions. Most of the off-design conditions are caused by changes in coal composition when compared to the coal rank used in the design stage. For instance, the Jorge Lacerda thermo power plant, located at Capivarí de Baixo, Santa Catarina State (SC), south of Brazil, suffers with the high ash content from this State's coal. The weight content of the Brazilian coal used in the Jorge Lacerda boiler is, approximately, 40% ash. This high content causes severe deposition of ash on the heat transfer surfaces. This creates preferential ways, changing the flow field and consequently lowering the heat transfer to the steam due to the insulation effects of the ash deposit.

Taking the importance of coal to satisfy near future energy needs into consideration, this work addresses one of the difficulties encountered when burning high ash coals, which is the effect of coal deposition into the external heat transfer surfaces in boiler tubes. Therefore, three aspects will be addressed: (1) The ash deposition in boiler tube surfaces, (2) The growth of the ash deposit and (3) The heat transfer across the ash deposit. This information will then be incorporated into a global heat transfer model to estimate the efficiency decrease due to the ash deposits in the tubes of the superheater bank of a typical pulverized coal fired boiler. The methodologies developed here can be used, in future works, in coal boiler design, analysis and optimization. Data obtained from the Jorge Lacerda Power Plant in Brazil will be used to provide conditions and to validate some aspects of this work.

1.2 Description of the problem

The vaporization of inorganic elements, coalescence of particles, nucleation, coagulation and condensation are the main mechanisms involved in the formation of ash from the burning of coal. Figure 1.2 presents a rendering of the accepted mechanism for ash formation from coal (Knudsen, 2001). Inorganic elements are dispersed in the coal matrix. Some of them are considered included in the carbon matrix. They can react and evaporate in aggressive conditions forming

condensable vapors. Other elements can be considered as excluded elements of the carbon matrix. They form fragmented particles on which the vapors condensate or melt, creating potentially adherent particles, reaching the tube. This particle formation mechanism, according to Knudsen (2001), generates a bimodal distribution of ash size, with particle sizes ranging mostly from 0.1 to 20 μm.

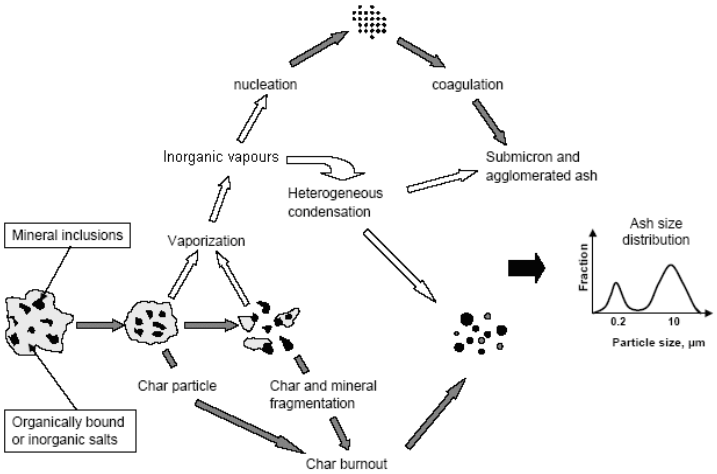

Figure 1.2 – Schematic illustration of ash developing, from Knudsen (2001).

These particles are carried by the hot flue gases. Along the way in the boiler they may suffer coalescence or break-up, depending on the particles mineralogy and flow temperature. Eventually, a reasonable concentration of the ash particles, commonly denominated as fly-ash, reaches the tube bundles in the steam superheating section. There, these particles may hit and adhere to the tube surfaces.

Many mechanisms are identified for the deposition of ash particles (Baxter, 1993; Knudsen, 2001). The most important are: condensation of inorganic vapors, thermophoresis eddy diffusion and inertial impact. Condensation has a major effect on the submicron particles and will not be addressed here, since only particles above 1 μm will be considered. The thermophoresis and inertial impact mechanisms are responsible for taking the particles from the particle-laden flow to the tube surface. Figure 1.3 presents a steam tube covered by a layer of deposited ash. At the bottom of the figure, there is a rendering of the normal temperature distribution from the tube surface. The direction of the particle motion is presented with a rendering of the relative particle

sizes affected by each mechanism. The heat transfer rates by convection and radiation are also shown.

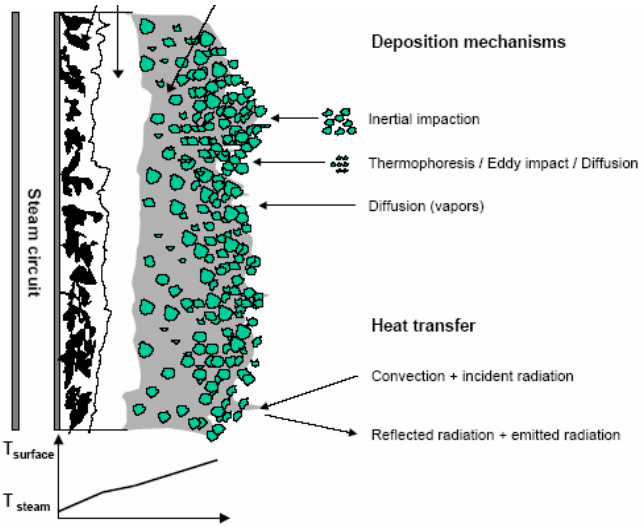

Figure 1.3 – Conceptual illustration of the structure, heat and mass transfer in the deposit on superheat tube of the boiler, Knudsen (2001).

After the impact of the particles against the surface, they may stick there, which results in adherence as an ash deposit. The deposit grows at a rate proportional to the amount of adherent particles that impact the surface. The layer thickness can span distances larger than the tube diameter and eventually total flow blockage of the tube bank may occur.

Two different theoretical treatments for the prediction of the formation of deposits can be identified. First, the particle-laden dynamics in a homogeneous fluid treats the fluid as a continuum media with a dense phase. Secondly, after particles are deposited or close to the deposit the theoretical approach considers the discrete dynamics of particles. In this work, a discrete particle model will be developed and applied to the formation of ash deposits.

In the discrete particle model, the growing surfaces can be described through the Growing Surfaces Theory, following Barabási (1995). The dynamics of growing surfaces can describe the movement of the interface between the deposit and the flow using a fractal theory. The morphology of the deposit depends on how it is formed. Many

models are available to match the forming dynamics, such as, random deposition, random deposition with diffusion, ballistic deposition, ballistic deposition with diffusion, and Eden models. Figure 1.4 shows a section pattern of a deposit of particles simulated by Dobrescu and Rusu (2002) through the use of the dynamics of growing surfaces theory, using a ballistic model.

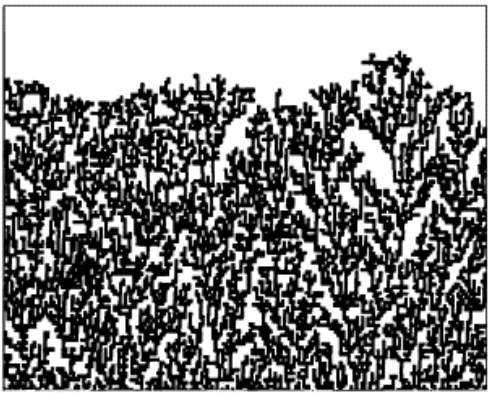

Figure 1.4 – Simulated deposit of monodisperse suspensions, Dobrescu and Rusu (2002).

The porous structure resulting from the deposition and growth affects the effective thermal conductivity of the ash layer which results in an additional thermal resistance between the steam and the boiler environment. This thermal resistance, therefore, changes with time and depends on all the flow, heat transfer, capture, adherence and growth parameters.

Several approaches can be used to describe the heat transfer in ash deposits, a simple analysis is done by Baxter (1998) describing the influence of tortuosity and porosity of the ash deposit in the heat transfer. A similar procedure will be used in this work, but will be complemented with an analysis of the heat transfer through the porous structure of the ash deposit. Zhogar *et al* (2005) also presented a review of the heat transfer in ash deposit with focus on the packed bed models.

Zhogar *et al* (2005) divided the thermal conductivity models into two main groups according to the handling of radiative effects on the system: unity cell models and pseudo homogeneous models. The unity cell models treat radiation as a local effect taking place between adjacent particle surfaces and void boundary surfaces in the unity cell, and neglect the long range effects of radiation. In general, this is done

by adding a radiative conductivity as a resistance in the network of resistances and a packed bed of sphere particles with known properties such as air-glass or alumina-air is assumed. The pseudo homogeneous models consider the packed bed to be continuum for a radiation, but for this approach the radiative properties are required. No further analysis is made here concerning the radiation in the porous structure. This was left for a future work.

Concerning the conductivity models of the packed bed presented by Zhogar *et al* (2005), in general, the models have a simplified approach to the structure system and, thus, can be applied only when one phase is continuous and the other is discontinuous.

Finally, the thermal resistance created by the ash deposit decreases the heat transfer from the hot flue gases to the steam flowing inside the tube, which causes an impact on the boiler's efficiency. A proper design of the boiler should avoid conditions that lead to excessive ash deposit formation. Nevertheless, the predictive capability of a model to evaluate the resistance imposed by the ash deposit can be used to analyze a given power plant and predict the intervals at which to stop and do cleaning. This would aid in the energy production planning.

1.3 Bibliographic Review of Ash Deposition Models

The ash deposit formation is usually described via the CFD of the boiler with a model coupled to the particles which calculates the probability of the sticking particles. Fan *et al* (2001) describe the ash deposition behavior in a pulverized coal fired boiler with a Lagrangian/Eulerian approach for the solid gas two phase flow. In order to simulate correctly the deposition of the particles, saving mesh and CPU memory, a post processor was added to calculate the particle impaction rates. In this model, the influence of the turbulent velocity fluctuations was assumed to be isotropic. In the gas phase, the particle trajectories were accounted for through random particle eddy interactions.

Huang *et al* (1996) described the ash deposition as a cumulative effect of the thermophoretic and inertial impaction. The inertial model is considered a function of the total mass flux of the ash particle and the fraction captured once collision on the surface has occurred. The impact efficiency was calculated considering the balance between the inertial and drag forces via Stokes number. Once impacted, the colliding particle actually sticks or rebounds according to a sticking probability based on the particle viscosity. The particle viscosity is calculated according to

the ash composition of the ash and is compared with a critical viscosity, 10^4 Pa s.

Huang *et al* (1996) coupled the deposition model with the FLUENT in order to simulate the ash deposition in a drop tube furnace and there were some discrepancies between CFD and the experimental work when non-fouling coal was considered. They occurred due to the shedding of the ash layer formed on the heat transfer surfaces. A similar approach is also considered by Lee and Lockwood (1999).

The particle sticking model described by Fan *et al* (2001) is based on the particle temperature and composition, similar to the Huang *et al* (1996) approach. The fraction of the impacting particles which adhere to the surface was approximated by the calculation of the particle viscosity as a function of particle temperature. In order to model deposit growth and heat transfer, Fan *et al* (2001) assumed that the porosity is the major factor which influences the total properties of the deposit. The porosity is calculated by the direct relation between the liquid and solid fraction of the sticking particle, once it is assumed that solid with viscosity bigger than 10^5 Pa s is liquid. Also a simple relation between porosity and particle density gives the thickness of the deposit. The thermal conductivity is described as a function of the porosity and thermal conductivity of the gas, and solid phase via empirical parameters. No further comparison with the boiler was made.

Yan *et al* (2001) based on the sticking probability, improved the sticking model introducing the mineral composition, which allowed the evaluation of the coalescence and non coalescence behavior schemes.

Tomeczek *et al* (2004) used a similar approach to Fan *et al* (2001) in which the depositing particles are based on a sticking particle probability. However, an alternative proposal for the probability was suggested, once the critical viscosity was found to vary from $10^5 – 10^8$ Pa s with some at 10^3 Pa s. This alternative proposes that the probability of a sticking particle takes into account the saturation pressure of the condensation of vapors such as Na_2SO_4, K_2SO_4 and H_2O which form a sticky layer,. For the thermal conductivity of the deposit a simple relation between gas and solid phases, via porosity, is used. Again the porosity is calculated in the same way as Fan *et al* (2001). A comparison with a boiler operation is made but further improvement in the modeling should be done, especially on the calculation of the particles trajectories and local temperatures, which were assumed known.

A different approach is presented by Bouris and Bergeles (1997) followed by Bergeles *et al* (1997) and Bouris *et al* (2001). The model proposed determines that the colliding particle adheres or rebounds

according to an energy balance at the point of impact, When the material properties of the particle and surface are taken into account it is possible to calculate the elastic and plastic deformations while the surface energy is used to determine the forces holding the particle at the surface.

According to Bouris and Bergeles (1997), the expressions of these energy terms are quite complex For a particle of a known size and velocity, they are functions of material properties of the particle and the surface on which it impacts, i.e. Young's modulus and Poisson's ratio. Further details can be found on Bouris and Bergeles (1997).

1.4 Objectives and Contribution

The main objective of this work is to develop a predictive model for the ash deposition and ash deposit growth in tube banks of coal-fired boilers. To this end, the following specific objectives are pursued:

(1) To develop a CFD model for the particle deposition on the surface of a tube of the superheating section of a pulverized coal-fired boiler.
(2) To develop a model for the ash deposit growth based on the particle-laden flow typical of coal-fired boilers. The characteristics predicted will be compared to physical and chemical measurements of a typical ash deposit collected from pulverized coal fired in boiler 6, one of the 7 boilers burning coal from Santa Catarina with 40% of ash, of 857 MW thermoelectric power plant.
(3) To develop a model for the heat transfer across the ash deposit and for the total thermal resistance around a tube of the steam superheater section.
(4) To generate information on strategies to couple the models developed into typical software used for design, analysis and optimization of coal-fired boilers.

For the solution of the flow around the tube boiler the LES turbulence model with a Lagrangian tracking of the ash particles will be used. The ash deposit growth will be modeled using a random ballistic deposition model. An effective thermal conductivity model will then be developed based on a thermal resistance network. This network is constructed based on the porous structure generated by the ash deposit growth model. The model accounts for rarefaction effects due to the low Knudsen number at the boiler conditions. Several structures are generated and compared to scanning electron images of ash deposits from the steam superheater section of a pulverized coal fired boiler from a 137 MW thermoelectric power plant. To the author's knowledge, this

is the first time that these models are applied to coal-fired boilers being the main contribution of this work. Finally, a connection between the models developed and typical coal-fired boiler analysis is suggested.

1.5 Thesis Organization

This text is structured in five chapters with four appendices.

The first chapter describes the motivation, the problem being addressed, the objectives and the contributions of the present work.

The second chapter describes the particle-laden flow field around a single circular cylinder representative of a tube in the tube bundle of the steam superheater section of a coal fired boiler. The main objective is to describe the mechanisms involved in the particle capture by a single tube and the influence of the inlet conditions on the particle deposition rate.

The third chapter describes the ash deposit growth. Three different models are proposed to represent the macro characteristics of the ash deposit. The porous structures generated by a random ballistic deposition model are compared with a typical ash deposit collected from a coal-fired boiler.

The fourth chapter proposes a heat transfer model for the heat transfer from the boiler environment and the steam. The heat transfer analysis includes a network model for the effective thermal conductivity of the ash deposit, the effect of the Knudsen flow on the thermal conductivity of the gas phase, and the impact of the ash deposit on the rise of the coal flow to reach the same thermo power output. Several porous structures are generated by the growing ash deposit model. The model has several porosities and an empirical correlation between the effective thermal conductivity and the proposed porosity of the ash deposit.

Finally, chapter five provides guidelines on using the developed models for boiler analysis, the main conclusions are listed and suggestions for future work are provided.

CHAPTER 2 - FLUID AND PARTICLE DEPOSITION ANALYSIS

2.1 Introduction.

The ash deposition inside the boiler includes many complex mechanisms. In order to get a closer look at the main mechanisms related to ash capture by the tube bundles on the superheater, some simplifications are necessary.

The flow around tubes is a classical analysis of fluid mechanics and there is a vast amount of information available in the literature.

There are closed form analytical solutions available (White (2002), Panton (2005), Happel and Brenner (1983)) for the low Reynolds number regime and for inviscid fluids. As the Reynolds number in the flow of viscous fluids increases, the low Reynolds number solution may be corrected using additional terms in the asymptotic approximation, Panton (2005). However, the typical Reynolds number based on tube diameter encountered in superheaters of interest in this work range from 500 to 2000. In this range of Reynolds number, the Boundary layer around the tube quickly undergoes a transition to turbulence and the wake of the cylinder is a fully turbulent wake. Closed form analytical solutions are no longer available for these flows. Therefore, some form of turbulence modeling is usually adopted.

The turbulence models are classified as Reynolds Averaged Navier-Stokes (RANS), Large-Eddy Simulation (LES) and Direct Numerical Simulation (DNS) models. Since particle capture depends on details of the flow close to the wall, in this work an LES model is applied in order to capture phenomena closer to the tube walls, as well the effects of the wake vortices on particle capture. A more suitable choice would be the use DNS, but this is still computationally too expensive for this problem. The general hypotheses used to develop the model are: incompressible flow, non slip velocity on the walls and uniform velocity on the inlet plane. Also, in this work, instead of calculating the flow field along the entire tube bundle a representative tube located mid-way along the superheater is chosen to return values of particle capture that will be considered valid averages for the entire tube bundle. The inlet flow conditions will be taken from Reinaldo (2004), who numerically simulated the same boiler of interest. FLUENT Version 6.3.26, 2007 software will be used.

Next, the flow regime around the tubes will be analyzed and the hypothesis assumed will be made clear.

2.2 Flow around a Circular Cylinder and Turbulence Approach

At a Reynolds number below around 49, the wake formed behind a circular cylinder on cross flow contains a symmetrical pair of equal and opposite recirculation regions, as show schematically on Fig. 2.1a. When the Reynolds number ranges from 140 to 260, the wake behind the cylinder becomes unstable and the vortices begin to shed alternately, resulting in an oscillating lift force. At a higher Reynolds number, ranging from 1,000 to 200,000, the shear layer becomes unstable resulting in an unsteady wake, as shown in Fig. 2.1b.

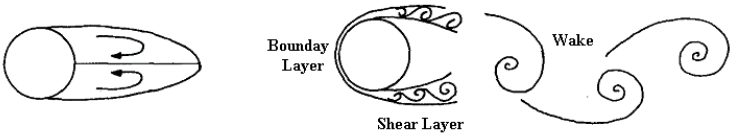

Figure 2.1 – Rendering of the development of the wake in a circular cylinder, from (a) a low Reynolds number below 49 (b) a higher Reynolds number above 1,000, as the wake becomes unsteady, forming the vortex street, adapted from Williamson, (1996)

The accurate simulation of the vortices and their interaction with the flow around the circular cylinder is a very complicated task and requires reliable models to determine, for instance, the separation point of the boundary layer around the cylinder. As noted by Pope (2000), there is very little hope of developing a single analytic theory for the solution of turbulent flows. Instead, the methodologies adopted rely on the numerical solution of sets of partial differential equations with the specification of the appropriated initial and boundary conditions. Three approaches are normally used to model turbulent flow, namely Direct Numerical Simulation (DNS), Large Eddy Simulation (LES) and the Reynolds Average Navier Stokes (RANS).

In DNS, the transient form of the Navier Stokes equations are solved to determine the velocities in a flow field for one realization of the flow. Since all length and time scales have to be resolved, DNS is computationally expensive, and applied to flows in small domains with low to moderate Reynolds numbers. In the LES approach, the Navier Stokes equations are solved for a filtered velocity field, which is

representative of the larger scale turbulent motions. So the modeling is restricted only to the small scales. The RANS approach involves the solution of the mean velocity field from a time-averaged form of the Navier Stokes equations. Since LES resolves only the large-scale eddy motion in space and time it is less intensive in computer memory and time, if compared to the DNS approach. Figure 2.2 depicts schematically the axial velocity distribution calculated from the three approaches in a fully-developed flow inside a pipe.

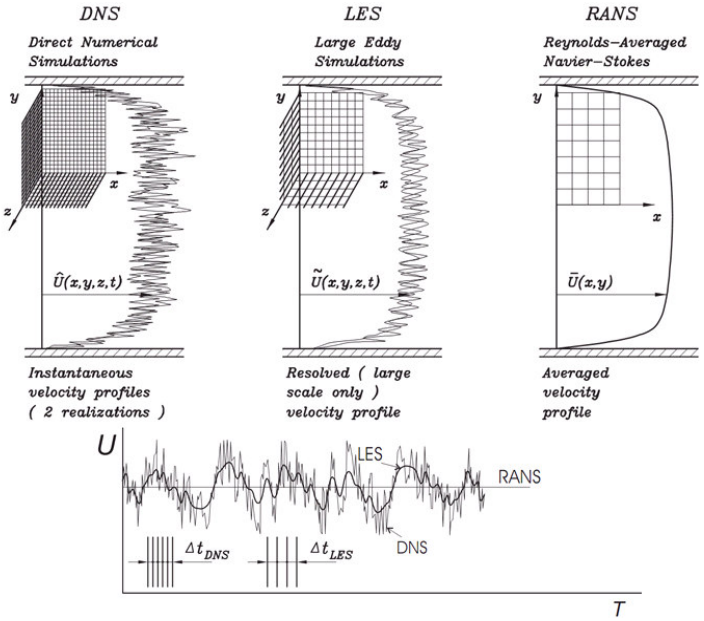

Figure 2.2 – Illustrative comparison of DNS, LES and RANS simulations of a fully developed turbulent steady state flow in a pipe. Top: typical computational grids and sketches of instantaneous velocity profile for DNS and LES, and the time average profile obtained by RANS. Bottom: time signal at a point in the flow, typical time steps for DNS and LES and the constant solution from RANS, Hanjalić (2005).

As shown in Fig. 2.2, the computational grid necessary to solve all the scales is much denser in the DNS approach than in the LES. Also, the time step is coarser in LES. In the case analyzed here, the flow behind the cylinder has a typical vortex street with large eddy shedding phenomena. Also, these large eddies interact with the particles depositing them behind the cylinder through the inertial impact

mechanism, as will be described later in this chapter. Therefore, in order to take all these effects into account, an LES approach will be used in this work.

2.3 Large Eddy Simulation (LES)

The conservation equations governing the filtered velocity field $\bar{\mathbf{U}}(\mathbf{x},t)$ are obtained by applying the filtering operation, described in Appendix A1, to the Navier Stokes Equations (NSE). For simplicity, the filtered NSE is shown only for the case with spatially uniform filters, so that filtering and differentiation commutes. For the incompressibility case with Cartesian coordinates, using the index summation, the filtered continuity and the momentum equation are, Pope (2000):

$$\frac{\partial \overline{U_i}}{\partial x_i} = \frac{\partial \bar{U}_i}{\partial x_i} \tag{2.1}$$

$$\frac{\partial \bar{U}_j}{\partial t} + \frac{\partial \left(\overline{U_i U_j}\right)}{\partial x_i} = \nu \frac{\partial^2 \bar{U}_j}{\partial x_i \partial x_j} - \frac{1}{\rho}\frac{\partial \bar{p}}{\partial x_j} \tag{2.2}$$

where $\bar{p}$ is the filtered pressure field. This equation differs from the original Navier Stokes because the product $\overline{U_i U_j} \neq \bar{U}_i \bar{U}_j$. The difference is the residual stress tensor, analogous to the Reynolds stress tensor, defined by:

$$\tau_{ij}^R = \overline{U_i U_j} - \bar{U}_i \bar{U}_j \tag{2.3}$$

Thus, substituting eq. 2.3 into 2.2:

$$\frac{\partial \bar{U}_j}{\partial t} + \frac{\partial \left(\bar{U}_i \bar{U}_j\right)}{\partial x_i} = \nu \frac{\partial^2 \bar{U}_j}{\partial x_i \partial x_j} - \frac{1}{\rho}\frac{\partial \bar{p}}{\partial x_j} - \frac{\partial \tau_{ij}^R}{\partial x_i} \tag{2.4}$$

The residual stress tensor is a second order tensor whose trace is invariant. The trace of the tensor is a scalar obtained by the contraction of the tensor. An example is:

$$\text{trace}(\mathbf{A}) = A_{jj} = A_{11} + A_{22} + A_{33} \tag{2.5}$$

According to the Smagorinsky approach, following the Boussinesq hypothesis, the residual stress tensor can be separated into an isotropic part and a deviatoric part (anisotropic):

$$\tau_{ij}^R = \frac{1}{3}\text{trace}\left(\tau_{ij}^R\right)\delta_{ij} + \tau_{ij}^r \tag{2.6}$$

The Boussinesq hypothesis states that turbulent motions create additional turbulent stresses, which can be described in the same way as

the stresses caused by molecular viscosity. The turbulent stresses involve the definition of a turbulent viscosity, which has to be computed by the turbulent model, Silva (2001).

As in the Reynolds stress tensor, the trace of the residual stress tensor is the residual kinetic energy:

$$k_r = \frac{1}{2}\text{trace}\left(\tau_{ij}^R\right) = \frac{1}{2}\left(u'_1 u'_1 + u'_2 u'_2 + u'_3 u'_3\right) \tag{2.7}$$

Substituting in eq. 2.5:

$$\tau_{ij}^R = \frac{2}{3}k_r\delta_{ij} + \tau_{ij}^r \tag{2.8}$$

Once the anisotropic component is the one effectively transporting the momentum, the isotropic residual stress is included in the modified filtered pressure

$$\overline{p} = \overline{p} + \frac{2}{3}\rho k_r \tag{2.9}$$

The true pressure only has to be computed if it is needed for some reason, such as in acoustics. In those cases, a separated model is required to estimate the subgrid kinetic energy in Eq. 2.9.

The filtered Navier Stokes equation results in:

$$\frac{\partial \overline{U}_j}{\partial t} + \frac{\partial\left(\overline{U}_i\overline{U}_j\right)}{\partial x_i} = \nu\frac{\partial^2\overline{U}_j}{\partial x_i \partial x_j} - \frac{1}{\rho}\frac{\partial\overline{p}}{\partial x_j} - \frac{\partial\tau_{ij}^r}{\partial x_i} \tag{2.10}$$

As we can see on Eq. 2.10, the problem is still unclosed due to the anisotropic component, τ_{ij}^r. Closure is achieved by modeling the anisotropic residual stress tensor.

2.4 Subgrid Models

The subgrid models attempt to simulate the influence of the filtered fluctuating scales on the large eddies, since the small scales cannot be resolved by the grid and the discretization scheme. The simplest model is the Smagorinsky model. The Dynamic approach proposed by Germano *et al* (1991) and Lilly (1992), will also be described here.

2.4.1 Smagorinsky Model

According to Lesieur *et al* (2005), the Smagorinsky model follows the mixture length assumption adapted to the subgrid scale modeling. It assumes that the eddy viscosity is proportional to a

turbulence characteristic scale (mixing length) multiplied by a turbulence characteristic velocity.

The mixing length is an analogy to the mean free path of the gas, which is the average distance that a molecule travels without colliding with another. Prandtl assumed that a fluid particle runs a distance, mixing length, before its momentum changes, Streeter and Wylie (1982). The same happens for the subgrid scale modeling results in Silva *et al* (2002):

$$\nu_t = \left(C_S l\right)^2 \sqrt{2\overline{S}_{ij}\overline{S}_{ij}} \tag{2.11}$$

where C_S is the Smagorinsky constant and l is the turbulence characteristic scale calculated as a function of the grid. In FLUENT, $(C_S l)^2$ is computed by using:

$$\left(C_S l\right)^2 = \min\left(\kappa d, C_S V^{1/3}\right) \tag{2.12}$$

where κ is the von Kármán constant, d is the distance to the closest wall and V is the volume of the computational cell. As we can see in Eq. 2.12, there is a damping function as the flow goes to the walls. The behavior of the LES close to the wall will be handled in a further section.

Also, Smagorinsky assumed the local equilibrium in the small scales, which means that the production of the turbulent subgrid stress is equal to the dissipation. The local equilibrium consists in assuming that the small scales of turbulence are always in equilibrium because they recover instantaneously from the non equilibrium prompted by any external force, Silva (2001). Attention has to be paid because the equilibrium assumption implies that the filter width must be in the inertial range. These assumptions, together with the Boussinesq hypothesis, lead the anisotropic residual stress tensor to:

$$\tau_{ij}^r = -2\nu_t \overline{S}_{ij} \tag{2.12}$$

Inserting Eq. 2.12 into 2.10, leads to:

$$\frac{\partial \overline{U}_j}{\partial t} + \frac{\partial\left(\overline{U}_i \overline{U}_j\right)}{\partial x_i} = \left(\nu + \nu_t\right)\frac{\partial^2 \overline{U}_j}{\partial x_i \partial x_j} - \frac{1}{\rho}\frac{\partial \overline{p}}{\partial x_j} \tag{2.13}$$

2.4.2 Dynamic Model

One of the drawbacks of the Smagorinsky model is the imposition of an *ad hoc* constant, $C_S > 0$, in the entire domain. It means that energy transfer is always from the large to the small scales, there is no backscatter.

Usually average, the energy is transferred from the large scales to the small ones ("forward scatter"), but reverse energy flow ("backscatter") from the small scales to the large ones may also occur locally. It is more pronounced near the walls in the transition region. Also, different regimes of flow lead to different Smagorinsky constant, from laminar, with $C_S = 0$, to highly turbulent with $C_S = 0.23$. In the flow around bluff bodies the transition from the laminar regimes, near the walls, to the turbulent ones is expected, so a unique *ad hoc* constant can seriously compromises the flow field prediction.

Germano *et al* (1991) and Lilly (1992) conceived a procedure in which the Smagorinsky model constant is dynamically computed based on the information provided by the resolved scales of motion. The dynamic procedure obviates the need to specify the model constant in advance. Besides, the dynamic approach allows the backscatter information. The derivation of the model is described in the Appendix A2. In FLUENT the dynamic model is clipped at 0 and 0.23 to avoid numerical instabilities, FLUENT (2007).

2.5 Near Wall Resolution

According to Pope (2000), there are two distinct ways to treat near wall regions: (1) To model all scales down to the wall (LES with near wall resolution – LES-NWR), and (2) The near wall region is modeled, because the filter width and the grid resolution are too coarse to resolve the large scales near the wall (LES with near wall modeling – LES-NWM), as illustrated in Fig. 2.3

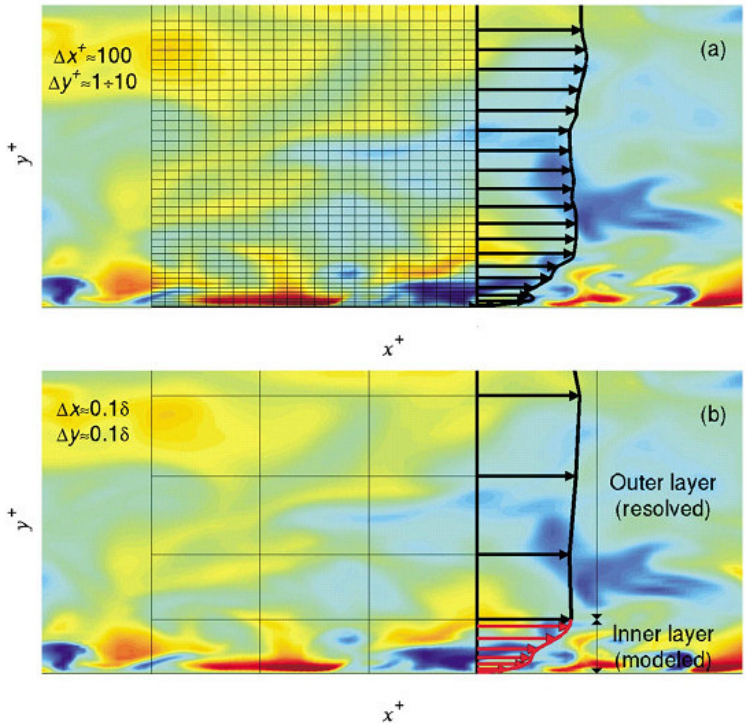

Figure 2.3 – Sketch illustrating the wall layer modeling philosophy (a) Inner layer resolved. (b) Inner layer modeled, Piomelli and Balaras (2002).

Piomelli and Balaras (2002) analyzed both approaches to the wall resolution and compared several models in the LES-NWM approach. Figure 2.3 shows the simulation of a plane channel flow with both approaches and the grid used. From one time step to the next, the grid cell adjacent to the wall sees a large number of near wall eddies. They go through several life cycles, because their timescale is smaller than the time step, usually determined by outer flow conditions. If the sample of near wall eddies in a grid cell is large enough, the inner layer can be assumed to be governed by the Reynolds Average Navier Stokes (RANS) equations, rather than the filtered Navier Stokes equations solved in LES in the outer layer. For this assumption to hold, the grid size must be very large, if the grid is too fine, the statistical considerations on which wall layer models are based fail.

It is clear, from Fig. 2.3, that the computational cost to solve all the scales down to the wall in a high Reynolds number is high so, the

only feasible situation to use LES in the attached flow is to use the near wall models to solve the inner layer and LES on the outer layer.

In the Smagorinsky model, the specification of $C_S\Delta$ is justifiable for Δ in the inertial subrange of high Reynolds numbers. This is clearly not the case of the flow on the viscous wall region and this specification leads to a non-zero residual viscosity and shear stress at the wall. Instead, a van Driest damping function to specify $C_S\Delta$ is a common choice:

$$\nu_t = \left(C_S l \left[1 - \exp\left({-y^+}/{A^+} \right) \right] \right)^2 \sqrt{2\bar{S}_{ij}\bar{S}_{ij}} \tag{2.14}$$

where y^+ is the normalized distance from the wall and A^+ is the van Driest constant, usually $A^+ = 25$ for the flow around circular cylinder, Breuer (1998).

In FLUENT, there are two possibilities in the near wall model, when the mesh is fine enough to resolve the laminar sublayer, the wall shear stress is obtained from the laminar stress strain relationship:

$$\frac{\bar{U}}{U_\tau} = \frac{\rho U_\tau y}{\mu} \tag{2.15}$$

where U_τ is the friction velocity, y is the normal distance to the wall and μ is the viscosity. If the mesh is too coarse to resolve the laminar sublayer, it is assumed that the centroid of the wall adjacent cell falls within the logarithmic region of the boundary layer, and the log law is employed:

$$\frac{\bar{U}}{U_\tau} = \frac{1}{\kappa_{vK}} \ln E\left(\frac{\rho U_\tau y}{\mu} \right) \tag{2.16}$$

where κ_{vK} is the von Kármán constant and E = 9.793, in the buffer layer, the two walls are blended. Also, an alternative to the near wall approach is based on the work of Werner and Wengle (1991), *apud* FLUENT (2007). They proposed an analytical integration of a power law near the wall velocity distribution to compute the wall shear stress. This approach, according to Piomelli and Balaras (2002), is based on the logarithmic law of the wall and on the local equilibrium of the near wall region. Its validity strongly depends on the size of the averaging volume (grid cell), which must contain a significant sample of inner layer eddies. In FLUENT manuals, in the recommendation for obtaining best results it might be necessary to indicate the use of a very fine near wall mesh spacing on the order of $y^+ = 1$. Fröhlich *et al* (1998) used the Werner and Wengle wall function and argued that, with a mesh fine

enough, this condition is actually applied in the viscous sublayer. Since in this region a linear velocity distribution is assumed, the wall function becomes effectively a non slip condition, and its results presented $y^+ \sim 1$.

2.6 Particle Modeling

The flow on the pulverized coal boiler involves more than one phase and it is known as a multiphase system. Only two phases are distinguishable here: (1) The disperse phase or the particle phase or ash particle and (2) The continuous phase or carrier phase or fluid phase. Also, the multiphase flow can be classified as (i) A dilute flow, where the particle motion is controlled by the surface and body forces on the particle, or (ii) A dense flow, where the particle motion is controlled primarily by particle – particle collisions or interactions. The motion of particles in dense phase transport or in fluidized beds is strongly dependent on particle collisions, Crowe *et al* (1996).

Most of the dispersion models can be broadly classified based on the type of reference frame used for the formulation of the transport equations. There are two types of reference frames: Lagrangian and Eulerian. In the Lagrangian reference frame, individual particles are tracked as they move through the computational domain. In the Lagrangian particle models, the reference frame moves with the particles, and the instantaneous position of a particle can be considered as a function of the location from where the particle was originated from and the time elapsed.

In the Eulerian models, the reference frame is stationary and the particles pass through fixed differential control volumes. In this approach, the characteristics of the particulate phase are obtained by solving partial differential equations in a given coordinate system. Eulerian models are popular when the particle loading is high, as in fluidized bed combustion systems. In this work, the focus will be on the Lagrangian approach, which is the natural way to treat particles in dilute flows, Shirolkar *et al* (1996).

2.6.1 Discrete Phase Model

In the Lagrangian frame of reference, the second phase consists of spherical particles dispersed in the continuous phase. These particles are treated as discrete objects and their motions are tracked as they move through the flow field. In this case, it is possible to account for the non-continuum behavior of particles and particle history effects. It should also be noted that, although it is theoretically possible to track each

individual particle, each particle is a representative sample with the same dimension and initial condition. This approach reduces significantly the computational efforts. However, the number of trajectories should be high enough to provide statistics that characterize the particle behavior, Shirolkar *et al* (1996).

The trajectory of the discrete phase particle is obtained by integrating the force balance on the particle, which is written in a Lagrangian reference frame. This force balance equates the particle inertia with forces acting on the particle. These forces can be classified as (1) Forces that act on a particle due to its motion of particle; (2) Forces that act on the particle due to the motion of the surrounding fluid; (3) Forces that act on the particle irrespective of the fact that the particle is in motion or is immersed in a flowing fluid (body forces, such as gravity); (4) Forces that act on any object immersed in fluid (buoyancy forces). The equation of motion has been identified as the BBO (Basset-Boussinesq-Oseen) equation, which can be written (for the x direction in Cartesian coordinates), FLUENT (2007):

$$\frac{dU_p}{dt} = F_D\left(U - U_p\right) + \frac{g_x\left(\rho_p - \rho\right)}{\rho_p} + F_X \tag{2.17}$$

where U_p is the particle velocity and U is the instantaneous velocity of the continuous phase. Also, the first term on the right hand side is the drag force, F_D, the second term are the forces due to the gravity and buoyancy. The last one, F_X, is an additional force that can be considered in the analysis, such as the Basset, virtual mass, Magnus force and thermophoretic.

In most fluid particle systems, the drag force is the most important force acting on the particle. Several different functions have been used to determine the drag term for different configurations. These functions depend on the particle Reynolds number, Re_P, Eq. (2.18) and reflect the variation of the drag coefficient with the relative velocity.

$$Re_P = \frac{\rho d_P \left|U_P - U\right|}{\mu} \tag{2.18}$$

where d_p is the particle diameter and the drag force can be written as, FLUENT (2007):

$$F_D = \frac{18\mu}{\rho_P d_P^2}\frac{C_D\, Re_P}{24} \tag{2.19}$$

where C_D is the drag coefficient, which is a function over several ranges of Re_P, as described by FLUENT (2007).

Additional forces can be accounted for by the last term on the right side of Eq. 2.17, which are the Basset force that results from the transitory nature of particle's boundary layer and is mainly influenced by the history of the particle trajectory. The virtual mass force is due to the difference in the acceleration/deceleration in a fluid, causing the acceleration/deceleration of a certain fraction of the surrounding fluid, and the Magnus force results from the rotating particle immersed in a non-rotating fluid. All these forces can be neglected in the present dilute flow mostly because $\rho/\rho_P \sim 10^{-3}$, also assuming non-rotating particles, Shirolkar *et al* (1996). All of these assumptions were considered by Bouris *et al* (2001), so that only the thermophoretic force will be considered because of the nature of the flow. Another simplification is the collision effects, agglomeration and coalescence were not considered. The particle turbulence interactional was also not taking into account leading to a one way coupling only.

Thermophoretic force is the resulting force due to the temperature gradient in the surrounding medium. The molecules moving from the hot surface carry greater kinetic energy than those moving from the cold side, resulting in a net force on the particle, as illustrated in Fig. 2.4.

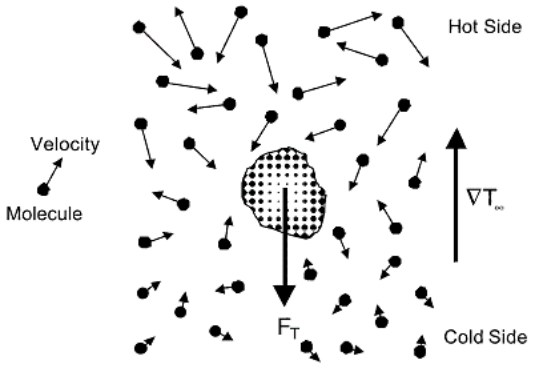

Figure 2.4 – A particle immersed in a gas with temperature gradient, Zheng (2002).

Although thermophoresis is important only for micron and submicron particles, while the primary mechanism for large particle impaction is the inertial impact, it was included in the equation of particle motion. In the range analyzed here, there are small particles that may move due to the temperature gradient between the tube wall and the flow field. In FLUENT the thermophoretic acceleration is described as:

$$F_X = -K_{th}\frac{1}{m_p T}\frac{\partial T}{\partial x} \tag{2.20}$$

where K_{th} is the thermophoretic coefficient defined by Talbot *et al* (1980).

Another important parameter in fluid particle flows is the Stokes number, which is the ratio of particle response time or particle relaxation time, τ_P, vs. a time characteristic of the fluid motion, τ_F.

$$St = \frac{\tau_P}{\tau_F} \tag{2.21}$$

A small Stokes number $(St \ll 1)$ implies that the particles can maintain near velocity equilibrium with the carrier phase and its motion is governed by the turbulence of the fluid. Meanwhile, a high Stokes number $(St \gg 1)$ suggests that the particle motion is unaffected by the turbulence of the carrier phase, Crowe *et al* (1996).

The particle relaxation time is defined as the rate of response of particle acceleration to the relative velocity between the particle and the carrier fluid. In other words, a dense particle will have less fluctuating velocity as compared to that of the fluid, thus reducing the particle root mean square (rms) of the fluctuating velocity:

$$\tau_P = \frac{24\rho_P d_P^2}{18\mu_F C_D Re_P} \tag{2.22}$$

In addition, numerical models for fluid particle flows are based either on one way or two way coupling. In a model based on one way coupling, it is assumed that the presence of the particulate phase has a negligible effect on the properties of the carrier phase. The one way coupling assumption is typically valid for small particle to fluid mass concentration ratios and/or high Stokes numbers. The two-way coupling approach includes the effects of the particle on the carrier phase. Additionally, inter-particle interactions may become important in a dense regime. Hence, this regime is characterized by the so called four way coupling, Crowe *et al* (1996). The discrete phase formulation used by FLUENT contains the assumption that the second phase is sufficiently dilute so that particle-particle interactions are negligible.

Some notes must be added concerning the instantaneous fluid velocity, U, in the Eqs. 2.17 and 2.18. In RANS analysis, the Eulerian fluid velocity can be acquired from the time average Navier Stokes equations. It is, therefore, necessary to estimate the fluctuating component of the fluid velocity at every particle location, as the particle

moves in discrete time steps through the computational domain. Usually, it is assumed that the fluctuating component is a Gaussian function of the turbulent kinetic energy.

As the turbulence approach considered here is LES, some consideration should be made in order to take into account the effects subgrid scales on particle deposition. In FLUENT these fluctuations are considered through the use of a Discrete Random Walk model (or eddy life time model). This model assumes that the fluctuating velocities follow a Gaussian distribution and all the velocity fluctuations are equivalent in all the directions, which is probably true in the outer region, but probably not near the walls. Also it is assumed that the contributions of the subgrid scales on particle dispersion are negligible. It is expected that this assumption may affect mostly the smaller particles, which are more responsive to subgrid scale motions occurring in smaller time scales. The same assumption was made by Bouris *et al* (2001).

An analysis of the SGS impact on the particle deposition can be summarized in the work of Wang and Squires (1996). They compared a LES approach on the particle deposition, in a vertical turbulent channel flow, to DNS and data of McLaughlin (1989). They argued that SGS models, which reflect local properties of turbulence are especially attractive for the computation of particle laden flows. They reached this assumption since predictions of particle transport and deposition should be expected to be significantly improved by more accurate parameterizations of the turbulence. They analyzed the correlation coefficient between the wall normal components of the fluid and particle velocities for the depositing particles and showed that it is much smaller than unity near the wall, especially for particles with large relaxation time. This result demonstrates that particles are brought to the near wall region by turbulent motions but travel to the wall by free flight.

It is known that particles with smaller relaxation times are responsive to a broader spectrum of turbulence scales, and errors in the representation of the smallest resolved scales and that SGS motions will adversely affect predictions of particle motion. Wang and Squires (1996) showed that there is no difference for particle relaxation time, expressed in wall units of 4, when considering the effect of SGS in the particle deposition. While for a particle relaxation time of 2, the subgrid scale fluctuation increases the wall normal velocities for depositing particles by 30% near $y^+ = 5$, but the deposition rate increases by only about 10%. Considering the analysis by Wang and Squires (1996), it is

expected that the contribution of the SGS on particle deposition be negligible and it will not be considered here.

2.7 Numerical Method

2.7.1 Spatial Discretization

Here, the commercial CFD code FLUENT was used to simulate the flow field around the circular cylinder and the particle flow. The whole numerical setup followed the FLUENT recommendations for the LES case.

FLUENT uses 3D finite volume method co-located scheme, where both pressure and velocity are stored at cell centers. For a non-staggered arrangement, the values at the cell faces are not available and must be interpolated. For pressure, and under the LES approach, the use of the PRESTO interpolation scheme is recommended, especially for strongly curved boundaries. The PRESTO (PREssure STaggering Option) scheme uses the discrete continuity balance for a "staggered" control volume across the face to compute the "staggered" pressure. The face values of velocities, which are necessary to compute the continuity equation, are calculated using a similar procedure to that of Rhie and Chow (1983), *apud* FLUENT, (2007), in which the face velocity is not averaged linearly. Instead, a momentum weighted averaging is performed, using weighting factors based on the momentum coefficients. This is necessary to determine the mass fluxes at the cell faces.

According to FLUENT, 2007, the best choice for the convection terms of the filtered Navier Stokes equations is the bounded central differencing scheme. This scheme is based on the normalized variable diagram (NVD) approach from Leonard (1991) with the convection boundedness criterion (CBC). A brief description of these approaches is given Appendix A3.

The gradient is computed by the Green Gauss theorem, which performs a summation over all faces enclosing the cell. The face value of the gradient is taken from the arithmetic values at the neighboring cell centers.

An analysis of the different schemes for the convective fluxes in the LES approach to the flow around a circular cylinder is shown in the work of Breuer (1998). The numerical dissipation produced by the scheme for the convective fluxes is of much greater relevance for LES than its formal order of accuracy in space itself. Breuer (1998) investigated different approximations for the convective fluxes in the

filtered Navier Stokes equations and showed that the hybrid scheme, which switches between the upwind and central differencing scheme, postponed the separation angle resulting in a shorter recirculation zone. The same trends were demonstrated when using the HLPA (hybrid linear/parabolic approximation), which combines a second order upstream weighted approximation with first order upwind differencing.

Breuer (1998) also used the QUICK scheme and showed a recirculation length 27% larger than the experimental value and a back pressure even smaller than in experiments. QUICK combined with the midpoint rule is of second order accuracy. It generates a dissipative fourth order error term that acts as an additional subgrid scale model, similarly to the hybrid and HLPA schemes, but it should shorten the recirculation length. No explanation was found for this unexpected behavior, Breuer (1998).

The best results found by Breuer (1998) are for the central differencing scheme (CDS-2), which linearly interpolates the value at the cell face, and for the central differencing scheme (CDS-4) with third order polynomial through four nodes.

2.7.2 Temporal Discretization

Time advancement in FLUENT is of a second order segregated. The segregated solution process, by which the equations are solved one by one, introduces a splitting error. This error is reduced to the truncation error via non-iterative time advanced scheme (NITA), which performs a single outer iteration per time step to solve the individual set of equations, Fig 2.5.

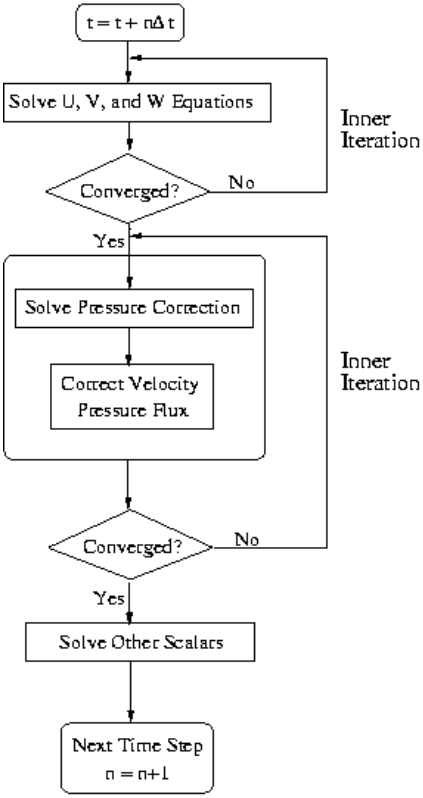

Figure 2.5 – Overview of the Non-Iterative Time Advancement Solution Method (NITA), FLUENT, 2007.

NITA is used with the fractional step method (FSM), with second order truncation error. FSM integrates the Navier Stokes equations in time at each time step by first solving the momentum equations, using an approximate pressure field to yield an intermediate velocity field that will not, in general, satisfy continuity. A Poisson equation is then solved with the divergence of the intermediate velocity as a source term to provide a pressure or pressure correction. This term is then used to correct the intermediate velocity field, providing a divergence free velocity. The pressure is updated and integration proceeds to the next time step, Armfield and Street (2004).

2.8 Test Case – $Re_D = 3900$

Prior to the analysis of the boiler superheater, it is necessary to set up the numerical case to allow an accurate description of the physics involved in the flow field around the tubes of the boiler. Since the proposal is to use the LES approach to take into account the turbulence effects on the flow field, a detailed set up of the grid is necessary because LES is very sensitive to the wall effects, which can change the flow field around the circular cylinder.

In order to set up the mesh for this case, the back pressure coefficient is used in comparison with other simulation and experimental cases since it takes into account the pressure gradient along the wall, which indicates the mesh quality.

The first assumption here is to analyze only one tube that is representative of the tube bundle. This hypothesis is done in order to simplify the analysis while still capturing the main mechanisms involved in the particle deposition.

Another simplification is to set up the test case to isothermal at a high Reynolds number. The same set up will suit the flow field with heat transfer and particle trajectories in a low Reynolds number, as the case analyzed here. This is expected because the grid will be suited for a high flow case and all the turbulence generated from the quenching effect due to the low temperature of the wall tube. Although in the boiler case the Reynolds number is low when compared to the free stream, it will be solved and consequently the particle deposition will be promptly analyzed.

The Reynolds number considered in the test case is $Re_D = 3900$ (based on cylinder diameter and free stream velocity). For this subcritical number, there are several papers on numerical analysis with LES/DNS and experimental studies. For example, the works of Breuer (1998), who investigated the numerical and modeling aspects involved in the flow past a circular cylinder with LES; Fröhlich *et al* (1998), who compared the finite volume and finite element solutions on structured and unstructured grids; Lübcke *et al* (2001), who compared the RANS approach with LES in bluff body flows, and Franke and Frank (2002), who analyzed the influence of time averaging in a finite volume compressible code. Also, Ma *et al* (2000) investigated the dynamics of the near wake in turbulent flow via direct systematic spectral and large eddy simulations. Kravechenko and Moin (2000) also studied the same flow with a high order accurate numerical method based on B-splines. All these studies are based on the experiments of Ong and Wallace (1996) and Lourenco and Shih (1993) *apud* Ma *et al* (2000). Also, Liang

and Papadakis (2007) studied a pulsating cross flow over a singular cylinder in a subcritical Reynolds number. The experimental data of Lourenco and Shih (1993) and some of the Ong and Wallace (1996) are shown along the text. They were taken from the articles described above.

The computational domain is described in a fixed Cartesian coordinate system (x, y, z). Y-axis is along the streamwise mean flow direction, Z-axis is along the spanwise direction and X-axis is perpendicular to both Y- and Z-axis. The origin of the coordinate system and the size of the computational domain are shown in Fig. 2.6. The size of the domain is the same used in the Franke and Frank (2002) simulations.

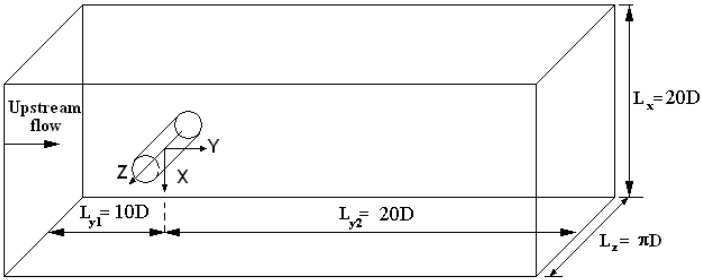

Figure 2.6 – Computational domain and physical configuration of the circular cylinder.

The diameter of the cylinder is the same as for the boiler superheater, 31.8 mm, with a blockage ratio of 5%. The velocity at the inlet plane was set to 23.05 m/s in order to have Re_D close to 3900 at 25ºC. The spanwise direction is usually estimated from the experimental measurements or prior knowledge of the sizes of the streamwise vortex structures. Many authors, such as Frölich *et al* (1998), Breuer (1998), Lübcke *et al* (2001) and Liang and Papadakis, (2007), have reported that the spanwise direction should be at least πD to represent the three dimensional structures. The grid, Fig. 2.7, is stretched in the normal direction to the cylinder wall with a stretching factor of 1.03 in order to avoid abrupt changes. This stretching factor is the same used by Breuer (1998) and Frank and Franke (2002), but lower than the 1.11 used by Liang and Papadakis (2007). The number of grid points on the circumference of the cylinder is 128, the same number that Liang and Papadakis (2007) used, and which is lower than Fröhlich (1998), Breuer (1998) and Franke and Frank (2002) all whom used 165 or 193. Breuer

(1998) compared the 165 and 209 elements on the circumferential direction and found irrelevant results.

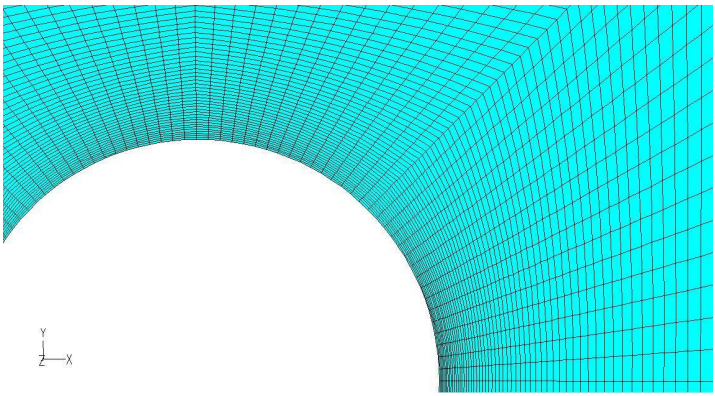

Figure 2.7 – Computational domain and physical configuration of the circular cylinder.

In the spanwise direction, 32 grid points were used. Breuer (1998) compared results on the same spanwise domain, πD, with different numbers of elements, 32 and 64. The same trends were obtained on both. Spanwise grid refinement leads to some increase on deviations with the Smagorinsky SGS, but improved results were obtained with the dynamic model. The same spanwise number of grid elements was also used by Fröhlich (1998) and Frank and Franke (2002). But lower if compared to the Kravchenco and Moin (2000), who used 48 elements. The height of the first cell at the cylinder surface, $1l/\lambda$, is shown in Tab. 2.1 as well as the total amount of hexahedral control volumes for each case analyzed here.

At the inflow plane, constant velocity is imposed. No slip boundary condition at walls is used on solid walls. In spanwise and cross wise directions, periodic boundary condition is assumed. At the outflow boundary, a zero diffusion flux is imposed. This condition is consistent with the fully developed flow assumption. According to Breuer (1998), this condition ensures that the vortices can approach and pass the outflow boundary without significant disturbance or reflections into the inner domain. This is different from the pressure outflow that is known to be reflective when an inhomogeneous pressure distribution, like the one in the large von Kármán vortices, is convected across the outflow, Franke and Frank (2002). The same outflow condition considered here is used by Fröhlich (1998) and Ma *et al* (2000).

The mean integral results for all cases analyzed here are described in Tab. 2.1, some results from previous authors considered here are also shown. The flow was initialized with a LES simulation with a very high time step. After that, the simulation was run for six shedding cycles before time averaging begun. The solution variables were then sampled at every time step, corresponding to a dimensionless time interval of $\Delta t^* = \Delta t U_0 / D \approx 2.64 \times 10^{-3}$, which is the same time step used by Kravchenko and Moin (2000) and Franke and Frank (2002). The flow statistics were accumulated over approximately six vortex shedding cycles $\left(T^* = T U_0 / D \approx 26\right)$, close to the ones in Kravchenko and Moin (2000), who used seven shedding cycles. Also, statistics were averaged over the periodic spanwise direction.

Franke and Frank (2002) compared the results of different time averaging and showed that even $T^* = 200$ was not enough to reach a statistically converged mean flow field. With the increase of the time averaging interval, Franke and Frank (2002) obtained a substantially longer recirculation region, accompanied by an increase in the base pressure. The same results were obtained by Ma *et al* (2000). This deviation from the experimental results may be attributed to the dissipative numerical scheme.

Table 2.1 shows the different heights of the first cell at the cylinder surface, $l1/\lambda$. It also shows the recirculation length, L_r, here defined as the zero average velocity in the centerline streamwise.

Height of the first cell at the cylinder surface, l1, used by Franke and Frank (2002) is $3.5 \times 10^{-3} D$ which is, according to them, approximately 30% larger than the value used by Breuer (1998) and Fröhlich *et al* (1998). Also, Liang and Papadakis (2007) used $1.75 \times 10^{-3} D$ for the finest grid, which is slightly higher than the finest mesh of Beaudan and Moin (1994) ($1.25 \times 10^{-3} D$), *apud* Liang and Papadakis (2007).

The height of the first cell on the surface will influence the calculus of the flow around the cylinder and consequently the separation of the boundary layer. As the separation of the boundary layer is the only source of turbulence in this type of flow, the height of the first cell will influence the flow field behind the cylinder. In order to isolate the effects of the l1 size, the dynamic subgrid model is chosen because it calculates accurately the amount of energy dissipation on each cell of the grid, thus avoiding possible source of errors from the tuning of an *ad hoc* constant, as in the Smagorinsky SGS.

Table 2.1 – Overview of all simulations of the cross flow around a circular cylinder.

Run	ll/λ	Nº Cell	SGS Model	T^*	L_r/D	y^+ (max.)	$-\langle C_{Pb} \rangle$
Exp	-	-	-	-	1.18± 0.05	-	0.90± 0.05
LD1	1	894 336	Dynamic	26	0.92	5.80	1.24
LD2	1/4	1 079 168	Dynamic	26	1.32	1.50	0.99
LD3	1/8	1 165 568	Dynamic	26	1.59	0.74	0.91
LS1	1/4	894 336	$C_S = 0.032$	26	1.50	1.50	0.94
LS2	1/4	1 079 168	$C_S = 0.1$	26	1.59	1.60	0.92
KMC5[I]	-	1 333 472	Dynamic	35	1.35	-	0.93
MC2[II]	-	-	DNS-	624	1.59	-	0.84
FF[III]	1/5	1 138 688	$C_S = 0.1$	50	1.34	-	0.94
FF	1/5	1 138 688	$C_S = 0.1$	200	1.64	-	0.85
L[IV]	-	900 000	Dynamic	-	1.00	-	-
BC2[V]	1/5	871 200	$C_S = 0.1$	-	1.12	-	1.05
BC3	1/5	871 200	Dynamic	-	1.20	-	1.01
FLR2[VI]	1/5	881 792	$C_S = 0.1$	-	1.09	-	1.06

[I] KMC5 – Kravchenko and Moin (2000) Case 5
[II] MC2 – Ma *et al* (2000) Case 2
[III] FF – Franke and Frank (2002)
[IV] L – Lübcke *et al* (2001)
[V] BC – Breuer (1998) Case 2 and Case 3
[VI] FLR2 – Fröhlich *et al* (1998) Case LRUN2

The coarse grid used has the height of the first cell, with the same size of the Taylor microscale, λ. The Taylor scale is located between the Kolmogorov microscale and the integral scale, and can be estimated by, Arpaci (1997):

$$\frac{\lambda}{D} = \frac{1}{\sqrt{Re_D}} \tag{2.23}$$

According to Pope (2000), the Taylor scale does not have a clear physical interpretation. Here, λ is used as a reference for the first cell height analysis.

According to Tab. 2.1, in spite of the low time averaging interval used in this work, $T^* = 26$, none of the runs analyzed here presented good results, when compared to the experimental results. The run LD1 got a very close result of the recirculation length but very different from the back pressure coefficient. As described before, the Werner and Wengle function is based on the equilibrium approach and its validity is very dependent on the size of the averaging volume, which must contain a significant sample of inner layer eddies. The volume of the first cell resulted in $y^+ = 5$ for the run LD1, although it can be considered in the viscous sublayer, it is possibly far from the equilibrium approach. The bad description of the flow near the wall compromised the flow field in the wake of the cylinder, resulting in a shorter recirculation length.

As stated by Kravchenko and Moin, (2000) the shorter recirculation length obtained by Lourenco and Shih (1993) is possibly due to the earlier transition to the turbulence, and consequent smaller recirculation zone, since the coarse grid, used by Kravchenko and Moin (2000) and Ma *et al* (2000) produced results in very good agreement with the experimental results. Kravchenko and Moin (2000) used an accurate numerical method based on B-splines and Ma *et al* (2000) used a direct numerical simulation and large eddy simulations based on the spectral/hp method. In spite of the bad description of the flow field around the circular cylinder, the flow field of the LD1 run in the near wake was in agreement with the experimental results of Lourenco and Shih (1993), Fig. 2.9.

In the BC2 and BC3 runs, Breuer (1998) used 32 elements in the resolution of the spanwise direction along with a central differencing scheme, which probably lead to a small resolution of the vortices in that direction. FLR2 run, as in Breuer (1998), used only 32 elements in the spanwise direction. On the run L, Lübcke *et al* (2001) used only 14D in the crosswise direction which probably lead to a shorter recirculation zone.

The influence of the time averaging interval on the converged results is shown by the FF runs with 50 and 200 dimensionless time. Surprisingly the FF run with the time averaging interval of 50 produced almost the same result as LS2.

Comparing LS2 and LS1, the higher fluctuations imposed by the Smagorinsky constant lead to a higher recirculation zone due to the high energy content in the cell volume. Similar results were obtained by Ma *et al* (2000).

The MC2 run had a higher refinement in the spanwise direction for the same spanwise domain, πD. As Ma *et al* (2000) stated, this higher resolution increased the width of the profile at y/D = 1.06, accentuating the U shape profile and increasing the recirculation length. The spectral DNS employed by Ma *et al* (2000) converged to a U shape profile for πD spanwise domain and to a V shape profile for a $2\pi D$ spanwise domain with the same spanwise resolution.

Figures 2.8 and 2.9 show the streamwise profile of the streamwise velocity at the center line and the spanwise profile of the streamwise velocity at y/D = 1.06.

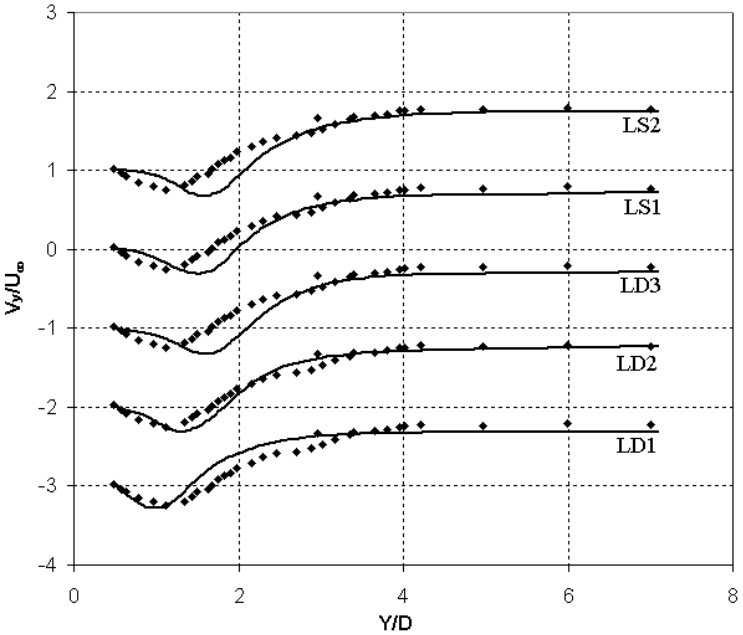

Figure 2.8 – Streamwise velocity on the centre line in the wake of a circular cylinder at Re_D = 3900, captions described in Tab. 2.1. Full diamonds, represent the experiments of Ong and (1996) Wallace and Lourenco and Shih (1993)

As stated before, the coarse grid leads to a separating laminar shear layer shorter than that presented in a fine grid resolution. This means that the transition to turbulence in the separating shear layer occurs closer to the cylinder, Fig. 2.10, and leads to the development of the V shape spanwise profile in the streamwise velocity at y/D = 1.06, Fig. 2.9.

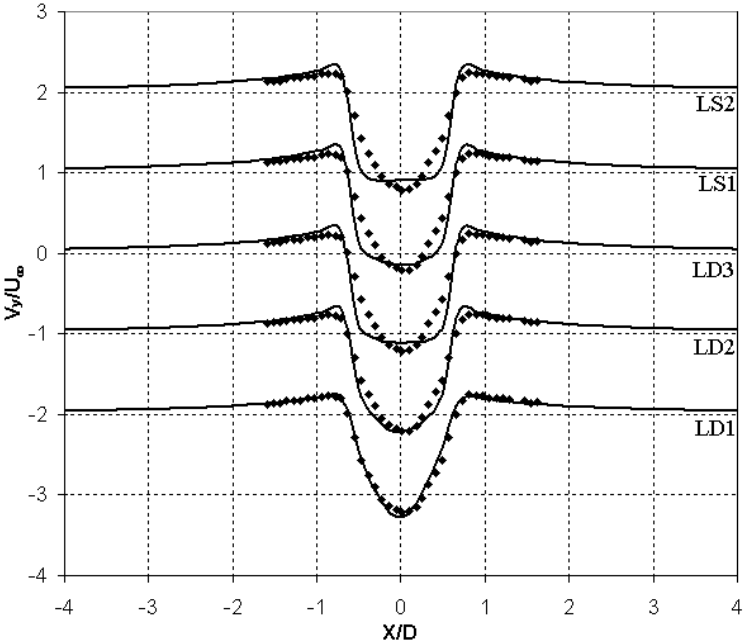

Figure 2.9 – Streamwise velocity at Y/D = 1.06 in the wake of a circular cylinder at Re_D = 3900. For details, see the caption of Fig. 2.8.

Here, again, the results for the coarser resolution agree very well with the experimental results of Lourenco and Shih (1993) and present a V shape profile for the streamwise velocity, differently from that U shape presented in the finer resolution. These results are evidence that some external disturbances influenced the experiment of Lourenco and Shih (1993). In the case of Smagorinsky SGS the stronger subfilter model dissipation, LS2, presented a flatter a U shaped profile than that from the run LS1, which is very similar to the run LD3. The influence of the radial resolution on the transitional shear layers is shown in Fig. 2.10.

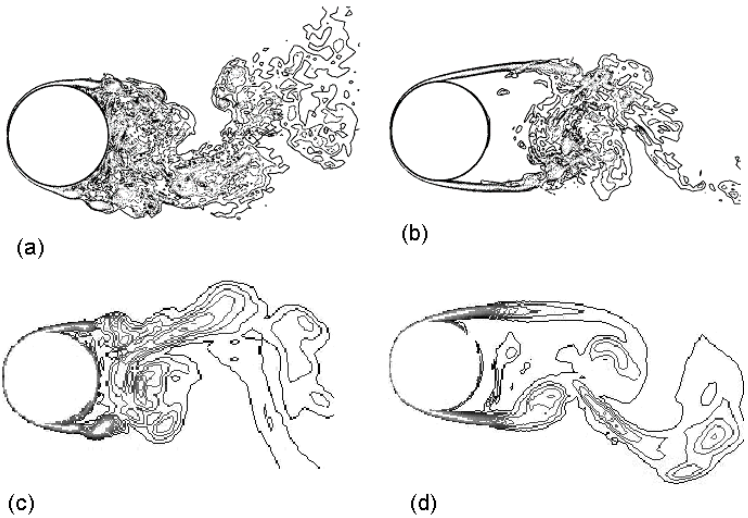

Figure 2.10 – Instantaneous magnitude of vorticity $\omega D/U_\infty$ in the near wake at $Re_D = 3900$: 10 contours from 3 to 20. (a) Coarse spanwise resolution from Kravchenko and Moin (2000). (b) Fine spanwise resolution from Kravchenko and Moin (2000), (c) LD1 run, (d) LD3 run.

As shown in Fig. 2.10, the laminar shear layers are substantially shorter in the coarse simulation from Kravchenko and Moin (2000) and the LD1 run than in the fine grid calculation, which leads to turbulence transition closer to the cylinder resulting in a V shape profile and shorter recirculation length. This means that an inadequate resolution in the radial direction leads to a shorter shear layer and consequently a shorter recirculation length and V shape profile.

It is also clear from Fig. 2.10 that although the run LD3 has similar behavior to the fine spanwise simulation of Kravchenko and Moin (2000), is not as turbulent as it should be. It seems there is some damping from the grid resolution which is probably due to the 32 elements in the spanwise direction used here. This resolution is the same used on the BC2, BC3, FLR2 and FF runs. The behavior of LD3, similar to the Kravchenko and Moin (2000) case, is probably due to the low time averaging of the LD3 run which indicates that the simulation is still not converged.

Although the LD2 run is not converged for the case of Re_D = 3900, it will be used for the boiler case because the Re_D of 1000 is smaller and the grid resolution considered here is enough to solve the

flow field. Also, the cell numbers are in an intermediate case between the LD3 and LD1 saving some computing RAM.

2.9 Boiler Case – $Re_D = 1000$

In order to simulate the boiler conditions, some inlet data were taken from Reinaldo (2004). The whole pulverized coal boiler was simulated by Reinaldo (2004) and the inlet data, for the case analyzed here, were taken from a plane perpendicular to the main flow direction in the region of the superheater. The inlet velocity was considered as being that in the middle of the plane, 4 m/s. Flue gases were at 1300 K without perturbations and the cylinder wall temperature was at 750 K, all other conditions were kept the same, i.e. periodic boundary conditions. Statistical averages were taken with T* = 37 with a prescribed tolerance for the normalized residuals of 10^{-3}. Figure 2.11a shows the streamwise profile of the streamwise velocity at the center line and Fig. 2.11b shows the spanwise profile of the streamwise velocity at y/D = 1.06.

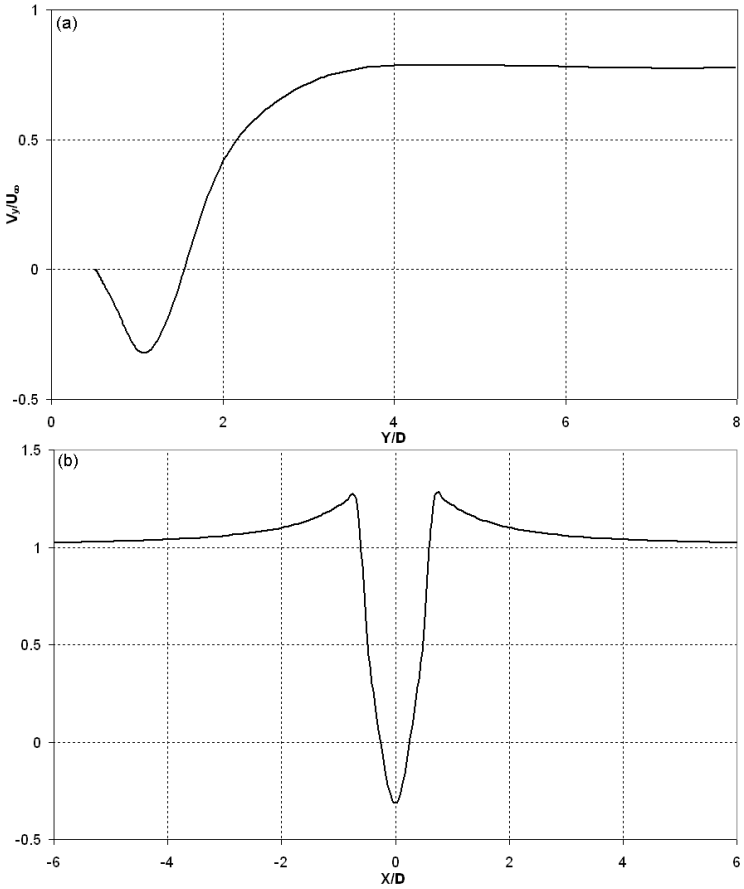

Figure 2.11 – Streamwise velocity on the (a) center line and (b) at Y/D = 1.06 in the wake of a circular cylinder under the case of boiler.

Here, the recirculation length, L_r/D = 1.06, is shorter than in the case of Re_D = 3900 as expected because of the low Reynolds, Re_D = 1000 based on the film temperature. Also, Fig 2.11b shows a residual of V_y/U_∞ = 1.04, the same value as the case of Re_D = 3900, due to the blockage effect.

The maximum y+ resulted in 0.67 with $-\langle C_{Pb} \rangle = 1.0$, which indicates that the flow is well resolved all the way down to the wall. According to Williamson (1996), under isothermal conditions for this Re_D of 1000, the back pressure coefficient should be 0.8, but the

cylinder cooling effects increase the turbulence resulting in a higher back pressure and lower recirculation length.

The instantaneous magnitude of vorticity and the local Nusselt number are shown in Fig 2.12

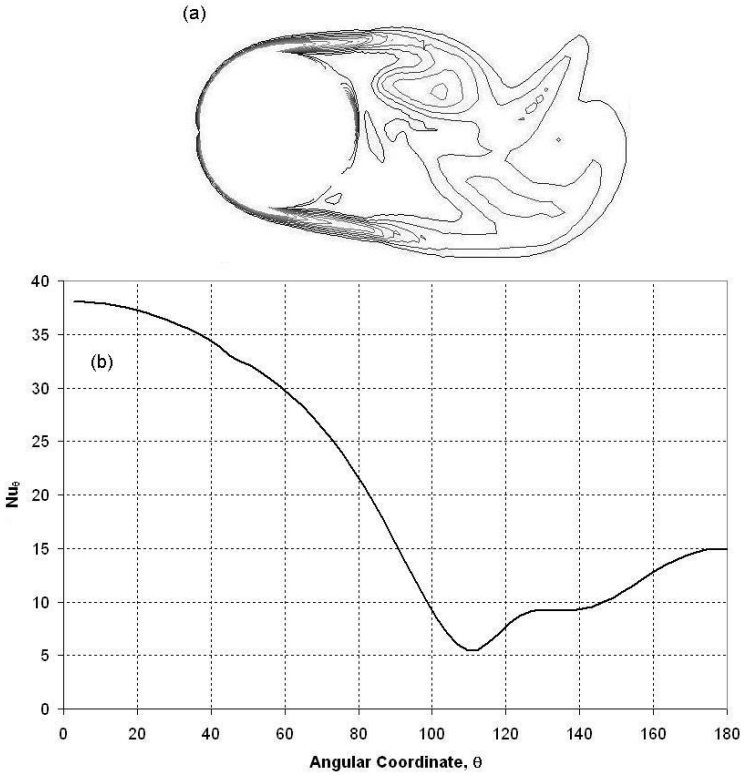

Figure 2.12 – (a) Instantaneous magnitude of vorticity $\omega D/U_\infty$ in the near wake at Re_D = 1000: 10 contours from 3 to 20 (b) Local Nusselt number around the cylinder.

In Fig 2.12a, it is clear that the turbulence intensity is much lower than that shown in Fig 2.10. Although the recirculation length is shorter than that for Re_D = 3900, the vortex formation is not so close to the cylinder wall. Also in Fig 2.12b, the local Nusselt number decreases from the stagnation point, with increasing θ as a result of the boundary layer development. The minimum, at 110°, indicates the boundary layer separation and the increasing of Nu_θ after it is associated with the

mixing promoted by the vortex formation in the wake, Incropera (1996). The resulting $\overline{Nu}_D = 20$, plus the correlation of Zhukauskas, *apud* Incropera (1996), is $\overline{Nu}_D = 15$ which is in the range of 25% of accuracy.

2.9.1 Particle Phase

Since the particle deposition can be very dependent on the inlet conditions, a parametric analysis was done in order to evaluate their effects. This parametric analysis was done using RANS because the CPU use is cheaper when compared with LES, and can provide good descriptions of the main physical effects. Since that RANS is not the subject of this work, further details of this parametric analysis can be found on Mendes *et al* (2007).

The Realizable κ–ε was chosen with QUICK discretization and enhanced wall function. The solid phase was described via Lagrangian approach and the global parameters with significant effects were the Reynolds number and the turbulent kinetic energy at the inlet plane, ranged from 750 to 2000 and 4 to 20 m^2/s^2, respectively. These inlet conditions were taken from Reinaldo (2004).

From a gas picnometry analysis, Berti *et al* (2007) calculated an apparent density of the ash particle close to 2460 kg/m^3, which is similar to the assumption of Bouris *et al* (2001) of 2300 kg/m^3, assuming that the ash particle density is close to that of Al_2O_3.

In the case of RANS a steady state simulation was done and particle diameters ranged from 1 to 200 μm following a Rosin Rammler distribution with $\bar{d} = 65.4\,\mu m$ and n = 1.23 based on experimental data. Due to the high computational cost, the particles were only injected in an area twice the size of the projected area of the cylinder in the flow direction. The center of this area was placed over the center of the inlet plane from the computational domain.

In the LES case, particles were released at each time step over one shedding cycle, with 1024 particles for each diameter per time step. Three diameters were chosen as being representative of the particle distribution, 30 μm with relaxation time of $2.81\ 10^{-3}$, 90 μm with τ_p of $2.53\ 10^{-2}$ and 200 μm with τ_p of $1.25\ 10^{-1}$. Their mass flow also followed the Rosin Rammler distribution with $7.07\ 10^{-4}$,$1.15\ 10^{-3}$, $2.75\ 10^{-4}$ kg/s respectively for each diameter. All particles were considered deposited once they reached the cylinder wall and this was considered not a change in the deposition. During real operations not all particles on this range are actual ash, probably most of the higher ones are still coke.

However, in this work they will all be considered ash particles. Figure 2.13 shows the particle deposition rate separated into two regions due to the size effects on each one as a function of the particle relaxation time.

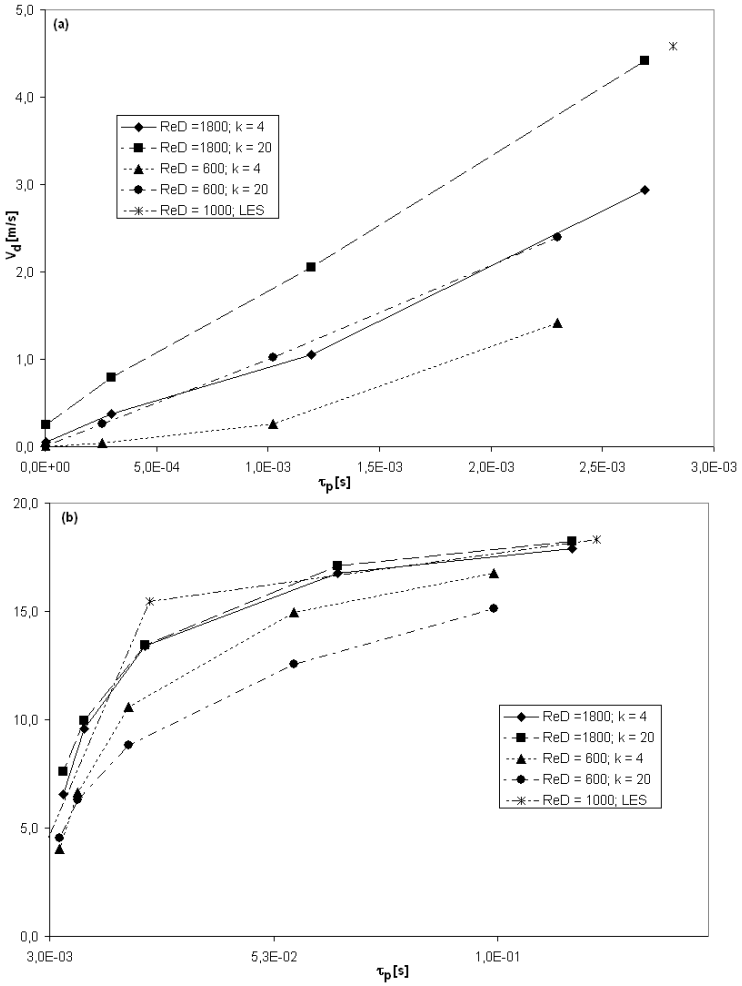

Figure 2.13 – Particle dep. rate on the circular cylinder. (a) Particles with τ_p lower than 3 10^{-3}; (b) Particles with τ_p higher than 3 10^{-3}.

The particle deposition rate, also known as deposition velocity, is defined as the flux of particles ratio at the deposition surface to the particle concentration (i.e. the number of particles per unit of volume)

Wang and Squires (1996). For a deposition of N_d particles on the wall from a total number N in time interval t, the deposition rate is then

$$V_d = \frac{N_d / A / t}{N / V} \tag{2.23}$$

where A is the deposition surface area and V the computational domain volume. In Fig. 2.13, the particle relaxation time, Eq. 2.22, is based on the assumption of Stokes regime and the fluid properties were taken at film temperature. As expected, the particle deposition rate increases with the increasing particle relaxation times.

As observed in Fig. 2.13, particles with relaxation times lower than $3\ 10^{-3}$ have a different behavior. In general because small particles tend to follow the streamlines and their tendency for depositing is lower than in the larger ones. Also in Fig. 2.13a, the effect in raising the Reynolds number from 600 to 1800 is the same as when raising the inlet turbulent kinetic energy from 4 to 20. The raising in the inlet kinetic energy possibly spreads the particles all around the domain more uniformly. Although this effect spreads all over the domain, in the region near the wall the raise in the inlet kinetic energy also raises the deposition of the small particles, indicating that small fluctuations near the wall promote a particle deposition with $\tau_p < 3\ 10^{-3}$.

In Fig. 2.13b it is shown that the inlet conditions, for a higher Reynolds, had no effect in the depositing of particles. However, with a low Reynolds number the raise in the inlet turbulent kinetic energy lowered the depositing particles with a higher relaxation time. Since the depositing particles with a higher relaxation time and low turbulent kinetic energy are possibly those that flow directly to the projected area of the tube, the raise in the inlet conditions gave them enough inertia to let escape from the streamline. This effect can also be a consequence of the inlet plane from which the particles were released, which means that the raise in the kinetic energy, compared to the inertia, deviated the trajectory from the circular cylinder. However, with higher Reynolds the inertia effect was probably higher and did not change the direction of the flow significantly.

In the LES case, the particles considered have a deposition rate comparable to those with higher Reynolds number from RANS which means that enough time elapsed indicating a steady state solution for the particles depositing.

Figure 2.14 shows the mean skin friction coefficient and the particle Reynolds number variation over the cylinder.

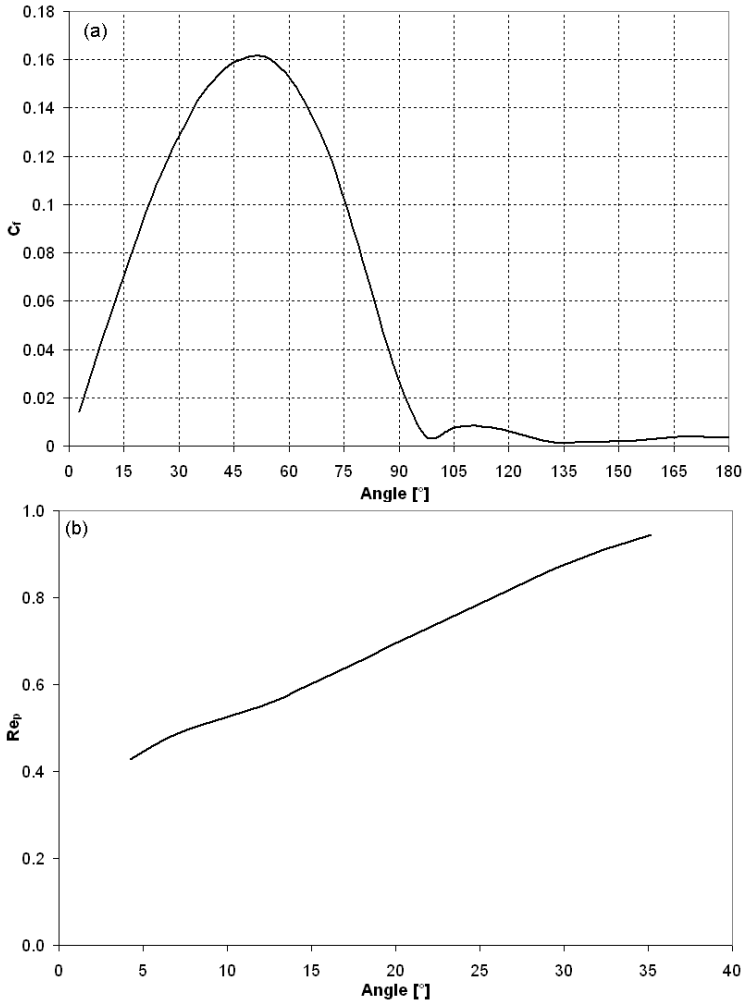

Figure 2.14 – a) Mean skin friction coefficient and b) Particle Reynolds number (30 μm) along the wall of the circular cylinder.

The particle's Reynolds number was defined in Eq. 2.18 and the mean skin friction coefficient is defined in Eq. 2.24

$$C_f = \frac{\tau_w}{0.5\rho v^2} \tag{2.24}$$

where τ_w is the wall shear stress and r and v are the density and velocity of the free stream reference. For particles with higher relaxation time,

such as 90 and 200 μm particles, Re_p is approximately constant over the entire deposition angle, resulting in 4 and 9 respectively. Because of the high inertia of those particles their motion is unaffected by the fluid stream. But for lower τ_p the Re_p changes such as the boundary layer develop, Fig 2.14b.

As the boundary layer develops, under a favorable pressure gradient, the fluid velocity gradient, normal to the wall, increases and, consequently, increases the mean skin friction coefficient until about 35°, Fig 2.14a. This raise in the fluid velocity gradient accompanied by a favorable pressure gradient produces a higher particle inertia and motion increasing its velocity. Beyond 35°, the fluid velocity gradient keeps increasing but slowly, it then starts to decrease, also under a favorable pressure gradient. Low τ_p particles have enough momentum to leave the boundary layer and follow the fluid stream. Probably, this is the reason why no particle of 30 μm was deposited beyond 35°.

2.10 Conclusions

This chapter presented the Large Eddy Simulation applied to the flow around a circular cylinder. Aiming to apply the LES approach to the ash deposition, a test case was considered in order to select the appropriate grid for a lower Re_D flow as is in the superheater tubes.

Several cases were analyzed and the LD2 run was chosen as suitable to simulate the steam generator tube bundle. This choice was made considering CPU time, and precision of the predicted velocity field around a circular cylinder.

Typical values of the flow in the region of superheater tubes were selected from previous works of Reinaldo (2004). The ash particle distribution was set as the in the power plant.

Ash particles with higher relaxation time have a higher particle deposition rate, as expected, due to their lower tendency to follow the streamlines around the cylinder. Also, these depositing particles showed a similar particle Reynolds number around the cylinder.

For the particles with lower relaxation time, Re_p showed a raising tendency to follow the curvature of the cylinder, owing to a favorable pressure gradient which increases the fluid velocity, accelerating the depositing particles.

CHAPTER 3 - SIMULATION AND CHARACTERIZATION OF ASH DEPOSIT

3.1 Introduction.

The growth of ash deposits involves several complex mechanisms, such as chemical surface reactions and vapor condensation, which play an important role in the final morphology of the interface and porous structure. However the application of simple rules, through discrete growth models, can mimic the essential physics that dictates the ash deposit growth. In this work, a computer model based on random and ballistic deposition was developed in order to simulate the porous structure of the ash deposit. The predictions were compared to measurements of pore size distribution, porosity and fractal dimension of a typical ash deposit. These characteristics were evaluated using the image software Imago developed at the Laboratory of Porous Media and Thermophysical Properties of the Federal University of Santa Catarina (LMPT/UFSC), Fernandes, (1994) and Philippi *et al* (2000). The images were taken with the scanning electronic microscope (SEM) at the Microstructure Characterization Laboratory (LCM/UFSC). Some chemical characterization was also done, including the analysis of oxides using the SEM and the X-ray diffraction pattern.

A similar characterization was presented by Clasen (2007), who used the same approach developed here to evaluate the initial stages of growth of the deposit.

3.2 Ash Deposit Characterization

This section presents the physical and chemical characteristics of a typical pulverized coal combustion ash deposit collected from the boiler. Both ash deposits, shown in Fig. 3.1, were collected from the first tube of the final superheater. The samples were collected from the front of the superheater tubes.

Figure 3.1 – A typical ash deposit from the superheater of Jorge Lacerda thermo power plant. The scale is marked in mm.

3.2.1 Physical Analysis

In order to characterize the ash deposit, a cross section in the flow direction was mounted in epoxy resin and then polished for analysis in the scanning electronic microscope (SEM). The SEM used is a PHILIPS XL 30 in the Microstructure Characterization Laboratory at UFSC. Twenty images were randomly collected following the base, bottom, the deposit, at the external surface of the tube, and the top of the deposit, subjected to the gas flow. All the images were analyzed with the Imago software developed by LMPT (Laboratory of Physical Properties and Porous Material) at UFSC to characterize the porous microstructure. Originally the software was developed for the petroleum industry with the objective of analyzing reservoir porous rocks, Damiani *et al* (2000).

Scanning electron microscopy (SEM) employs back scattered electron imaging (BEI) as the back scattered electrons provide a significant contrast in the image because their intensity varies with average atomic number. Since the mineral or ash particles appear brighter in BEI in relation to substances with lower atomic number elements, a distinction can be made between epoxy and mineral matter, Bryers (1996). Figure 3.2 shows a sample collected from the ash deposit. In this picture, the darker finer grained regions are the epoxy resin, while the lighter smoother regions are the mineral particles. Notice that the mineral particles present voids that resemble closed, i.e., isolated, porosity.

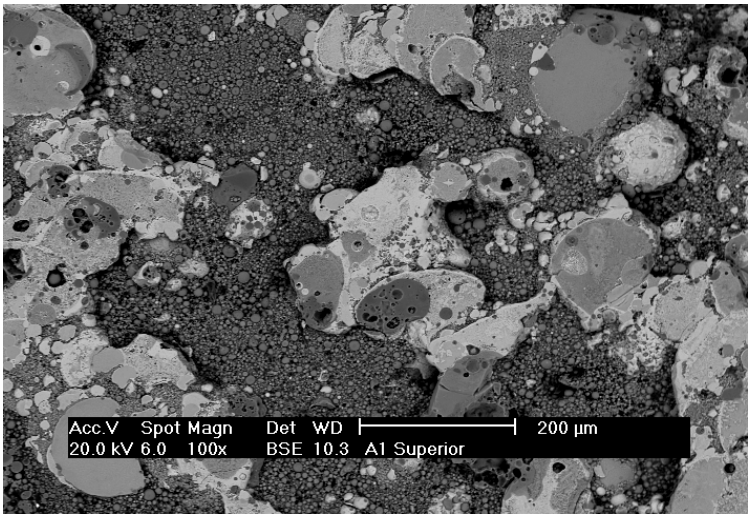

Figure 3.2 – Typical image collected from the ash deposit using SEM.

As shown in Fig. 3.2, the magnification used is 100x, which leads the resolution of 1 pixel to be equivalent to 1.3 µm. From the image treatment applied by the Imago software a pore size distribution can be obtained. In Fig. 3.2 we notice that the pores have highly irregular shapes. Imago assumes that the pore size is the diameter of the circle that can be subscribed within the given pore volume, this technique is known as $d_{3\text{-}4}$ metric and will be described further in the text. Figure 3.3 shows the pore size distribution expressed as cumulative volume to the right (the points connected by line) and frequency to the left (the points not connected by lines) as a function of pore size expressed in pixels. The cumulative volume at a given pore size d_i is the sum of the volumes of all pores with sizes smaller than d_i. The open circles represent the base, i.e., the region of the deposit closer to the tube surface, and the crosses represent the top of the deposit, i.e., the region of the deposit closer to the gas flow.

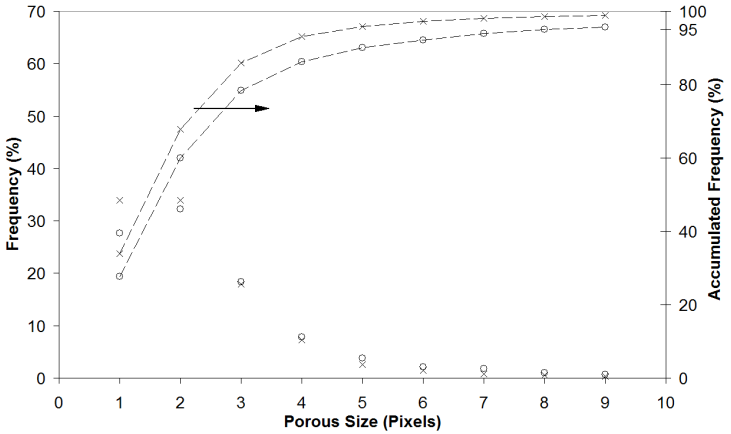

Figure 3.3 – Pore size distribution of a typical ash deposit, where the open circles represent the base, i.e., the region of the deposit closest to the tube surface. The crosses represent the top of the deposit, i.e., the region of the deposit closest to the gas flow.

As shown in Fig. 3.3, the base region, with 28% porosity, 95% of the pore size is in the range of 1 to 8 pixels (close to 1 to 12 μm), while in the top region, with 26% porosity, 95% is in the range of 1 to 5 pixels (close 1 to 6 μm). This indicates that there is a transition from a clustered region in the base to a more sintered region in the top, probably due to the higher temperature closer to the gas flow. The higher temperature induces higher sintering leading to smaller porosity and smaller pore sizes. This temperature gradient also induces different phase transitions highlighted by the chemical analysis which shows a difference in the composition between the base and top of the deposit.

The fractal dimension was determined using the self-correlation method for all the collected images. In average, a fractal dimension of 1.75 was found in both regions which represent no difference concerning the morphology of the porous structure between the base and top regions.

3.2.2 Chemical Analysis

The SEM is also coupled with an energy dispersive X-ray (EDX) detector which allows the quantitative analysis of the equivalent oxides present in the ash deposit. The results are shown in Tab. 3.1.

Table 3.1 – Average oxide weight percentage of a typical ash deposit.

Elements	Average Weight (%)	
	Top	Base
Na_2O	0.33	0.35
MgO	1.14	0.96
Al_2O_3	18.97	18.73
SiO_2	37.73	31.04
K_2O	1.43	1.24
CaO	4.31	3.51
Fe_2O_3	36.10	44.16

The difference between the base and top regions regards, mainly, in the SiO_2 and Fe_2O_3 concentration. The high content of Fe_2O_3 in the base indicates a possible diffusion from the tube to the deposit due to the high temperature gradient. In the SiO_2 case, the high content on the top is due to the highly external molten layer of the ash deposit, which has a high capture efficiency of the fly ash particles capturing the heavy particles after the deposit has grown. Similar conclusions were advanced by Wang *et al* (1999).

Another qualitative chemical analysis was done via X-ray diffraction, (XRD). The XRD technique consists on the detection of diffracted photons resulting from the incident radiation on milled samples. X-ray diffraction represents an interaction phenomenon between the incident X-ray and the electrons of the sample. In a material where the atoms are periodically arranged in space, which is one of the characteristics of the crystal structures, the X-ray diffraction occurs in all scattering directions, following Bragg's law, Eq. 3.1.

$$n\lambda = 2d\sin(\theta) \tag{3.1}$$

where n is an integer, λ is the X-ray wavelength, d is the spacing between the crystalline planes and θ is the angle between the incident ray and the scattering planes.

The diffracted beam produces a pattern of peaks that can be distinguished from the background registered in the intensity spectrum versus the angle 2θ (or d), constituting the standard diffraction spectrum. Each element can be identified by the relative intensity of the peak and the angle in which it appears. A disadvantage of this method is that the relative intensity of different elements can be superimposed. The individual standards are available at the ICDD (International Center for Diffraction Data) JCPDS (1981). All the samples were analyzed in a

Philips Xpert provided with a tube copper (λ = 1.54056 Å) and n = 1. The XRD pattern of the ash deposit is shown in Fig. 3.4.

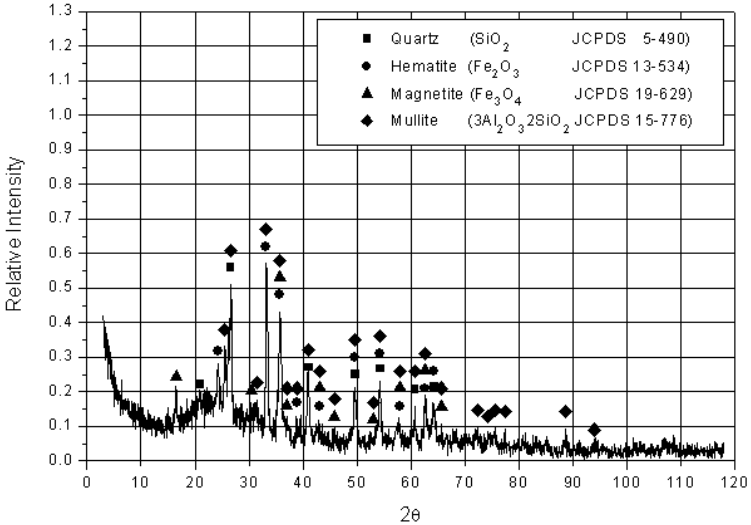

Figure 3.4 – X-ray diffraction pattern for the ash deposit.

Figure 3.4 shows the oxides present in the ash deposit by comparing them with standard intensity along the 2θ axis: Quartz (SiO_2 JCPDS 5-490), mullite ($3Al_2O_32SiO_2$ JCPDS 15-776), hematite (Fe_2O_3 JCPDS 13-534) and magnetite (Fe_3O_4 JCPDS 19-629). From the elements found in the ash deposit, attention should be paid to mullite. According to Wang *et al* (1999), mullite is expected to precipitate from the aluminosilicate amorphous phase and it is the main responsible for the insulation of the ash deposit due to its low thermal conductivity. This insulation leads to additional sintering due to the higher temperatures reached at the top layer.

3.3 Modeling of Growth of Ash Deposit

3.3.1 Growth Models

The formation of the solid-gas interface within and on the surface of the ash layer is influenced by a large number of factors, making it very difficult to distinguish the individual effects. A few simple rules, however, can be applied to mimic the growth of the ash deposit. Two of these rules are known as the ballistic and random deposition. These

models generate a deposit from which it is possible to evaluate some of the characteristics of the growth process without direct contact with the large number of factors that influences the growing behavior.

3.3.1.1 Ballistic Deposition (BD)

In this procedure, a particle is released from a randomly chosen position above the surface, located at a distance far from the most elevated point of the surface. The particle follows a straight vertical trajectory until it touches and sticks to the nearest occupied neighbor, Barabási and Stanley (1995). The time unit is chosen to correspond to a certain quantity of deposited particles, which means that each time step corresponds to a number of particles deposited. Figure 3.5 presents a rendering depicting two possible outcomes for two particles released in different points above the surface.

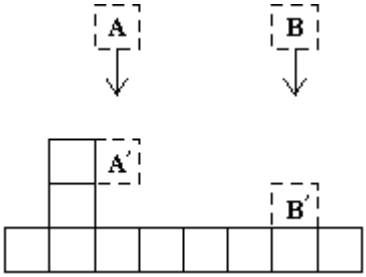

Figure 3.5 – Ballistic deposition model, adapted from Barabási and Stanley (1995).

The particle sticks to the first site along its trajectory that has an occupied nearest neighbor. According to this deposition rule, particle A attaches to site A', while particle B attaches to site B', Barabási and Stanley (1995). Both A' and B' become part of the aggregate and define the new contour of the surface.

3.3.1.2 Random Deposition (RD)

Random deposition is the simplest of the growth models. In this method, a particle is released from a randomly chosen site over the surface, it then falls vertically until it reaches the top of a column, whereupon it is deposited. Figure 3.6 illustrates two particles dropped from random positions above the surface and deposited on the top of a column directly under them.

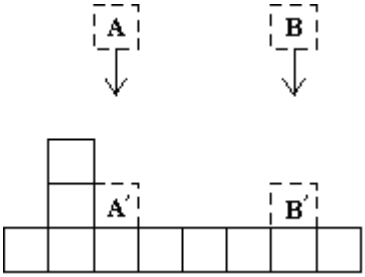

Figure 3.6 – Random deposition model, adapted from Barabási and Stanley (1995).

In RD, the columns grow independently, as there is no mechanism that can generate correlations along the interface. In BD, the fact that particles are capable of sticking to the edge of the neighboring columns leads to lateral growth, allowing the spread of correlations along the surface, Barabási and Stanley (1995).

A similar approach was proposed by Kamarkar *et al* (2005). However, instead of depositing one single square particle, rectangular parallelepiped grains of two different sizes on a cubic lattice with unity spacing are used. The smaller grain has dimensions of 1x1x1 and the larger, of 2x1x1. The inclusion of the longer grains causes gaps to be left in the structure that forms the pores. A porous structure is created with a porosity that is a function of the probability of occurrence of the large particles, Kamarkar *et al* (2005). The near neighbor is not taken into account, just like the RD, and the porous structure is generated only due to the longer grains. This approach is used here in order to compare the porous structure generated by this simple model with a typical ash deposit.

3.3.2 Scaling Relationship

Some essential properties of a growth process can be described by introducing some scaling relationships.

The surface is defined as the set of particles in the aggregate that are highest in each column. To describe the growth quantitatively, the concept of mean height and interface width is introduced, Barabási and Stanley (1995).

The mean height of the surface, $\bar{h}$, is defined by:

$$\bar{h}(t) = \frac{1}{L}\sum_{i=1}^{L} h(i,t) \qquad (3.2)$$

where h(i,t) is the height of column i at time t and L is the number of columns. If the deposition rate (number of particles arriving at a site) is constant, the mean height increases linearly with time:

$$\bar{h}(t) \approx t \tag{3.3}$$

The unity time is chosen to correspond to the deposition of L particles on the interface, where L is the system size, or the number of columns.

The interface width, w(L,t), which characterizes the roughness of the interface, is defined by the rms fluctuation in the height and is given by:

$$w(L,t) = \sqrt{\frac{1}{L}\sum_{i=1}^{L}\left[h(i,t) - \bar{h}(t)\right]^2} \tag{3.4}$$

To quantitatively monitor the roughening process, the interface width is measured as a function of time. By definition, the growth starts from a horizontal line, at which the interface width is zero.

A typical plot of the time evolution of the surface width has two regions separated by a crossover time, t_x, Fig. 3.7:

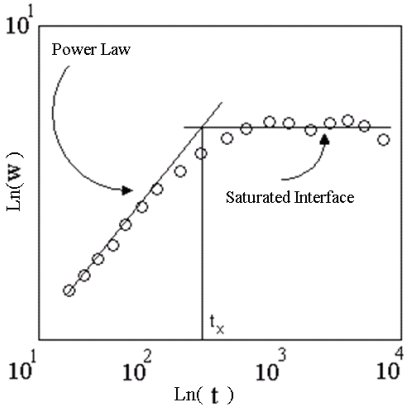

Figure 3.7 – Growth of the interface width with time for the BD model, adapted from Barabási and Stanley (2005).

Figure 3.7 describes a typical time evolution of the interface width of the ballistic deposition model. Two characteristic regimes are noticed, the power law growth, which appears as a straight line on the log-log plot, and the saturation regime, for which the interface width does not change with the passage of time.

In the power law regime, the width increases as a power of time:

$$w(L,t) \sim t^{\beta} \qquad t \ll t_x \tag{3.5}$$

The exponent β, or growth exponent, characterizes the time dependent dynamics of the roughening process. The growth of the interface width does not continue indefinitely, but is followed by a saturation regime during which the width reaches a saturation value, w_{sat}. The saturation width clearly depends on the size of the system, L. As L increases, the saturation width increases as well, and the dependence is also assumed to follow a power law:

$$w_{sat}(L) \sim L^{\alpha} \qquad t \gg t_x \tag{3.6}$$

The exponent α, which is called the roughness exponent, is a second critical exponent that characterizes the roughness of the saturated interface.

The crossover time, t_x, also known as saturation time, characterizes the moment at which the interface crosses over from the behavior of the power law regime to the saturation regime. It is a function of the system size, as

$$t_x \sim L^{z} \tag{3.7}$$

where z is called the dynamic exponent.

The scaling exponents are not independent. Instead, when plotting the $w(L,t)/w_{sat}(L)$ as a function of t/t_x, the curve reaches saturation at the same characteristic time, which suggest that

$$\frac{w(L,t)}{w_{sat}(L)} \sim f\left(\frac{t}{t_x}\right) \tag{3.8}$$

Replacing w_{sat} and t_x with their relations, one can obtain the Family Vicsek scaling relation, Barabási and Stanley (1995), which can be expressed as

$$w(L,t) \sim L^{\alpha} f\left(\frac{t}{L^{z}}\right) \tag{3.9}$$

Also, at the same crossover time, t_x, Eqs. 3.5 and 3.6 should result in the same interface width, $t_x^{\beta} \sim L^{\alpha}$ and from Eq. 3.7 it comes that:

$$z = \frac{\alpha}{\beta} \tag{3.10}$$

Equation 3.10 is a scaling law linking the three exponents that are valid for any growing process that obeys the scaling relation of Family Vicsek.

For the models described here, ballistic deposition and random deposition models, it is not enough to let them grow until their porosity does not change with time, because the elapsed time is not enough to reach the saturation of the interface. In other words, at this time all the sites are not yet correlated.

3.3.3 Fractal Dimension

The morphology of ash deposits can be poorly defined within the scope of Euclidean geometry. However, when a sufficient number of particles have been deposited, it may be possible to describe these structures in terms of a non-integer or fractal dimension, D_f, which is equal to or less than the Euclidean dimension, D_E, of the space in which the structure is embedded, Mandelbrot, (1998).

In order to estimate the fractal dimension, the box counting method or box dimension is used, which is equivalent to the Hausdorff-Besicovitch dimension, and consists of covering any non-empty bounded set F by a box of size δ. Let $N_\delta(F)$ be the smallest number of sets of diameter δ which can cover F. Then, $N_\delta(F) \sim \delta^{-D_f}$ such that:

$$D_f = \lim_{\delta \to 0} \frac{\ln\left(N_\delta(F)\right)}{\ln\left(1/\delta\right)} \tag{3.11}$$

Here, it is assumed that $\delta > 0$ and sufficiently small to ensure that $\ln(1/\delta)$ is always positive. Falconer (1990) also provides a definition of the meaning of the box dimension. To find the box dimension of a plane set F, we draw a mesh of squares or boxes of side δ and count the number $N_\delta(F)$ that overlaps the set for various small values of δ (hence the name 'box counting'). The box dimension is the logarithmic rate at which $N_\delta(F)$ increases as $\delta \to 0$, and may be estimated from the gradient on the log ($N_\delta(F)$) vs. -log (δ) graph. The number of mesh cubes of side δ that intersect a set is an indication of how spread out or irregular the set is when examined at scale δ. The dimension reflects how rapidly the irregularities develop as $\delta \to 0$.

As we can appreciate, this dimension is promptly applied to the porous structure in order to characterize its pore spread in the structure analyzed. Also, it is easily implemented in the code developed here since it places the particles at the points of a regular lattice, enabling easy counting and measurement. The same approach was applied by Fernandes (1994) to a cement mortar. Another approach to the fractal dimension is via self correlation. It is obtained from the normalized

covariogram, which gives the probability of two elementary cells separated by a distance u to belong to the same structure (void or solid fraction). The statistical values of covariograms are obtained by displacing half the image over itself. It ranges from ϕ, for a null displacement, to ϕ^2, for large displacements, Fernandes (1994). The fractal dimension is obtained from the slope of the linear part of the resulting curve ln(C(u)) versus ln(displacement), where the displacement is measured in pixels. Fernandes (1994) compared the fractal dimension obtained through self correlation and through the box counting method obtaining similar results for a self similar structure.

The use of fractal dimensions to characterize complex structures, such as porous media, is widespread, Mandelbrot (1998) and Falconer (1990). Attempts to relate the fractal dimension to the structure of coal are available in Xu *et al* (1997) and Song *et al* (2004). Xu *et al* (1997) estimated the fractal dimensions of coals and cokes via adsorption methods, and Song *et al* (2004) estimated the fractal dimensions based on scanning electron microscope (SEM) images.

Is this work, the fractal dimension from a typical ash deposit was estimated via self correlation with SEM images of the ash deposit. Song *et al* (2004) estimated the fractal dimension from SEM images of coals by the Xie method, which consists of covering a SEM image with small squares with a small scale of $\delta x \delta$. In this way the projected area of these small squares, on the SEM image can be correlated via the gray scale with the area of the full image.

The work of Song *et al* (2004) aimed to describe the surface of the internal char during the combustion process leading to a relation between the pore reacted area and the burn off ratio. This work is a departure from Song *et al*. (2004) because the focus here is the relation between the void and the solid phase and how spread the pores are in the porous structure.

3.3.4 Pore Size Distribution

The pore size is determined by comparing the pore with a previously defined standard object of size and form. The basic idea is to compare each pore of a deposit to a known object (structure element). To this end, the mathematical operations named erosion and dilatation of the objects are used, Fernandes (1994).

An object that suffers erosion by losing a structure element can be represented by a set of points resulting from the subtraction of the object by the structure element, starting at the outer borders and moving

towards the geometric center of the object. The dilatation process operates in the reverse way. Actually, these operations use a circle as the structure element, and the results are expressed by real numbers, which require a huge computational effort.

To overcome this difficulty, a quasi-Euclidean geometry is used. Instead of using a circle, it is possible to use an octagon in a metric known as $d_{3\text{-}4}$, which is very similar to the circle, and its main advantage is the possibility of working with integer numbers, Fernandes (1994). This metric is illustrated in Fig. 3.8.

$\sqrt{2}$	1	$\sqrt{2}$
1	P	1
$\sqrt{2}$	1	$\sqrt{2}$

4	3	4
3	P	3
4	3	4

Figure 3.8: Local weights for the octagonal structure element.

The method consists in applying a displacement of 1 in the vertical and horizontal directions, and a displacement of square root of 2 in the diagonals, which is approximately 4/3, in order to represent the structure element as an octagonal. Now, the algorithm can move along the lattice with a displacement proportional to 3 in the vertical and horizontal directions and 4 in the diagonals, Fig. 3.9 represents some structure elements that can be used in the process of eroding and dilatation on the image.

To measure the frequency of the pore with size 1, it is eroded by a structure element with radius 1 moving with the metric $d_{3\text{-}4}$. After that, the resulting object is dilated by the same structure element and the resulting pore volume is measured and compared with the original volume of the structure. The fraction of the pore with size smaller or equal to the radius of the structure element is then obtained. For more details, refer to Fernandes (1994). Some examples of pore sizes, under the $d_{3\text{-}4}$ metric, are illustrated on Fig. 3.9 and an overview of the algorithm described here is illustrated on Fig. 3.10.

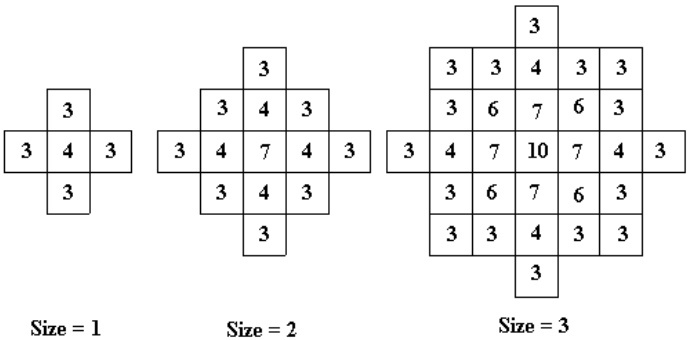

Figure 3.9 – Structure elements with sizes 1, 2 and 3, adapted from Fernandes (1994).

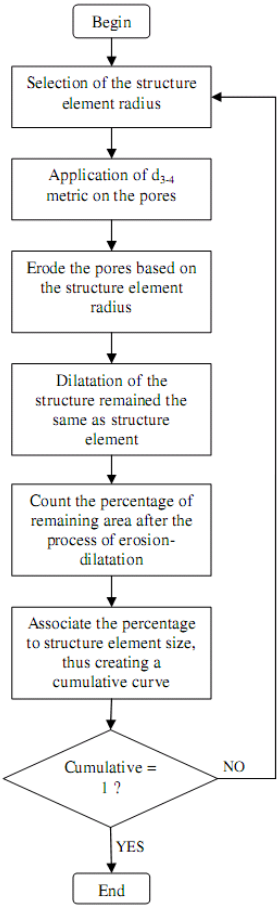

Figure 3.10 – Overview of the algorithm used on the pore size distribution, adapted from Fernandes (1994).

3.4 Prediction of Ash Deposit

3.4.1 Single Trajectory Particle Deposition Model

The approach used in the Single Trajectory Particle Deposition Model is the same described by Kamarkar *et al* (2005). Two particles with size 1x1 and 2x1 are released from a distance far from the surface. Those particles are ruled by the Random Deposition approach, by which the particle does not stick to the nearest neighbor as in the Ballistic

Deposition approach, but instead the formation of the porous structure is done by the particle with size 2. Fig. 3.11 illustrates this process.

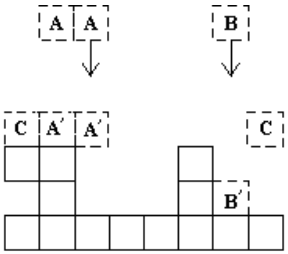

Figure 3.11 – Structure generated by Single Trajectory Particle Deposition Model with periodic boundary conditions

The substrate is linear and the longer axis of the particle is taken along the surface direction. The time step corresponds to that needed for the deposition of L particles. As usual, periodic boundary conditions are applied to the lateral boundaries, which mean that the structure located at the left border is connected to the right border. Figure 3.11 illustrates this situation, size 2 particle C is located both on the left size as on the right size of the porous structure. It is assumed that once the particle reaches the surface it remains frozen in that position. In this sense, the particle is not allowed to reach the position that would provide the minimum free surface energy. Also, the choosing probability of the 2x1 particle was initially 1/3.

The deposit was let to grow until a time corresponding to a saturated deposit of maximum height (h_{max}) of 1,000 L for L = 32, 64 and 128. At each time step, the mean height, interface width and porosity of the ash deposit were calculated. The characteristics of the deposit were estimated using 600 independent samples.

As pointed out by Kamarkar *et al* (2005), two different regimes were observed for the interface width. Initially, the surface evolves in time in a typical uncorrelated regime, and after some time, it becomes correlated. Figure 3.12 illustrates the two different values of the growth exponent, $\beta_1 \sim 0.48$ and $\beta_2 \sim 0.28$.

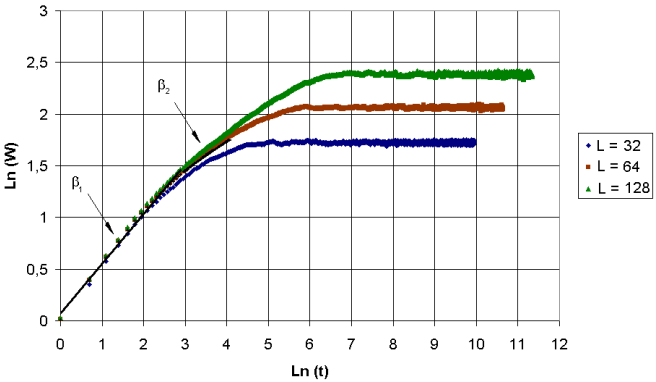

Figure 3.12 – Unscaled fit of width versus time in the particle deposition model.

The saturation widths are 1.70, 2.03 and 2.38 for L = 32, 64 and 128 respectively. The resulting roughness exponent, from Eq. 3.6, obtained from this analysis is $\alpha \sim 0.49$, which is very close to the exact value (1/2) for the ballistic deposition model, Barabási and Stanley (1995). Note that, although the deposition of particles follow a random deposition model, the final result is a deposit similar to the one generated by a ballistic deposition, Kamarkar *et al* (2005). The identification of both regimes, random and ballistic behavior, occurs because there is a competition among the particles of size 1 and 2 that are being deposited. Also the dynamic exponent obtained was $z \sim 1.7$, which is 13% higher than the corresponding value (3/2) found for the ballistic deposition. Certainly, these differences are due to the poor statistics, 600 independent simulations, which is characterized by the noise in Fig. 3.12.

The resulting porosity stabilized at 34% and was calculated by the ratio between the volumes of particles deposited and the volume of the whole deposit. The fractal dimensions obtained through the box counting method is 1.72, 1.79 and 1.83 for L = 32, 64 and 128, respectively. The maximum difference in fractal dimension is about 6%. The pore size distribution over the averaged samples is shown in Fig. 3.13.

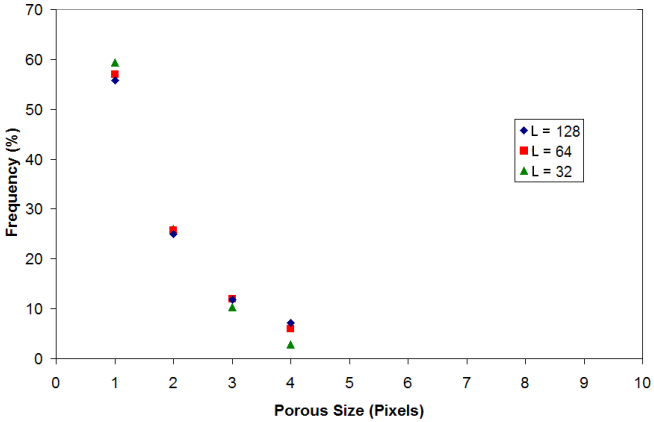

Figure 3.13 – Pore size distribution for Single Trajectory Particle Deposition Model.

No significant differences can be observed in the pore size distribution for all the substrates analyzed here. All the simulations based on the ballistic deposition model proposed by Kamarkar *et al* (2005) resulted in similar structures, with slightly different fractal dimensions. Once the fractal dimension can be interpreted as the spreading of the irregular objects embedded in an Euclidean dimension, the fractal dimension calculated indicates that the larger the substrate sizes, the more spread the pores are. This fact has a very important consequence, especially in the heat transfer mechanism in the porous media, as will be explored in the next chapter.

In order to evaluate the influence of the input data, the probability of choosing particles of size 2 were varied from 5 to 95%, for a substrate size of 32, 64 and 128. The results are shown in Fig.3.14.

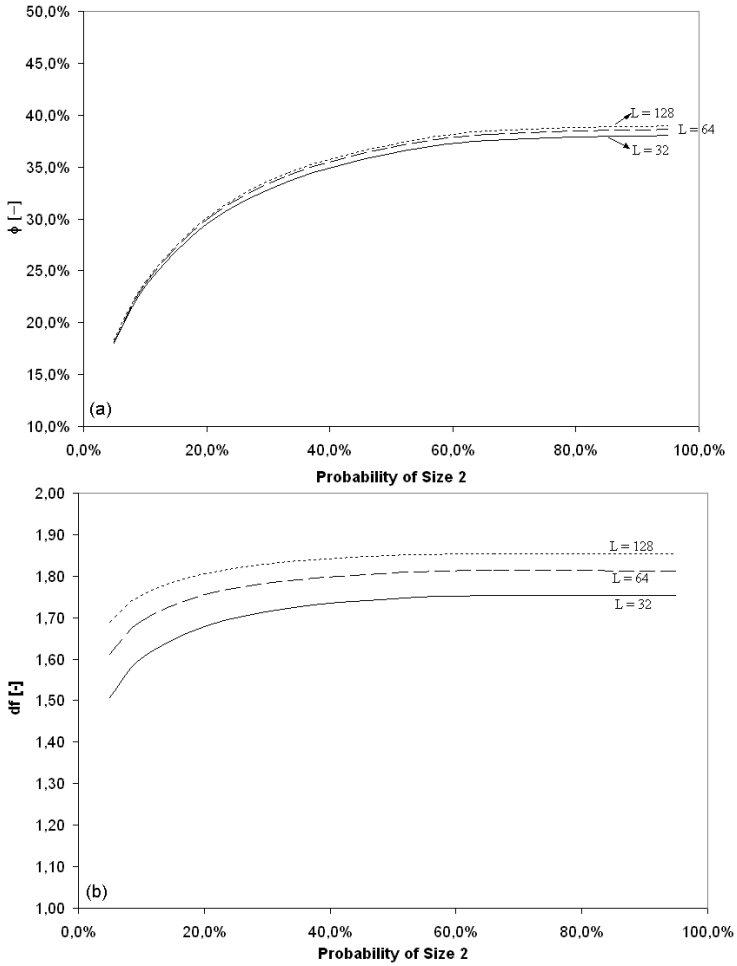

Figure 3.14 – (a) Porosity and, (b) fractal dimension of porous structure as a function of probability in choosing particle with size 2.

As shown in Fig. 3.14a the porosity changes less than 20% while the probability of the particle with size 2 changes from 5% to 95%. This can be explained because, since the particles are released from a randomly chosen position and follow a straight vertical path until they reach the surface, it is expected that the model results in the same behavior for all the substrates. Also, since the sticking property depends on the particle size, for a very small probability of particles with size 2, the model tends to behave more like a random deposition. While for a

high probability of particles with size 2, the model tends to follow the ballistic deposition behavior with a limited porosity of 40%.

In Fig. 3.8b, the fractal dimension follows the same tendency as the porosity, except that the difference between the results for the three substrate sizes increases to values from 15% to 8%. This difference is probably due to the higher spreading area of the substrate, since the higher the length of the substrate, the lower is the effect of the periodic boundary condition. Also, although not shown here, the frequency of pores with size 1 increases as the probability of particles with size 2 increase. This was expected since the particle with size 1 should fill the pores generated by the particle with size 2.

3.4.2 Random Trajectory Particle Deposition Model

From the results obtained above with the Kamarkar *et al* (2005) model, the saturation porosity reaches values of the order of 40%, while the measured values for the porosity of ash deposits are around 26-28%. So, in order to lower the predicted porosity to values closer to a typical ash deposit, the Kamarkar *et al* (2005)model was modified. The modification proposed allows the particles released to follow different trajectories besides the normal direction of the substrate and it is called the Random Trajectory Particle Deposition Model. This modification allows particles to fill adjacent pores, lowering the porosity of the resulting structure. The same parameters used above are also used for predictions with the Random Trajectory Particle Deposition Model, however, to reduce the computational effort, calculations were performed only for substrates with sizes L = 32 and 64. The inclination of the trajectories is randomly chosen from a normal distribution with average of 0º and standard deviation of 10º measured from the normal direction.

Based on the predictions, the resulting porosities stabilized at 20% and 28% with a fractal dimensions of 1.58 and 1.75 for L = 32 and 64 respectively. As expected, the resulting porosity reached a lower value when compared with the original model. Also, a low value of fractal dimension was found, for both substrates, which indicates that the Random Trajectory Particle Deposition Model tends to generate a more irregular porous structure than the Kamarkar *et al* (2005) model. The pore size distribution over the averaged samples is shown in Fig. 3.15.

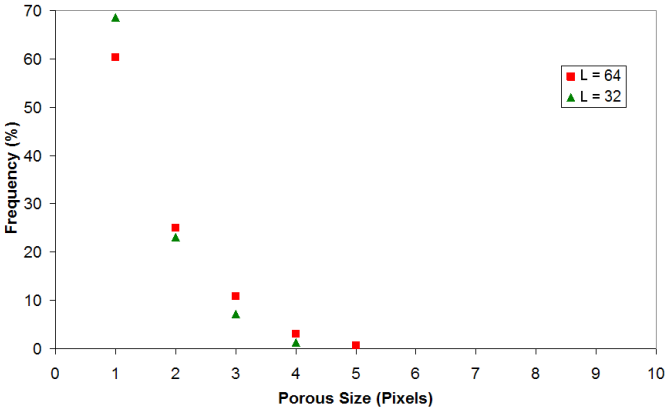

Figure 3.15 – Pore size distribution for Random Trajectory Particle Deposition Model.

Comparing the pore size distributions generated from both models, no difference can be seen, except for the pore size 1, which is more frequent in the Random Trajectory Particle Deposition Model.

As for the growing exponents, differently from the results pointed out by Kamarkar *et al* (2005), the two different regimes found for the Kamarkar *et al* (2005) model were not found in the Random Trajectory Particle Deposition Model. Actually it was found that $\beta \approx 0.3$, which is only 10% different from the exact value of the ballistic model. It is believed that the inclined trajectories speed up the saturation regime, not allowing competition between the two types of particles that are being deposited. As identified in the Kamarkar *et al* (2005) model.

Concerning the roughness exponent, it resulted in $\alpha \approx 0.34$, which is 35% smaller than the exact value of 0.5. Again, it is believed that the poor statistics are responsible for this difference.

In order to evaluate the influence of the particle probability, the probability of choosing particles with size 2 was changed from 5 to 95%, with two probability curves for the trajectory angle with 0° average and 10° and 20° of standard deviation respectively, for substrate sizes of 32 and 64. The results are shown in Fig.3.16. The wavy like form of the curves is attributed to the fact that only 50 realizations of each probability were calculated. This results in a data population too small to average out the mean.

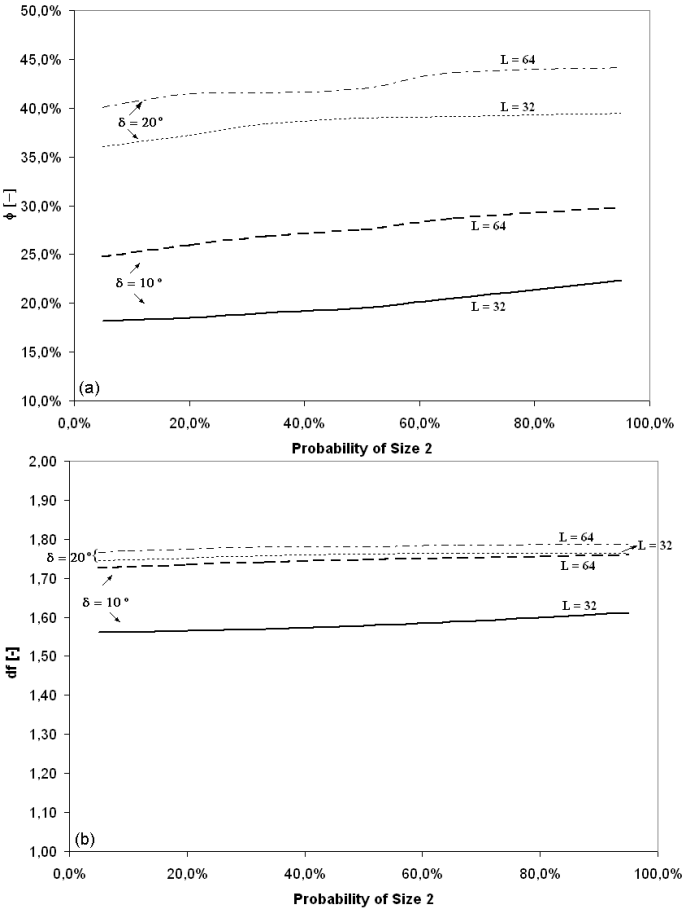

Figure 3.16 – (a) Porosity of porous structure, (b) Fractal dimension of porous structure as a function of probability of choosing particle with size 2.

Differently from the results of the Kamarkar *et al* (2005) model, Fig. 3.16a shows an increase of only a 5% in porosity as the probability of choosing a size 2 particle increased. Instead, the results of the Random Trajectory Particle Deposition Model are more sensitive to the substrate size. There is a 7% change as the substrate size is changed from 32 to 64 with a 10º of standard deviation and 4% as the substrate size is changed from 32 to 64 with a 20º of standard deviation. As the standard deviation of the probability distribution of trajectory angle increases, the difference in porosity for the two substrate sizes

decreases, leading to the same porous structure. The resulting pore size distribution is similar to the one presented in Fig 3.15.

3.4.3 Three-Dimensional Particle Deposition Model

The formation of deposits is affected by a large number of factors. The particle deposition models used so far have allowed the generation of a porous structure that resembles a typical ash deposit. However, the particle laden flow field in coal combustion presents particles with diameters ranging from 1 to 200 μm with different depositing velocities.

In this section, a model that takes into account particle-size and velocity distribution is developed in a three-dimensional space. In this model, named Three-Dimensional Particle Deposition Model, each particle is represented by a group of pixels, like the ones shown in Fig. 3.9. For instance, the size 2 particle is represented by a group of 13 elements, or pixels, in a 2D plane which leads to a serious drawback namely the need for a large allocated memory to store the surface and the particles being deposited. This allows for the predictions, although the size of the simulated deposit must be kept small, it still needs to be large enough to be representative of a typical ash deposit. To reach this compromise, a characteristic length based on the self correlation is considered.

As described in Section 3.3.3, the self correlation is related to the fractal dimension by the slope of the linear part of the probability curve of two elementary cells separated by a distance that pertains to the same structure versus the displacement. The average characteristic length of the typical ash deposit analyzed here is 100 pixels. Since the model considers periodic boundary conditions, the substrate length was set at 1,000 pixels. This size is assumed to be enough to avoid the boundary influence, as well as to recover the characteristic length on the self-correlation function once the deposit has reached saturation.

In order to approximate the particle-laden flow conditions presented in Chapter 2, the simulation was run in 3D with diameters of 30, 60 and 200 μm with average relative velocities, normal to the substrate, of 1.2, 3.3 and 3.8 m/s in the streamwise direction, 0.3, 0.1 and 0.05 m/s in the crosswise direction and close to 1e-5 m/s in the spanwise direction, respectively, for each particle diameter. These values were taken from LES simulations run on Chapter 2.

The substrate was considered as a square plane and the release position of each particle was randomly chosen above the highest site of

the structure. The model is set as a direct extension of the previous approaches and, as described in Section 3.4.1, it does not allow any kind of change in the structure, since the particle is deposited. Figure 3.17 shows an example of the structures obtained with this assumption. In this figure, the numbers represent the diameter of the particle. We can notice a size 3 particle hanging from a size 2 particle which is, hanging from a column formed by particles with size 1. This structure is probably unstable when subjected to flow conditions. Depending of the kinetic energy of the size 3 particle the structure should be rearranged or broken back into the flow. These events are not present in this model and are left for a future work.

As a result of the presence of structures such as that pictured in Fig 3.17, the averaged porosity from 200 realizations reaches 85%, which is well above the porosities observed in ash deposits.

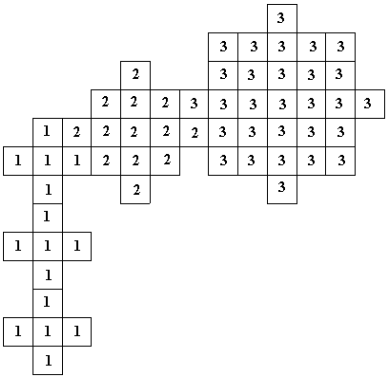

Figure 3.17 – Consequence of the assumption of non restructuring.

This approach is probably the best suited to model all the physical phenomena involved in the deposition and surface growth. However, it requires an improved approach regarding particle sticking and rearranging in order to avoid the situation described in Fig 3.17. These improvements are not developed here and are left as recommendations for future work.

Comparing the results found for a typical ash deposit with those from the Single Trajectory Particle Deposition Model and Random Trajectory Particle Deposition Model, we can see that the pore size distribution presents a higher frequency of size 1 than that presented in the ash deposit in all cases simulated here. The Random Trajectory Particle Deposition Model with a substrate size of 64 best represented

the ash deposit with a fractal dimension of 1.75 and porosity of 28%, but failed to represent the pore size distribution. This indicates that it is necessary to improve the rearrangement of the particles in the porous structure generated by this model.

3.5 Conclusion

The porosity, pore size distribution and fractal dimension of a typical ash deposit were measured using SEM image, treated with the Imago software, and the presence of ceramic phases were quantified using EDX detection and X-ray diffraction. Samples were taken from the top layer of the deposit, i.e., closer to the gas flow, and bottom layer of the deposit, i.e., closer to the tube. The measurements pointed out differences in pore sizes and pore size distribution in the two regions. These differences were related to the temperature gradient present in the ash layer as a result of the heat transfer from the hot gases to the colder steam. The top layer, with a higher temperature, presents a higher degree of sintering and a larger fraction of molten ash. This was confirmed by the presence of additional silicon oxide concentration in the top layer when compared to the bottom layer. The additional silicon oxide is related to fly ash captured by collision to the softer, more sticking top layer. The presence of mullite would increase the insulating effect of the ash layer.

The complex phenomena of the growth of the ash deposit were analyzed under some simple growing rules, such as the ballistic and random deposition models. The structures which evolved using the model of Kamarkar *et al* (2005), named Single Trajectory Particle Deposition Model, were compared to the porous structure of the ash deposit. The model predicted a higher porosity and also a higher value for the fractal dimension. Then an implementation of a probability function for the direction of the particle trajectories led to the Random Trajectory Particle Deposition Model which resulted in a better prediction of the measured porosities. The modification also allowed the model to be independent of the particle size. The implementation of additional probability functions for particle sizes and velocities in three-dimensional space led to the Three-Dimensional Model. The model resulted in low porosity due to the sticking treatment used, besides requiring additional computational effort. In order to improve the predictions of the Three-Dimensional Model a more detailed treatment of the sticking and rearrangement of the particles after collision are necessary.

In the next chapter, the generated structure of the ash layer is used to estimate the additional thermal resistance insulating the tubes in the steam superheating tube bank.

CHAPTER 4 - HEAT TRANSFER ANALYSIS OF THE ASH DEPOSIT

4.1 Introduction.

Ash deposition on the tubes of superheaters seriously inhibits heat transfer to the steam and consequently reduces the efficiency of boilers. As described in Chapter 1, the ash deposits may reduce the boiler thermal efficiency by 10%, Lee and Lockwood (1999).This is exceedingly high when small increases in efficiency are sought to satisfy the ever restricting environmental regulations. The boiler, unity 6 from the Jorge Lacerda thermo power plant, whose superheater tube is considered in this work, is represented in Fig. 4.1. The final superheater tube bundle, identified with letter A in Fig. 4.1, is shown in Fig. 4.2.

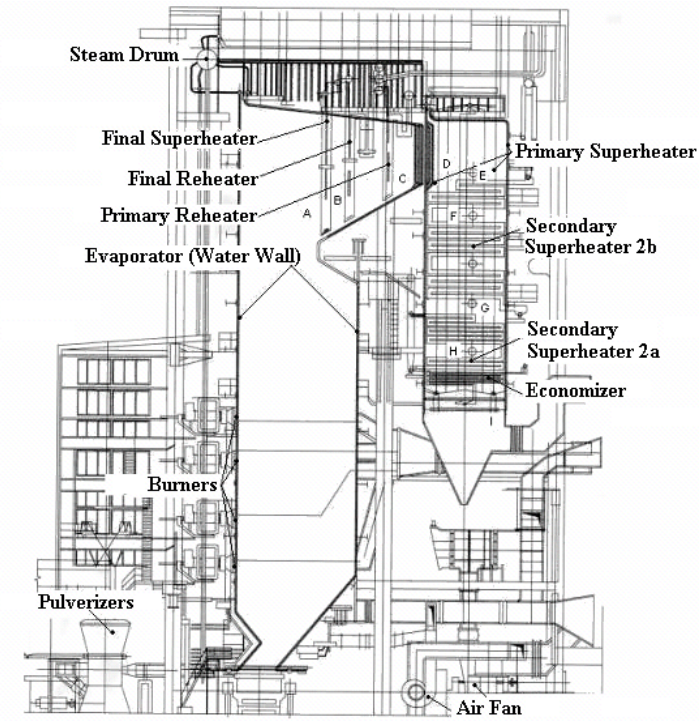

Figure 4.1 – Pulverized coal boiler, unity 6 from the Jorge Lacerda Thermo Power Plant, 135MWth, adapted from Reinaldo (2004).

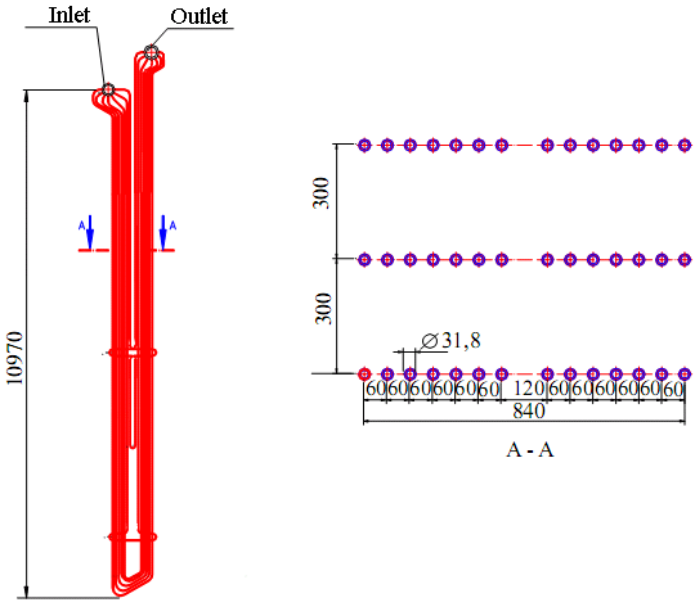

Figure 4.2 – Superheater of the steam generator, the dimensions are in mm, adapted from Reinaldo (2004).

As in Chapter 2, only a single tube will be analyzed, reducing the problem to the heat transfer by forced convection and radiation from the hot flue gas to a circular tube with a composite wall and an internal steam flow.

Here, the heat transfer from the flue gases to the steam will be predicted through a one dimensional analysis using the results from the 2D deposition models to provide the structural properties of the ash deposit. This one dimensional simplification may have an impact on the prediction of the heat transfer rate because the ash deposit is not expected to be homogeneous around the circular cylinder. Instead, it has a higher growing rate in the stagnation zone than in the region where boundary layer separation occurs. Nevertheless, the 2D results will be used in a model that estimates the effective thermal conductivity of the ash deposit, with and without low Knudsen number (rarefaction) effects. The effect of using a one dimensional model will be estimated from a parametric analysis.

The results of Reinaldo (2004) and Silva (2008) will be used here as input data for the boundary conditions in heat transfer.

4.2 Analysis of the Heat Transfer Rate from Flue Gases to Steam

In the superheater tube bundle, heat is transferred from the hot flue gases to the cold steam flow inside the cylinder by convection and radiation from the external side; by conduction through the tube wall; and, finally, by convection from the tube wall to the steam flow. Figure 4.3 shows a rendering of the heat transfer from the flue gas to the steam. The ash deposit is located between the flue gas and the wall tube and acts as a resistance in the heat transfer due to its porous structure and low heat conductivity.

According to Baxter (1998) and Zhogar *et al* (2005), the physical properties of a deposit, which are the most important factors controlling heat transfer, are the effective thermal conductivity, k_{eff}, and the surface emissivity, ε_d, since these properties depend on the deposit structure.

As described in Chapter 3, the ash deposit consists of several layers with different compositions, porosities and microstructures. All these characteristics lead to different thermal conductivities and consequently different thermal resistances. Different ash deposit positions around the tube or among tubes in the tube bundle can have different impact on the heat transfer.

In this work, the ash deposit will be considered as a uniform layer around the tube with an effective thermal conductivity obtained from the structures generated in Chapter 3.

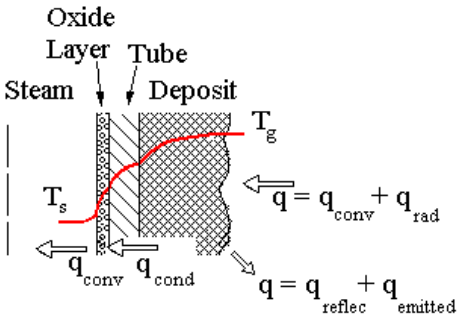

Figure 4.3 – Schematic composite wall and heat transfer mechanisms.

The radiation that comes from the burners has a significant effect on the temperature of the tubes Silva (2008). In addition, the deposit surface emits and reflects the radiation due to the incident flux from the furnace and the high temperature on the deposit surface. The net flux from the outer region is conducted through the composite wall formed by the ash deposit, the tube wall and the oxide layer. The latter is

formed due to the deposition of impurities present in the steam, thermal degradation of the tube and some surface reactions from the steam with the iron in the steel. Finally, the heat flux in the inner radius of the oxide layer is convected to the steam flowing inside the tube. Equation 4.1 computes the net flux from the outer region.

$$q_{cond} = q_{ec} + q_{irad} - q_{rerad} - q_{erad} \tag{4.1}$$

where, q_{cond} is the heat flux conducted through the composite wall, q_{ec} is the forced convection heat flux from the flue gases, q_{irad} is the incident radiation flux from the hot gases and from the furnace, q_{rerad} is the reflected radiation flux from the ash deposit surface and q_{erad} is the emitted radiation flux from the ash deposit surface. Each of these heat fluxes will be estimated separately.

4.2.1 External Convection to the Tubes in a Cross Flow

An estimate of the external convection heat transfer coefficient may be obtained from Zhukauskas (1961) correlation, presented in Incropera and DeWitt (1996) as,

$$\overline{Nu}_D = C\,Re_D^m\,Pr^n \left(\frac{Pr}{Pr_d}\right)^{1/4} \tag{4.2}$$

where C = 0.683 and m = 0.466 are constants for the Reynolds Number range of 40 to 4.000, based on the external diameter. As Pr < 10, n = 0.37. All properties are evaluated at T_∞ except Pr_d which is evaluated at T_d. This correlation is also used in the estimates done by Zhogar *et al* (2005) and Bazzo (1995).

4.2.2 Internal Convection inside the Tube

A rough estimate of the heat transfer coefficient for internal flow in the fully turbulent flow regime can be obtained, as listed in Incropera and DeWitt (1996), from

$$\overline{Nu}_D = 0.027\,Re_D^{4/5}\,Pr^{1/3}\left(\frac{\mu}{\mu_s}\right) \tag{4.3}$$

This correlation is valid for $Re_D \geq 10{,}000$ and $0.7 \leq Pr \leq 16{,}700$. All properties are evaluated at the mean (or bulk) temperature, except μ_s which is evaluated at surface temperature. This correlation is also used in the estimates done by Zhogar *et al* (2005) and Bazzo (1995).

4.2.3 Incident Radiation Heat Flux from Furnace

Reinaldo (2004) simulated the flow and heat transfer around the superheat bank for the same boiler operating with coal under the same conditions used here. The irradiation flux was calculated from the flame and furnace walls to a plane parallel to the axis of the superheater tubes. In order to calculate the heat exchange between this plane and the furnace walls and flame, the model of Lockwood and Shah (1981), *apud* Reinaldo (2004), was used. Here, the heat transfer from this plane to a single tube is estimated, as depicted in Fig. 4.4.

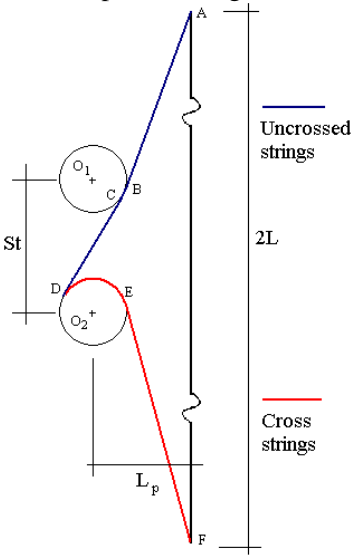

Figure 4.4 – Illustration of the inlet plane parallel to the axis of the superheater tube.

The radiating plane presents a radiation intensity distribution, as shown by Reinaldo (2004). Here, only an average value is taken as representative of the whole inlet plane. Then, from the radiation view factor, the radiative energy leaving the inlet plane and reaching the tube is given by

$$q_{irad} = F_{pt} \frac{A_p}{A_t} q_{iplane} \tag{4.4}$$

where F_{pt} is the radiation view factor from the inlet plane to the tube, A_t is the area in the tube that intercepts the radiation from the inlet plane, A_p is the area of the inlet plane and q_{iplane} is the average irradiation from the inlet plane.

The crossed string method of Hottel (1954), *apud* Siegel (2001) is used to calculate the view factor, and can be expressed as

$$F_{pt} = \frac{L_{cross} - L_{uncrossed}}{2A_p} \tag{4.5}$$

where L_{cross} is the sum of the length of the cross strings, Eq. 4.6, and $L_{uncrossed}$ is the sum of the lengths of the uncrossed strings, Eq. 4.7, both represented in Fig. 4.2.

$$L_{cross} = \overset{\frown}{DE} + \overline{EF} \tag{4.6}$$

$$L_{uncrossed} = \overline{AB} + \overset{\frown}{BC} + \overline{CD} \tag{4.7}$$

4.2.4 Incident Radiation Heat Flux from the Hot Gases

The hot gases emission is simplified to the same approach developed by Hottel (1954), *apud* Incropera and DeWitt (1996) and Siegel (2001), and is expressed as

$$E_g = \varepsilon_g \sigma T_g^4 \tag{4.8}$$

where the gas emissivity, ε_g is determined by correlating the gas temperature, the partial pressure of the radiating species and the mean beam length of the gas layer, and σ is the Stefan-Boltzmann constant. The total gas emissivity can be expressed as

$$\varepsilon_g = \varepsilon_w + \varepsilon_c - \Delta\varepsilon \tag{4.9}$$

where ε_w is the emissivity of water vapor, ε_c is the emissivity of carbon dioxide in a mixture and $\Delta\varepsilon$ is the correction factor due to the mutual absorption radiation between the two species. The emissivities were taken from the emissivity chart presented by Incropera and DeWitt (1996) as a function of the mean beam length and the partial pressure of the CO_2 and H_2O.

4.2.5 Ash Deposit Radiation Emission

According to Wall *et al* (1979), *apud* Zbogar *at al* (2005) an ash deposit thicker than 1 mm can be considered an opaque medium and the spectral emissivity is related to the spectral reflectivity by

$$\varepsilon_\lambda = \alpha_\lambda = 1 - \rho_\lambda \tag{4.10}$$

In general, the ash deposit cannot be considered gray. Wall and Becker (1984) stated that ash deposits behave as a dielectric material with a region of low emissivity at short wavelengths followed by a region of high emissivity at longer wavelengths. The effect of this spectral distribution on total emissivity or total absorptivity is to cause ε

or α to decrease as temperature increases. The reason for this is that while the emission (or absorption) bands of such materials remain relatively fixed in relation to spectral position, as temperature increases, the region of maximum energy of Planck's function moves toward shorter wavelengths. This causes ε or α to be weighted towards the low (short wavelengths) spectral emissivities, at high source temperature or surface temperature, respectively. Figure 4.5a shows the spectral emissivity and Fig. 4.5b shows the total absorptivity and total emissivity

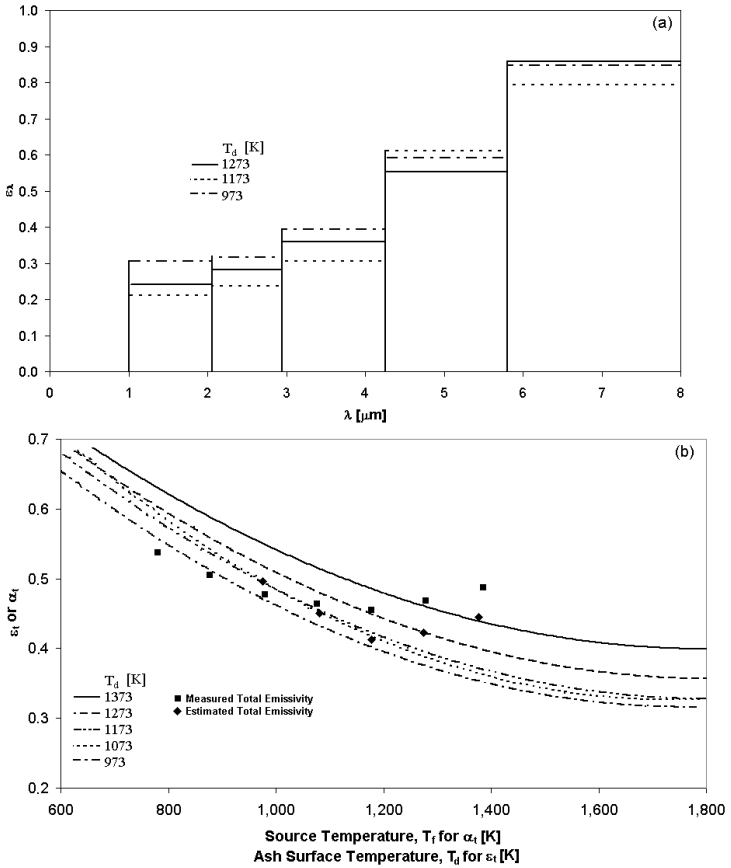

Figure 4.5 – (a) Band emissivity measurements, (b) Estimated total absorptivity (lines), estimated total emissivity (full diamond) and measured total emissivity (full square), adapted from Wall and Becker (1984)

It should be noted in Fig 4.5b that the abscissa is the ash surface temperature for the total emissivity values, whereas the abscissa for the total absorptivity is the source temperature.

Wall and Becker (1984) measured the spectral emissivity for several coal ashes and Fig 4.5 shows only the sample that has similar composition to the ash deposit used in this work (high content of SiO_2 and Al_2O_3). Figure 4.5 illustrates the influence of the spectral emissivity distribution over the total emissivity and total absorptivity, except when the source temperature equals the ash deposit surface temperature, the total absorptivity will have a different value from the total emissivity. The hypothesis of a grey surface does not fit the ash deposit. Figure 4.5b is used in this work in order to estimate the total absorptivity and the total emissivity of the ash deposit. Zbogar *et al* (2005) used the value of 0.9 for the total emissivity when the temperature of the ash deposit is above fusion temperature, otherwise data of Boow and Gorad (1969) *apud* Zbogar *et al* (2005) was used.

4.2.6 Thermal Conduction in the Composite Wall

For steady-state, one-dimensional, constant property heat transfer by conduction across a circular shell made of a homogeneous material the temperature distribution is

$$T(r) = T_1 - q\frac{r_2}{k_{eff}}\ln\left(\frac{r}{r_1}\right) \tag{4.11}$$

where q is the radial heat flux and k_{eff} is the effective thermal conductivity of the homogeneous medium.

There are several approaches in which the effective thermal conductivity can be evaluated. Most of them were compared in the work of Zbogar *et al* (2005) and some specifically to the case of the steam generator were used by Reinaldo's (2004). Usually these approaches correlate the effective thermal conductivity to porosity, ϕ, and tortuosity, τ as

$$k_{eff} = \frac{k_s(1-\phi)}{\tau} \tag{4.12}$$

where k_s is the thermal conductivity of the solid phase, assumed much larger than the thermal conductivity of the gas phase. The tortuosity represents the ratio of the temperature gradient normal for the surface of the ash deposit by the apparent temperature gradient along the radial coordinate along the deposit. Thus, as the solid phase becomes less connected, the tortuosity increases. Tortuosity can be correlated to the

degree of sintering of the ash deposit. From the reconstruction of the ash layer presented in Chapter 3, an estimate of the tortuosity can be made as shown below.

4.3 Modeling of the Effective Thermal Conductivity of the Ash Deposit

There are several approaches to evaluate the thermal conductivity of a porous medium, and some of them were evaluated in detail in the work of Rezaei *et al* (2000), Reinaldo (2004) and Zbogar *et al* (2005).

In order to evaluate the ash deposit thermal conductivity, the model used to generate the porous structure in Chapter 3 will be used together with a finite difference method to solve the conduction on the ash deposit generated. An example of the structure generated from the model is shown in Fig. 4.6.

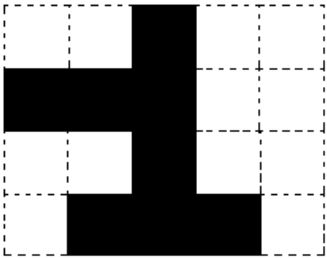

Figure 4.6 – Porous structure generated from ash deposition model.

The solid phase is represented by the filled squares, while the empty ones represent the pore filled with fluid (flue gas). In order to take advantage of the structure generated, the finite volume method can be applied to all squares as control volumes of the mesh with uniform grid spacing of δ = 1.3 μm, which is equivalent to the pixel relation obtained from the SEM resolution in Chapter 3.

In order to apply Fourier's Law, the continuum hypothesis must be assumed. For the continuum approach to be valid, the size of the flow system must be larger than the mean free path of the molecules. The mean free path is the average distance traveled by a molecule between two consecutive collisions and, according to Turns (2000), can be calculated by:

$$\lambda = \frac{1}{\sqrt{2}\pi d^2 n_v} \tag{4.13}$$

where λ is the mean free path, d is the mean molecular diameter and n_v is the number of molecules per unit volume. Considering the flue gas as an ideal gas, the mean free path can be calculated as:

$$\lambda = \frac{\bar{R}T}{\sqrt{2}\pi d^2 N_A p} \tag{4.14}$$

where N_A is the Avogadro constant, p is the pressure, T temperature and $\bar{R}$ is the universal gas constant. In order to evaluate the mean free path, the flue gas is approximated by air with d = 3.71 Å, Turns (2000). For 1 atm and 1300 K, the mean free path is $\lambda \approx 0.3$ μm, which is close to the size of the grid spacing. The ratio between the mean free path and the characteristic length, L, is the Knudsen number:

$$\mathrm{Kn} = \frac{\lambda}{L} \tag{4.15}$$

For a very small Knudsen number, $\mathrm{Kn} \ll 1$, the continuum hypothesis can be used without modifications, while for $\mathrm{Kn} \gg 1$ the gas rarefaction cannot be neglected. In order to solve the rarefied regime, the Boltzmann kinetic equation must be applied, and the solution requires much computational effort. However, for a moderately small Knudsen number, i.e. when $\mathrm{Kn} \approx 1$, the Fourier equation can still be applied and the gas rarefaction taken into account via the temperature jump boundary condition. This is a correction applied to the boundary condition for the Fourier equation that takes into account the temperature slip at the walls as a result of molecular motion. Following Sharipov and Kalempa (2005), the temperature slip is given as

$$T_g = T_w + \zeta_T \frac{\mu}{p}\left(\frac{2\kappa_B T_w}{M}\right)^{1/2} \left.\frac{\partial T_g}{\partial x}\right|_{x=0} \tag{4.16}$$

where x is the coordinate normal to the surface directed towards the gas with origin on the surface, μ is the viscosity of the gas, p is the local pressure, M is the molecular mass of the gas, κ_B is the Boltzmann constant. The ζ_T is the temperature jump coefficient which must be calculated applying the Boltzmann equation to the Knudsen layer.

Sharipov and Kalempa (2005) calculated the temperature jump coefficient for a mixture of gases and showed that ζ_T varies with the concentration of the mixture, but for an accuracy of 5% the value of 1.954 can be used without loss of information, Sharipov (2007). An example of the influence of the modified boundary condition is shown in Appendix A4. This modified boundary condition is applied in all interfaces between gas and solid.

Here it has assumed a steady state and no heat source, which simplifies the energy conservation equation to

$$\nabla.(k\nabla T) = 0 \qquad (4.17)$$

The equation is applied to a 2-Dimensional geometry in Cartesian coordinates, with a prescribed temperature on the tube wall (y = 0) and a prescribed heat flux at the hot gas side ($y = L_y$), with periodic boundary conditions in all other directions (x = 0, $x = L_x$).

The conservation equation is discretized in finite differences. This is equivalent to setting up an electrical circuit analog for the reconstructed ash deposit, considering one thermal resistance for each interface between adjacent pixels. The harmonic mean is used to calculate the thermal conductivity at the interface between two adjacent cells, as recommended by Patankar (1980).

The code TEACH C from Gosman, *et al* (1985), which provides a finite difference solving procedure for the Laplace equation, is used. This is a well known and tested computer code written in Fortran language and here translated to Pascal in order to couple with the code developed in Chapter 3.

The numerical model is applied to each one of the 600 independent simulations presented in Chapter 3 for the Random Trajectory Particle Deposition Model. At the prescribed temperature of 800 K and heat flux 5 10^4 W/m^2 from hot gases, it considers the rarefaction effect inside the porous structure and 0.05 W/m/K for the continuous phase.

A typical result obtained for a porosity of ϕ = 0.41 has an effective thermal conductivity 0.36 W/m/K. The inclusion of the temperature jump boundary condition leads to a lower thermal conductivity, 0.32 W/m/K

Two simple models can be used as theoretical boundaries. Assuming that the gas and the solid phase conduct heat independently these boundaries can be formulated as (1) Upper value, where heat is transferred in a direction parallel to the layers, as shown in Fig. 4.7. The heat resistance is calculated as a parallel connection of thermal resistances. (2) Lower value, in which heat is transferred in a direction normal to the layers as shown in Fig. 4.7. The heat transfer resistance is calculated as a serial connection of thermal resistances. The model can also be compared to another simple approach, namely the Rayleigh model which consists of a cubic array of uniform, unsintered, spheres (discrete phase) embedded in a continuous phase.

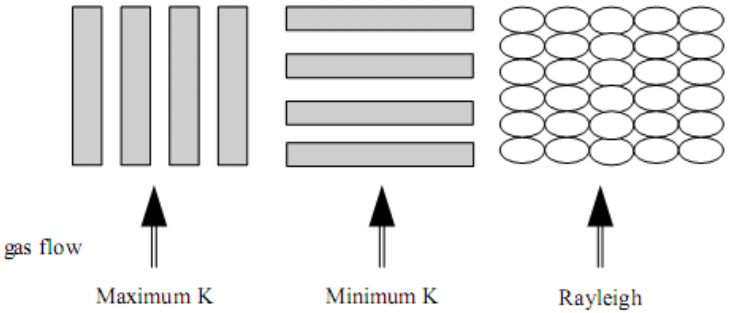

Figure 4.7 – Models for thermal conductivity estimations, adapted from Zbogar *et al* (2005).

For the case above the $k_{eff\ min}$, $k_{eff\ max}$ and the Rayleigh model considering the deposit as a slag, $k_{eff\ RS}$ and for the deposit as a particulate cluster, $k_{eff\ RP}$ the effective thermal conductivity resulted in 0.12, 1.22, 0.65 and 0.14 respectively. As demonstrated, the results of 0.36 and 0.32 are in the range of maximum and minimum, and if compared to the Rayleigh model the actual approach is in the transition from the slag to a particulate type.

It must also be noted that the prediction of thermal conductivity for a 2D medium is usually smaller than the predictions for a corresponding 3D extension of the model. Wang *et al*. (2007) observed an increase of 30% for a two-phase medium with k_s = 0.60 W/m/K, k_g = 0.035 W/m/K and ϕ = 0.3 when a third dimension is added to a reconstructed random 2D model.

Using the value 0.36 W/m/K in the thermal conductivity relation given by Eq. 4.12, would return a tortuosity factor of τ = 3. It can be remembered that the tortuosity factor for thermal conductivity defined by Eq. 4.12 is a function of the porosity, particle size and the probabilities used to generate the deposit, as the trajectory angle probability.

In order to obtain a correlation for the tortuosity factor, a curve fitting is suggested using the equation

$$k_{eff} = A k_s^B (1-\phi)^C \tag{4.18}$$

where A, B and C are constants to be fitted.

Several deposits were generated choosing particles with size 2 from 5% to 95% with 10º and 20º of standard deviation in the particle trajectory and 50 realizations for each probability, for substrate length of 32 and 64. These deposits resulted in porosities ranging from ϕ = 0.19 to

0.44. Finally, the solid thermal conductivity was varied from 2 to 8 W/m/K.

Figure 4.8 presents the calculated effective thermal conductivity as a function of porosity for the three solid conductivities. The continuous lines are the results of the best curve fits. Via multiple regression, the best fitting curve using the least square method provided (restricted to $0.19 \leq \phi \leq 0.44$, $2 \leq k_s \leq 8$),

$$k_{eff} = k_s^{0.85}(1-\phi)^{3.25} \tag{4.19}$$

The curve fitting is best for k_s = 2 W/m/K, with a 2% deviation, and deviates more as k_s increases, reaching a 15 % deviation for k_s = 8 W/m/K.

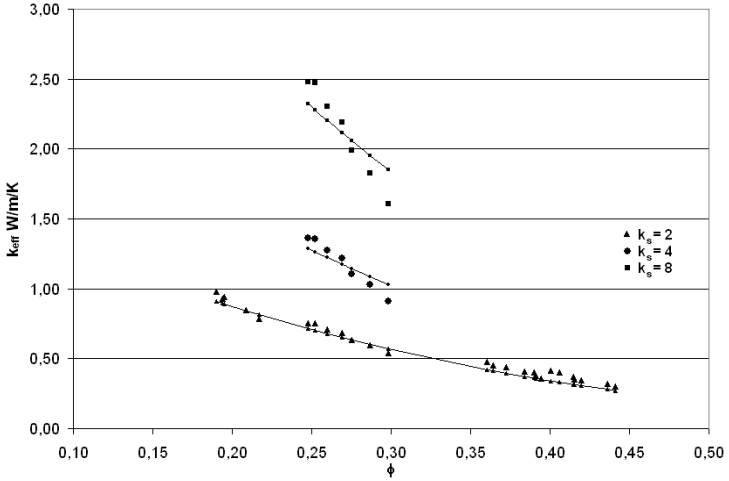

Figure 4.8 – The dependency of the thermal conductivity, k_{eff}, on the porosity, ϕ as calculated by the thermal conductivity model. The continuous lines are the best fit lines using equation 4.19.

The curves may be collapsed into a single one using a proper definition for the axis, as shown in Figure 4.9.

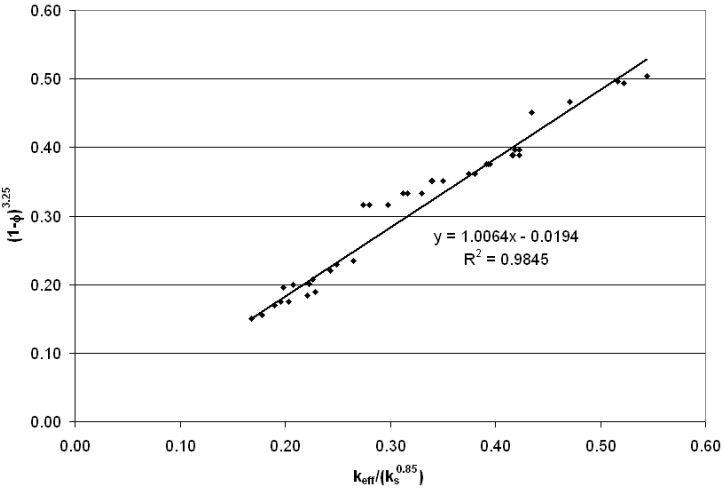

Figure 4.9 – Relation between ϕ and k_s in Eq. 4.19.

In this way, a maximum deviation of 15% for the thermal conductivity of 8 W/m/K was obtained, resulting in a reasonably good model. Comparing the curve fitted function to the model presented in Eq. 4.12, Eq. 4.19 may be rewritten as

$$\frac{k_{eff}}{k_S} = \frac{(1-\phi)}{\tau} \tag{4.20}$$

where the tortuosity factor is expressed as

$$\tau = \frac{k_S^{0.15}}{(1-\phi)^{2.25}} \tag{4.21}$$

In which $k_g > 0$, the tortuosity is not only a topological property, since it depends on how much heat is conducted along the solid phase when compared to the heat conducted along the gas phase. The dependency on the solid conductivity is expressed by the 0.15 exponent, which is weak. The dependency on the porosity expresses the change in topology as different rules are applied to grow the medium, generating different porosities. The function, however, does not satisfy the limit for $\phi = 0$.

Rezaei *et al* (2000) determined the thermal conductivity for a range of coal ash and synthetic ash samples. The ash pellets were placed on the base plate of a reference material with a known thermal conductivity. Both sides of the test and reference materials are polished nickel plates connected to thermocouples. The sample and the references

materials are isolated to minimize the radial heat losses. A constant weight pressure is also applied to reduce the contact resistance between the ash and the base.

Among those materials and ash samples analyzed by Rezaei *et al* (2005) ash sample A is the one whose chemical composition is similar to the typical ash from Jorge Lacerda. For a porosity of 29% the thermal conductivity resulted in 0.58 W/m/K and if compared to the Eq. 4.19 the effective thermal conductivity is 0.59 W/m/K resulting in 2% of deviation. If compared to the same sample A, but with 58% of porosity the experiments resulted in 0.52 W/m/K and the proposed relation resulted in 0.11 W/m/K. The Eq. 4.19 was used out of the validity range.

This model will be used to estimate the effect of the ash deposit on the ash surface temperature and boiler efficiency.

4.4 Parametric Analysis of the Effects of the Ash Deposit on the Ash Surface Temperature Distribution and Boiler Energy Balance

In this section the one-dimensional approach delineated above will be used to estimate the temperature distribution along the ash deposit.

In this analysis the average temperature of the steam is taken from an energy balance in the boiler, as shown by Reinaldo (2004). The average heat flux is taken from the difference between the inlet and outlet steam enthalpy flow divided by the internal surface area of the tube. Concerning the oxide layer, Bernardini *et al* (1999) measured the oxide layer inside the tube of the superheater and obtained the thickness of 0.15 mm with a thermal conductivity of 0.59 W/m/K, which is assumed here. For the solid phase of the ash deposit, the thermal conductivity was assumed to be the sum weighted average of the oxides present in the ash deposit, resulting in k_s = 2 W/m/K as calculated by Reinaldo (2004). The same approach is used by Zbogar *et al* (2005) and Baxter (1998).

The tube wall has an external diameter of 31.8 mm and a width of 5.6 mm with an average thermal conductivity taken as 30 W/m/K. The steam inlet temperature on the tube in the middle of the superheater tube bundle is 700 K. For the same tube, the outlet temperature is close to 800 K. The temperature in the middle of the tube is taken as 730 K. The steam mass flow is 0.39 kg/s, as calculated by Reinaldo (2004). From an estimated heat flux of 6 kW/m^2 the temperature on the outer radius of the tube is 780 K. Irradiation from the furnace was assumed to be 130 kW/m^2, as calculated by Reinaldo (2004). To simulate the boiler superheater, Reinaldo (2004) considered the radiation exchange among

the tubes of the tube bundle and the tubes with the water wall near the superheater, along with the entire furnace. So the difference between the inlet and outlet steam temperature is due to the radiation from the furnace, net radiation and convection between the tubes and the flue gas and the radiation between the tubes and water wall. The last term, is not considered directly here, but is obtained, indirectly, as a first assumption, from the subtraction of the net radiation (furnace and hot gases) absorbed by the ash deposit and the flue gas convection heat flux from the difference of the inlet and outlet enthalpy of the steam.

Figure 4.10 presents the temperature distribution along an ash layer 5 mm thick using Eq. 4.12 for two values of tortuosity and a porosity of 0.3 and the proposed correlation, Eq. 4.19. The temperature profile for a fully solid ash layer is also shown ($\tau = 1$, $\phi = 0$).

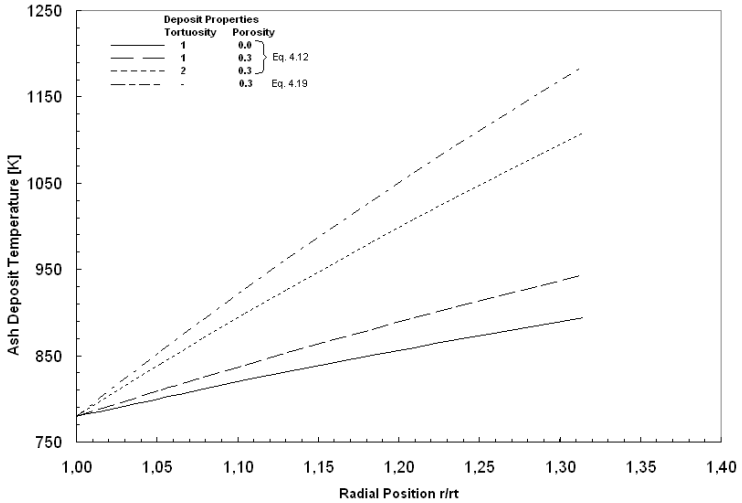

Figure 4.10 – Effect of tortuosity on the radial temperature distribution along the ash deposit.

In order to evaluate the influence of the ash deposit properties on temperature distribution, Fig. 4.10 also considers a case under the same conditions described before, but with a completely fused ash deposit, a slag deposit without pore.

According to Eq. 4.11, once the tortuosity doubles, the temperature difference $T(r)-T_1$ at a given radius r doubles. Any increase in effective thermal conductivity must be also followed by an increase in flue gas temperature in order to keep the same heat transfer rate to the

steam. This increase also leads to an increase in the ash surface temperature, provoking additional melting, capture and sintering. This situation may ultimately lead to a complete blockage of the channels between adjacent tubes. Although Eq. 4.11 has a logarithm behavior, Fig. 4.10 does not show this tendency especially because the thickness of the ash deposit considered in this analysis is small, 5 mm.

Comparing the temperature distribution of both Eq. 4.12 and 4.19 for the same porosity, 0.30, it is clear that the proposed correlation increases the complexity of the analysis. In order to have the same effective thermal conductivity, the tortuosity on Eq. 4.12 should be around 2.45. Also from Fig. 4.10, the temperature on top of the deposit is close to 1200 K, which is near the melting temperature for the typical ash analyzed here. It does indicating that the ash deposit height should be close to 5-8 mm and this result can be qualitatively compared to the ash deposit at the bottom of the Fig. 3.1.

To analyze the influence of the ash deposit on the temperature needed for the flue gas in order to keep the same superheating, a tube under the same conditions described before, but without the ash deposit will be considered as the base case. The enthalpy of the average temperature from the upstream and downstream flue gas will be considered as the reference for enthalpy rise. Figure 4.11 shows the influence of the porosity on the enthalpy rising need compared to the base case, using the simple equation Eq. 4.12, Fig. 4.11a, and the proposed correlation Eq. 4.19, Fig. 4.11b.

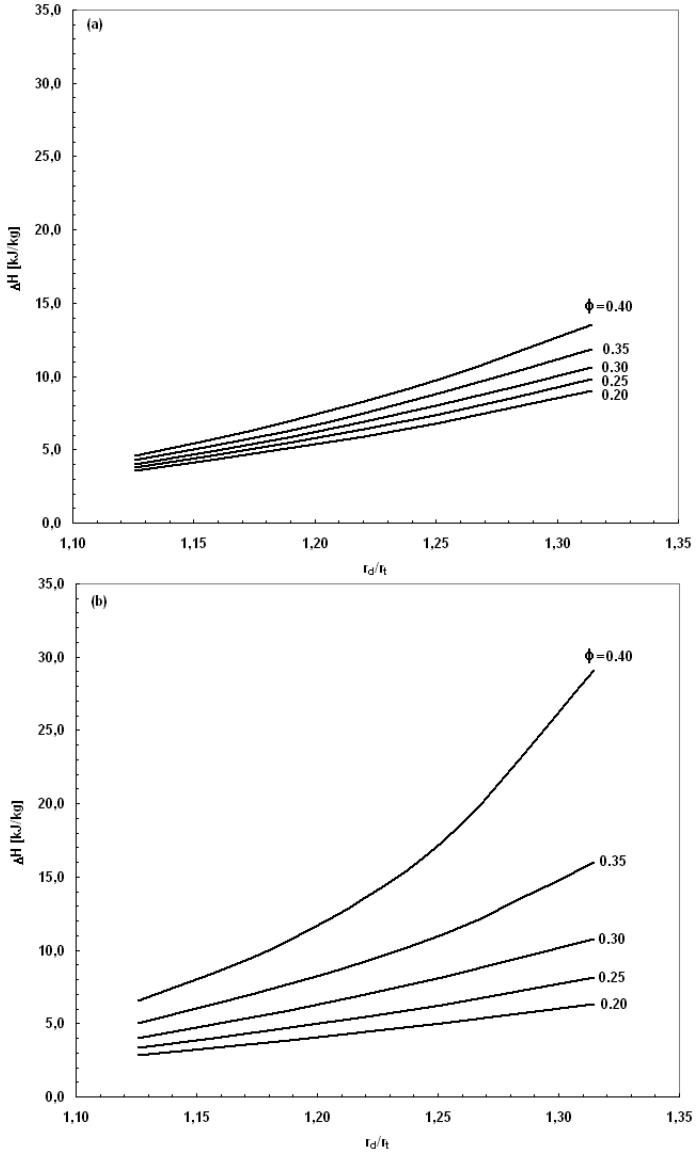

Figure 4.11 – Effect of the porosity on the rising of enthalpy compared with a bare tube (a) using the simple relation Eq. 4.12 and (b) the proposed correlation Eq. 4.19.

As shown in Fig. 4.11 the effect of porosity is more pronounced via the proposed correlation than in the simple Eq. 4.12. That happens because Eq. 4.19 takes into account the non linearity imposed by the complex porous structure generated by the model proposed in Chapter 3, Random Trajectory Particle Deposition Model, while the Eq. 4.12 conserves the linearity influence as the deposits grows.

For a deposit with porosity = 0.3 and 5 mm wide, the flue gases must have an additional energy of 30 kW per superheater tube in order to supply the same energy to the steam flow and therefore keep the same output power. The boiler efficiency might decrease by 3% from the nominal value if this situation is applied to the entire tube bank, which contains 40 lines with 7 tubes each. This value is consistent with the 10% decrease presented by Lee and Lockwood (1999), since they considered the influence of the ash deposit over the whole boiler.

The non linearity is more pronounced for a deposit with porosity over 0.35 and especially for deposits with $r_d/r_t > 1.25$, which require more energy from the flue gases, Fig. 4.11. But this situation may not be true, especially if the ash deposit surface reaches the melting ash temperature, which is close to 1200 K. In order to evaluate the influence of the porosity on the ash deposit surface temperature, the effect of the resistance imposed by the particles deposited will be considered using a Biot number, defined as:

$$\mathrm{Bi} = \frac{R_{cond}}{R_{ec}} = \frac{h_{eq} r_2}{k_{eff}} \tag{4.22}$$

where r_2 is the external tube radius and h_{eq} is the equivalent convection coefficient which is the result of the summation of convection and radiation heat flux linearized as,

$$q_{total} = q_{conv} + q_{rad} = h_{eq}\left(T_g - T_d\right) \tag{4.23}$$

Therefore, a larger value of porosity leads to a higher Biot number. Figure 4.12 presents the ash deposit surface temperature rise and the 1/Bi for different values of r_d/r_t.

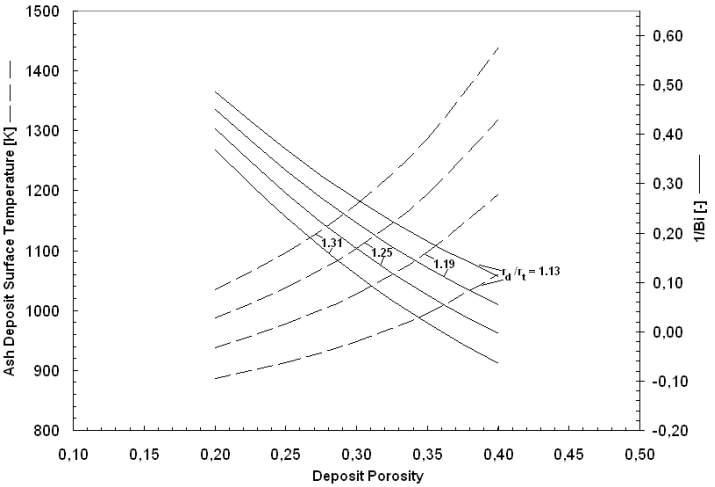

Figure 4.12 – Rise of the ash deposit surface temperature (——) and 1/Bi (–) as a function of porosity for different r_d/r_t.

From Fig. 4.12 it can be seen that for a higher porosity, for instance 0.40, there is a higher ash deposit surface temperature. However, for temperatures close to 1200 K, the ash might reach the melting temperature indicating that deposits with porosity of 0.40 and width of 4 mm (r_d/r_t = 1.25) probably have a different structure from the one proposed by the present model developed in Chapter 3. This happens because of the melting and high efficiency of the ash surface in capturing the fly ash particles in the flow. It can also be seen that for this situation the 1/Bi number is lower than 0.1. This would indicate that the ash surface temperature is close to the gas temperature while the negative values are due to the rise of the surface temperature above that of the flue gases, which is not realistic.

Figure 4.12 indicates that there is a limit to the use of the correlation proposed. This limit is not imposed by the porosity, which was evaluated at the limit range, see Eq. 4.19, but by the heat transfer process. This process changes the structure of the deposit as it grows indicating that the ash deposit model should take into account the boundary conditions to which the flow is subjected. When this is done, a restructuring process can be applied because of the heat transfer from the flue gases in which the heat transfer from the flue gases is embedded.

4.5 Conclusions

The ash deposit works as an insulating material for the heat transfer from the hot flue gases to steam, causing a decrease in the boiler efficiency.

In this chapter, the effect of the ash deposit on the ash surface temperature and boiler efficiency was evaluated. The model assumed a one-dimensional heat transfer from the flue gases to steam. The external heat transfer included radiation from the boiler walls, radiation and forced convection from the flue gases. The internal heat transfer considered the forced convection into the flowing steam. The conduction heat transfer considered the oxide layer, the steel tube and the ash deposit. Based on the evolution of the structures in Chapter 3, an effective thermal conductivity model was developed and applied to the structures of the ash deposit. The calculated values of thermal conductivity were curve fitted to porosity and solid thermal conductivity which resulted in a 15% maximum deviation of the curve fitted function when compared to the calculated values. The curve fitted function for the effective thermal conductivity was then used to calculate an average representative value of effective thermal conductivity of a typical ash deposit. The one dimensional model was then applied and the effects of the ash deposit were estimated.

For a typical boiler operating condition, the ash deposit reduces the boiler efficiency in at least 3%, when compared to a base operating condition in the absence of ash deposition. This decrease was calculated keeping the same boiler power in a presence of a 5 mm ash deposit. In times when small increases in thermal efficiency are sought, these figures are exceedingly high.

Although the proposed correlation leads to good results when compared to Rezaei *et al* (2000), it must be used with caution in order to have realistic ash deposit surface temperatures, as indicated by the 1/Bi analysis. This result also showed a need to improve the model in order to have a restructuring process that takes into account the heat transfer effects inherent to the flow of the flue gases.

CHAPTER 5 - FINAL REMARKS

5.1 Conclusions

This work discussed the mechanisms involved in ash particle deposition such as the vortex shedding on the tube of a superheater tube bundle, and applied particle deposition modeling via Lagrangean approach. The growing behavior of a porous structure and the heat transfer mechanisms on the ash deposit were also discussed.

The objective of this work was to analyze and evaluate the ash particle in a tube of the superheater tube bundle. Developing an ash deposit growth behavior and the heat transfer models across the ash deposit were proposed here. The results were compared with a typical ash deposit collected from the boiler superheater tubes.

The ash particles deposition and the solution of the flow around a circular cylinder were found via the CFD technique, applying Large Eddy Simulation for turbulence closure, This technique is more suitable for solving the large scales of turbulence which have a greater influence on the deposition of ash particles.

In order to apply the LES approach to ash deposition, a previous test case was considered to select the appropriated grid for a lower Re_D, typical of superheater tubes. Typical values of the flue gas flow in the region of superheater tubes were selected, and the ash particle size distribution was set as the same measured in the power plant.

As expected, ash particles with higher relaxation time showed a higher deposition rate due to their lower tendency to follow the streamlines around the circular cylinder. Also, these depositing particles showed a similar particle Reynolds number around the tube.

For the particles with lower relaxation time, the Re_p showed a raising tendency while following the cylinder curvature. This is due to the favorable pressure gradient which increases the fluid velocity, accelerating the depositing particles.

The ash deposit formation and growth was analyzed under some simple growth rules, such as the ballistic and the random deposition models. These simple models generated porous structures that were compared without success to a typical ash deposit collected from a steam generator. But a simple modification, i.e. the inclined trajectories, leads to a modified particle deposition model which represents the ash deposit better.

The physical and chemical characteristics of the ash deposit were measured. SEM pictures were provided and analyzed with the Imago software. The X-ray diffraction method, showed a transition region from the base, close to the heat exchange tube, to the top of deposit, which indicates a transition from a sintered to a more agglomerated region. This phenomenon is a consequence of the strong heat transfer to the steam flow and fast cooling of the first fly ash particles. This possibly leads to the precipitation of the mullite crystals which insulate the steam from the hot flue gas. The proposed procedure for ash characterization deposits in boilers was found to be reliable and suitable to support the results found on the ash deposition model proposed.

The heat transfer through the ash deposit is the most important mechanism in the insulation from the hot flue gases, and a rigorous analysis of the effective thermal conductivity must be considered. A classical approach considering a simple relation between porosity and tortuosity was considered in order to show the importance of the heat transfer analysis in the ash deposit. It is crucial for determining the rise in the flue gas energy required to overcome the penalties imposed by the ash deposit.

A new relation between porosity and effective thermal conductivity of the ash deposit was proposed here, and showed good results when compared to the finite difference method used on the porous structure and the experimental work of Rezaei *et al* (2005). Finally, this work proposes a model to evaluate the porous structure of a typical ash deposit in the superheater tubes along with a new relation between porosity and effective thermal conductivity of the ash deposit. Both models are based on different approaches from those in the literature presenting a new approach to evaluate the ash deposit influence on the boiler efficiency.

Another important result is that the flow field and particle deposition were evaluated based on the flow field data of a pulverized coal boiler. This methodology can provide enough data to evaluate the growth behavior of the ash deposit via the Three Dimensional Particle Deposition Model with further improvements, thus generating a model with all the information concerning the porous structure, pore size distribution and fractal dimension.

Based on the structure generated, a finite volume analysis can be done and the thermal properties of the ash deposit, such as the thermal effective conductivity, can be evaluated. This would provide a quite accurate correlation, for an engineering analysis concerned with the impact of the ash deposit on the thermal efficiency of the boiler of the

superheater. The proposed methodology and analysis can improve the design and optimization of boilers burning pulverized coal.

5.2 Recommendations for Future Works

The following improvements of the present treatment are recommended for future works:

1) Further analysis must be made and compared with the present data, due to the higher computational demand of the LES approach, a short period of time was considered in the calculation of the flow field and particle simulation around the circular cylinder;

2) In order to save CPU time, only a few particles were analyzed in the ash deposition and a wider range should be considered especially for the small particles;

3) Improvements in the ash deposition model considering the rearrangement of the deposited particles in order to represent better the influence of temperature inside the deposit should be taken;

4) Ash deposit samples should be taken from different positions in a more systematic way in order to provide a good representation of the ash deposition on the entire tube bundle;

5) Flow analysis in the pore should be taken in order to learn more about their effects on thermal insulation;

6) Improvements on the porous structure should be done in order to evaluate the tortuosity effects on the heat transfer.

BIBLIOGRAPHY

ANEEL, Brazilian Electricity Regulatory Agency, accessed October, 2008.

ARPACI, V.S., **Microscales of turbulence, heat and mass transfer correlation.** Amsterdam, Netherlands, Gordon and breach science Publishers, 1997.

ARMFIELD, S., STREET, R., **Modified fractional step methods for the Navier Stokes equations.** ANZIAM Journal, 45, C364 – C377, 2004.

BARABÁSI, A., STANLEY, H.E., **Fractal Concepts in Surface Growth**. Great Britain, Cambridge University Press, 1995.

BAXTER, L., **Ash deposition during biomass and coal combustion: a mechanistic approach**. Biomass and Bioenergy; 4, 85 – 102, 1993.

BAXTER, L., **Influence of ash deposit chemistry and structure on physical and transport properties.** Fuel Processing Technology, 56, 81 – 88, 1998.

BAZZO, E., **Geração de vapor.** Florianópolis, Publisher UFSC, Brazil, in Portuguese, 1995.

BERNARDINI, P.A.N., FURUKAWA, E., BUENO, E., **Identificação de causa de fratura em tubo do superaquecedor final da caldeira nº 5 da UTLB.** Technical Report, Tractebel Energy, Federal University of Santa Catarina, in Portuguese, 1999.

BERTI, L.F., *et al*., **A methodology for morphological and chemical characterization of ash deposits.** 19th International Congress of Mechanical Engineering, COBEM 2007, Brasília, Brazil, 2007.

BOURIS, D., BERGELES, G., **Numerical calculation of the effect of deposit formation on heat exchanger efficiency.** Int. J. Heat Mass Transfer, 40, 4073 – 4084, 1997.

BERGELES, G., *et al*, **Effects of fouling on the efficiency of heat exchangers in lignite utility boilers.** Applied Thermal Engineering, 17, 739 – 749, 1997.

BOURIS, D., PAPADAKIS, G., BERGELES, G., **Numerical evaluation of alternate tube configurations for particle deposition rate reduction in heat exchanger tube bundles.** Int. J. Heat Fluid Flow, 22, 525 – 536, 2001.

BREUER M., **Large eddy simulation of the subcritical flow past a circular cylinder: numerical and modelling aspects.** Int. J. Numer. Meth. Fluids, 28, 1281 – 1302, 1998.

BRYERS, R.W., **Fireside slagging fouling and high temperature corrosion of heat transfer surface due to impurities in steam raising fuels.** Prog. Energy Combustion, 22, 29 – 120, 1996.

CLASEN, L.F., **Structural, chemical and mineralogic characterization of ash deposit in boiler heat exchange operating with pulverized coal.** Mater Thesis, in Mechanical Engineering, Federal University of Santa Catarina, Florianópolis, Brazil, in Portuguese, 2007.

CROWE, C.T., TROUTT, T.R., CHUNG, J.N., **Numerical models for two phase turbulent flows.** Annu. Rev. Fluid. Mech. 28, 11 – 43, 1996.

DAMIANI, M.C., *et al*. **IMAGO: An image software analysis**; Proceedings of first congress in materials of South region SULMAT-2000, Joinville, Santa Catarina, Brazil, (in Portuguese) 751 – 759, 2000.

DOBRESCU, G., RUSU, M., **Dynamic scaling method and interface growth**. Advances in Colloid and Interface Science, 95, 83 – 93, 2002.

FALCONER, K.J., **Fractal geometry: mathematical foundations and applications.** J. Wiley Publisher, 1990.

FAN, J.R., ZHA, X.D., SUN, P., CEN, K.F., **Simulation of ash deposit in a pulverized coal fired boiler.** Fuel, 80, 645 – 654, 2001.

FERNANDES, C.P., **Morphological characterization of porous space: multiscale reconstitution and simulation of the process of fluid non-wetted intrusion.** Doctoral thesis in Mechanical Engineering, Federal University of Santa Catarina, Florianópolis, Brazil, in Portuguese, 1994.

FRANKE, J., FRANK, W., **Large eddy simulation of the flow past a circular cylinder at Re_D = 3900.** J. Wind Eng. Ind. Aerodynamics, 90, 1191 – 1206, 2002.

FRÖHLICH J., RODI W., KESSLER Ph., PARPAIS S., BERTOGLIO J.P., LAURENCE D., **Large eddy simulation of flow around circular cylinders on structured and unstructured grids**. In: Hirschek E., (ed) Numerical Flow Simulation I. Notes on numerical fluid mechanics, 66, 319 – 338, 1998.

FLUENT USER'S GUIDE. Version 6.3.26, Fluent Inc, 2007.

GASKELL, P.H., LAU, A.K.C., **Curvature compensated convective transport: Smart, a new boundedness preserving transport algorithm.** Int. J. for Num. Meth. Fluids, 8, 617 – 641, 1988.

GERMANO M., PIOMELLI U., MOIN P., CABOT W.H. **A dynamic subgrid scale eddy viscosity model**. Physics of Fluids A, 3, 1760 – 1765, 1991.

GHOSAL S., MOIN P. **The basic equations for the large eddy simulation of turbulent flows in complex geometry.** J. Comp. Phys., 118: 24 – 37, 1995.

GOSMAN, A.D., LAUNDER, B.E., REECE, G.J. **Computer Aided Engineering Heat Transfer and Fluid Flow. Ellis Horwood Limited,** 1985.

HAPPEL, J., BRENNER, H., **Low Reynolds Number Hydrodynamics.** Springer Publisher, 1983.

HANJALIĆ, K. **Turbulence and Transport Phenomena: Modelling and Simulation.** Class notes. Available at: <www.sla.tu-darmstadt.de/lehre/tms/TurbModeling-Hanjalic_0705.pdf>. Accessed in: May, 2008.

HUANG, L.Y., NORMAN, J.S., POURKASHANIAN, M., WILLIAMS, A., **Prediction of ash deposition on superheater tubes from pulverized coal combustion.** Fuel, 75, 271 – 279, 1996.

INCROPERA, F.P., DEWITT, D.P., **Fundamentals of heat and mass transfer.** New York, John Wiley & Sons Press, 1996.

IEA – International Energy Agency. **Key world energy statistics.** 2008.

IEA – International Energy Agency. **World energy outlook.** 2008.

JCPDS, **Power diffraction file search manual.** International Center for Diffraction Data: Pennsylvania, 1981.

KAMARKAR, R., DUTTA, T., LEBOVKA, N., TARAFDAR, S., **Effect of surface roughness on the bulk properties of simulated pore media.** Physica A, 348, 236 – 244, 2005.

KRAVCHENKO, A.G., MOIN, P., **Numerical studies of flow over a circular cylinder at Re_D = 3900.** Physics of Fluids, 12, 2, 403 – 417, 2000.

KNUDSEN, S., K., **Numerical Investigation of Ash Deposition in Straw – Fired Boilers – Using CFD as the Framework for Slagging and Fouling Predictions**. Doctoral thesis, Technology Institute of Energy, University of Aalborg, Denmark, 2001.

LEE, F.C.C., LOCKWOOD, F.C., **Modelling ash deposition in pulverized coal fired applications.** Progress in Energy and Combustion Science, 25, 117 – 132, 1999.

LESIEUR M., MÉTAIS O., COMTE P., **Large eddy simulations of turbulence.** Cambridge, Cambridge University Press, 2005.

LILLY D.K., **A proposed modification of the Germano subgrid scale closure method.** Physics of Fluids A, 4, 633 – 635, 1992.

LIANG C., PAPADAKIS G., **Large eddy simulation of pulsating flow over a circular cylinder at a subcritical Reynolds number.** Computers and fluids, 36, 2, 299 – 312, 2007.

LÜBCKE H., SCHMIDT St., RUNG T., THIELE F., **Comparison of LES and RANS in bluff body flow.** Journal of Wind Engineering and Industrial Aerodynamics, 89, 1471 – 1485, 2001.

MA, X., KARAMANOS, G.S., KARNIADAKIS, G.E., **Dynamics and low dimensionality of a turbulent near wake.** J. Fluid Mech. 40, 29 – 65, 2000.

MANDELBROT, B., **Objectos fractais.** Ciência Aberta Gradiva Publisher, Lisboa, Portugal, 1998.

MENDES, L.J.N., AZEVEDO, J.L.T., BAZZO, E., **A RANS analysis of the ash particle deposition around a boiler superheater tube.** 9th International Conf. on Energy for a Clean Environment, Póvoa de Varzim, Portugal, July, 2007.

MIT, Massachusetts Institute of Technology, **The future of coal, an interdisciplinary study MIT study.** 2007.

McLAUGHLIN, J.B., **Aerosol particle deposition in numerically simulated channel flow.** Physics of Fluids A, 1, 1211 – 1224, 1989.

ONG, L., WALLACE, J., **The velocity field of the turbulent very near wake of a circular cylinder.** Exp. Fluids, 20, 441 – 453, 1996.

PANTON, R.L., **Incompressible Flow.** Wiley Publisher, 2005.

PATANKAR, S.V., **Numerical heat transfer and fluid flow.** Hemisphere Publishing Corporation, 1980.

PHILIPPI, P.C, *et al* **Characterization of Reservoir Rocks from Image Analysis on Software IMAGO**, Proceeding of the Workshop on Subgrid modelling, Image and Visualization Recope/FINEP Informatics Aplication on Engineering, pp 32 – 36, 2000.

PIOMELLI, U. and BALARAS, E., **Wall Layer models for large eddy simulations.** Annu. Rev. Fluid Mech, 34, 349 – 374, 2002.

POPE, S.B. **Turbulent Flows.** Cambridge, Cambridge University Press, 2000.

REINALDO, R.F. **Estudo numérico de transferência de calor e deposição de cinzas em caldeiras de carvão pulverizado.** Doctoral thesis in Mechanical Engineering, Federal University of Santa Catarina, Florianópolis, Brazil, in Portuguese, 2004.

REINALDO, R.F., BAZZO, E., AZEVEDO, J.L.T.. **CFD Based analysis of heat transfer in a front wall pulverized coal fired boiler including superheaters.** International Journal on Energy for a Clean Environment, 6, 4, 409 – 421, 2005.

REZAEI, H.R., *et al*. **Thermal conductivity of coal ash and slags and models used.** Fuel 79, 1697 – 1710, 2000.

SHARIPOV F., KALEMPA, D., **Velocity slip and temperature jump coefficients for gaseous mixtures IV. Temperature jump coefficient.** Int. J. of Heat and Mass Transfer, 48, 1076 – 1083, 2005.

SHARIPOV, F., **Personal communication.** 2007.

SHIROLKAR, J.S., COIMBRA, C.F.M., McQUATY, Q., **Fundamental aspects of modelling turbulent particle dispersion in dilute flows.** Prog. Energy Combust. Sci. 22, 363 – 399, 1996.

SIEGEL, R., HOWELL J.R., **Thermal radiation heat transfer.** Taylor and Francis Publisher, New York, 2001.

SILVA, C.F.N.B. **The role of coherent structures in the control and interscale interactions of round, plane and coaxial jets.** Doctoral thesis in Mechanical Engineering, Grenoble Institute of Technology, Grenoble, France, 2001.

SILVA A.P.F., MENUT P.P.P., SU J. (Ed.). **Turbulência: Anais da I escola de primavera em transição e turbulência.**, Rio de Janeiro, ABCM Publisher, in Portuguese, 2002.

SILVA, R.C., **Arranjo instrumental para monitorar temperaturas de superfície em feixes tubulares de unidades geradoras de vapor.** Master thesis in Mechanical Engineering, Federal University of Santa Catarina, Florianópolis, Brazil, in Portuguese, 2008.

SONG, H., *et al*. **Fractal characteristic of three Chinese coals.** Fuel, 83, 1307 – 1313, 2004.

STREETER V.L., WYLIE E.B., **Mecânica dos Fluidos.** São Paulo, McGraw Hill Publisher, in Portuguese, 1982.

TALBOT, L., CHENG, R.K., SCHEFER, R.W., WILIS, D.R., **Thermophoresis of particles in a heated boundary layer.** J. Fluid Mech. 101, 737 – 758, 1980.

TOMECZEK, J., PALUGNOIK, H., OCHMAN, J., **Modelling of deposits formation on heating tubes in pulverized coal boilers.** Fuel, 83, 213 – 221, 2004.

TURNS, S.R., **An Introduction to Combustion: Concepts and Applications.** McGraw Hill Publisher, 2000.

WALL, T.F., BECKER, H.B., **Total absorptivities and emissivities of particulate coal ash from spectral band emissivity measurements.** Journal of Engineering for Gas Turbine and Power, 106, 771 – 776, 1984.

WALL, T.F., BHATTACHARYA, S.P., ZHANG, D.K., GUPTA, R.P., HE, X., **The properties and thermal effects of ash deposits in coal fired furnaces.** Prog. Energy Combustion, 19, 487 – 504, 1993.

WANG, T., SQUIRES, K., **Large eddy simulation of particle deposition in a vertical channel flow.** Int. J. Multiphase Flow, 22, 667 – 683, 1996.

WANG, M., WANG, J., PAN, N., CHEN, S., HE, J., **Three-dimensional effect on the effective thermal conductivity of porous media.** J. Phys D: Appl Phys, 40, 260 – 265, 2007.

WANG, H., WEST, J., HARB, J., **Microanalytical characterization of slagging deposits from a pilot scale combustor.** Energy and Fuels, 13, 3, 570 – 578, 1999.

WHITE, F. **Fluid Mechanics**, MacGraw-Hill Publisher, 2002.

WILLIAMSON, C.H.K., **Vortex dynamics in the cylinder wake.** Annual Review Fluid Mechanics, 28, 477 – 539, 1996.

XU, L., ZHANG, D., XIAN, X., **Fractal dimensions of coals and cokes.** J. Colloid Interface Science, 190, 357 – 359, 1997.

YAN, L., GUPTA, R.P., WALL, T.F., **The implication of mineral coalescence behavior on ash formation and ash deposition during pulverized coal combustion.** Fuel, 80, 1333 – 1340, 2001.

ZHENG, F., **Thermophoresis of spherical and non spherical particles: a review of theories and experiments.** Adv. Colloid Interf. Science. 97, 255 – 278, 2002.

APPENDIX A1 - FILTERING

On the Large Eddy Simulation approach, the Navier Stokes equations are filtered in the space via a low pass filtering operation, resulting in a filtered velocity field $\bar{\mathbf{U}}(\mathbf{x},t)$. Low pass filter is a filter that passes low frequency signals but attenuates (reduces the amplitude of) signals with a frequency higher than the cut-off frequency. In the LES case, the low frequency signals are from the large scales, Fig. A1.

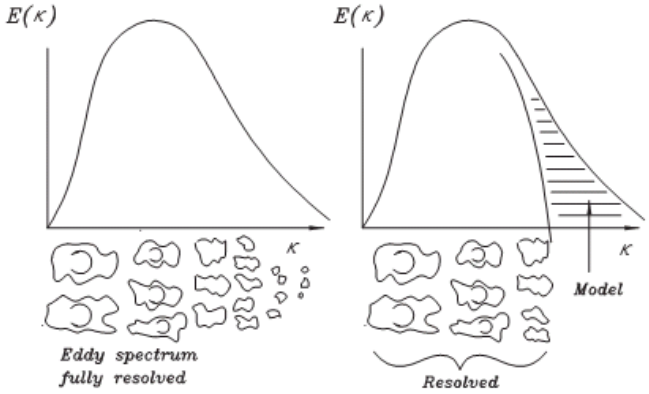

Figure A1.1 – A sketch of resolved energy spectrum for DNS and LES, Hanjalić (2005).

The filtering can be defined as a decomposition of the velocity $\mathbf{U}(\mathbf{x},t)$ into the sum of a filtered (or resolved) component $\bar{\mathbf{U}}(\mathbf{x},t)$ and a residual (or subgrid scale SGS) component $\mathbf{u}'(\mathbf{x},t)$.

The decomposition used in LES is analogous to the one used in the Reynolds Average approach, in which the characteristics of the flow field can be described in an average and fluctuation component. The difference remains on the average of the fluctuation component, on the Reynolds Average approach $\overline{u'}=0$, but the filtered residual (in general) $\overline{u'}\neq 0$.

The filtering operation is defined by a convolution integral given by:

$$\bar{\mathbf{U}}(\mathbf{x},t) = \int G(\mathbf{r},t)\,\mathbf{U}(\mathbf{x}-\mathbf{r},t)\,d\mathbf{r} \tag{A1.1}$$

where integration is over the entire flow domain, and the specified filter function, G, satisfies the normalization condition:

$$\int G(\mathbf{r},t) = 1 \tag{A1.2}$$

It is convenient to study the filtering process in the spectral space using Fourier transforms defined as:

$$\hat{U}(\kappa) = \Im\{U(x)\} = \frac{1}{2\pi}\int U(x)\,e^{-i\kappa x}\,dx \tag{A1.3}$$

Then the Fourier transform of the filtered velocity is:

$$\hat{\bar{U}}(\kappa) = \Im\{\bar{U}(x)\} = \hat{G}(\kappa)\,\hat{U}(\kappa) \tag{A1.4}$$

where the transfer function, $\hat{G}(\kappa)$, is 2π times the Fourier transform of the filter.

The filter used in spectral space is the cut off filter, which filters out all scales with a wavenumber larger than the cut off wavenumber $\kappa_C = \pi/\Delta$. This is defined as:

$$\hat{G}(\kappa) = \begin{cases} 1 \text{ if } \kappa < \kappa_C \\ 0 \text{ otherwise} \end{cases} \tag{A1.5}$$

However, in finite volume methods, box filters (volume filter) are always used, which filter out fluctuations in space with scales smaller than Δ:

$$G(x) = \begin{cases} 1/\Delta \text{ if } x < \Delta/2 \\ 0 \quad \text{otherwise} \end{cases} \tag{A1.6}$$

Furthermore, the filtering is implicit in the finite volume methods, which means that the filtering is the same as the discretization.

It is worth noting the behavior of the box filter in the spectral space:

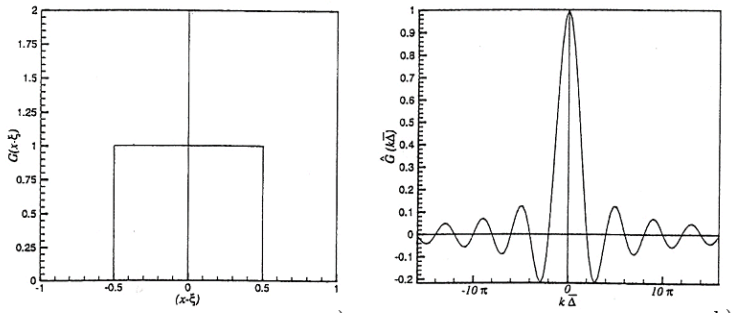

Figure A1.2 – Box filter: a) Physical space representation, b) Fourier space representation. Silva (2001).

Looking at the box filter in the Fourier space, we can see that it is local in physical space, but non local in the Fourier space. The spectral cut-off has an opposite behavior. As stated by Silva (2001), it is important to realize that the spectral cut-off is the only filter that separates unambiguously high/low frequencies. With the box filter, the separation of scales is not perfect, for example, for the large scales part there will be a major contribution from the low frequencies but also a smaller contribution from the high frequencies. The smaller scales, on the other hand, will be made by a major contribution from the high frequencies and a small contribution from the low frequencies.

The filtering and differentiating with respect to time commutes to:

$$\frac{\partial \overline{\mathbf{U}}}{\partial t} = \frac{\partial}{\partial t}\int G(r,\mathbf{x})\,\mathbf{U}(\mathbf{x}-r,t)\,dr \qquad (A1.7)$$

The Leibnitz rule has to be applied to commute the temporal derivative term inside the volume average operator as follows:

$$\frac{\partial}{\partial t}\int G(r,\mathbf{x})\,\mathbf{U}(\mathbf{x}-r,t)\,dr = \int \frac{\partial}{\partial t} G(r,\mathbf{x})\,\mathbf{U}(\mathbf{x}-r,t)\,dr = \overline{\frac{\partial \mathbf{U}}{\partial t}} \qquad (A1.8)$$

Analogous to the time derivative, a spatial derivative relation is obtained by:

$$\frac{\partial \overline{U}_i}{\partial x_j} = \int G(r,x)\frac{\partial U_i(x-r,t)}{\partial x_j}dr + \int U_i(x-r,t)\frac{\partial G(r,x)}{\partial x_j}dr \qquad (A1.9)$$

$$\frac{\partial \overline{U}_i}{\partial x_j} = \overline{\frac{\partial U_i}{\partial x_j}} + \int U_i(x-r,t)\frac{\partial G(r,x)}{\partial x_j}dr \qquad (A1.10)$$

As can be seen in Eq. (A1.10) the filtering and differentiation related to position do not commute in general, but do so for homogeneous filters (invariant with time and space), this is the case for box filter applied in the finite volume method. It is worth noting that in the case of non-uniform filter, for box filter, there is a second order error involved in the commutation of the filtering process and the spatial derivative, Ghosal and Moin (1995).

APPENDIX A2 - DYNAMIC MODEL

A2.1 Dynamic Model

In the model proposed by Germano (1991) and Lilly (1992), the coefficient of proportionality is not a constant, but is a function of time and space. The dynamic procedure involves different filter widths. The *grid filter* has a filter width $\overline{\Delta}$, which is proportional to the grid spacing, and the *test filter* with filter width $\tilde{\Delta}$, which is typically taken to be twice $\overline{\Delta}$. The operation of grid filtering is denoted by an overbar and the test filtering is denoted by a tilde. The description below follows Silva (2002), Pope (2000), Germano (1991) and Lilly (1992) description.

Filtering the Navier Stokes with a grid filter leads to:

$$\frac{\partial \overline{U}_j}{\partial t} + \frac{\partial\left(\overline{U_i U_j}\right)}{\partial x_i} = \nu \frac{\partial^2 \overline{U}_j}{\partial x_i \partial x_j} - \frac{1}{\rho}\frac{\partial \overline{p}}{\partial x_j} \tag{A2.1}$$

where $\tau_{ij}^R = \overline{U_i U_j} - \overline{U}_i \overline{U}_j$, which results in:

$$\frac{\partial \overline{U}_j}{\partial t} + \frac{\partial\left(\overline{U}_i \overline{U}_j\right)}{\partial x_i} = \nu \frac{\partial^2 \overline{U}_j}{\partial x_i \partial x_j} - \frac{1}{\rho}\frac{\partial \overline{p}}{\partial x_j} - \frac{\partial \tau_{ij}^R}{\partial x_i} \tag{A2.2}$$

Now filtering Eq. A2.1 with a filter width of $\tilde{\Delta}$ leads to:

$$\frac{\partial \tilde{\overline{U}}_j}{\partial t} + \frac{\partial\left(\widetilde{\overline{U_i U_j}}\right)}{\partial x_i} = \nu \frac{\partial^2 \tilde{\overline{U}}_j}{\partial x_i \partial x_j} - \frac{1}{\rho}\frac{\partial \tilde{\overline{p}}}{\partial x_j} \tag{A2.3}$$

where $T_{ij}^R = \widetilde{\overline{U_i U_j}} - \tilde{\overline{U}}_i \tilde{\overline{U}}_j$, which results in:

$$\frac{\partial \tilde{\overline{U}}_j}{\partial t} + \frac{\partial\left(\tilde{\overline{U}}_i \tilde{\overline{U}}_j\right)}{\partial x_i} = \nu \frac{\partial^2 \tilde{\overline{U}}_j}{\partial x_i \partial x_j} - \frac{1}{\rho}\frac{\partial \tilde{\overline{p}}}{\partial x_j} - \frac{\partial T_{ij}}{\partial x_j} \tag{A2.4}$$

Now applying the filtering operation with filter width $\tilde{\Delta}$ in Eq A2.2 leads to:

$$\frac{\partial \overline{U}_j}{\partial t} + \frac{\partial\left(\widetilde{\overline{U}_i}\,\tilde{\overline{U}}_j\right)}{\partial x_i} = \nu \frac{\partial^2 \tilde{\overline{U}}_j}{\partial x_i \partial x_j} - \frac{1}{\rho}\frac{\partial \tilde{\overline{p}}}{\partial x_j} - \frac{\partial \widetilde{\tau_{ij}^R}}{\partial x_i} \tag{A2.5}$$

Subtracting Eq . A2.4 from A2.5 results in:

$$L_{ij} \equiv \widetilde{\overline{\overline{U}_i}\,\overline{\overline{U}_j}} - \overline{\overline{\overline{U}_i}}\,\overline{\overline{\overline{U}_j}} = T_{ij} - \widetilde{\tau_{ij}^R} \qquad \text{(A2.6)}$$

This identity is known as Germano's identity, also known as resolved stress. In order to obtain the Smagorinsky coefficient, it is necessary to model the residual stress tensor from each filter width. Here the Boussinesq hypothesis is, also, used. The deviatoric part of τ_{ij}^R can be written:

$$\tau_{ij}^r = \tau_{ij}^R - \frac{1}{3}\delta_{ij}\tau_{ij}^R = -2c\overline{\Delta}^2 \left|\overline{S}\right| \overline{S}_{ij} \qquad \text{(A2.7)}$$

where $\left|\overline{S}\right| = \sqrt{2\overline{S}_{ij}\overline{S}_{ij}}$. The Smagorinsky coefficient is defined as c, instead of C_S^2 to allow for possible negative values, corresponding to backscatter. The same model equation is written for the filter width $\overline{\overline{\Delta}}$:

$$T_{ij}^r = T_{ij} - \frac{1}{3}\delta_{ij}T_{ij} = -2c\overline{\overline{\Delta}}^2 \left|\overline{\overline{S}}\right| \overline{\overline{S}}_{ij} \qquad \text{(A2.8)}$$

where $\left|\overline{\overline{S}}\right|$ is the rate of strain based on $\overline{\overline{U}}$. Taking c to be uniform and defining:

$$M_{ij} = \overline{\overline{\Delta}}^2 \left|\overline{\overline{S}}\right| \overline{\overline{S}}_{ij} - \overline{\Delta}^2 \widetilde{\left|\overline{\overline{S}}\right| \overline{\overline{S}}}_{ij} \qquad \text{(A2.9)}$$

Filtering Eq. A2.7 with filter width $\widetilde{\Delta}$ and subtracting from equation A2.8 lead to

$$L_{ij}^S = T_{ij}^r - \widetilde{\tau_{ij}^r} = -2cM_{ij} \qquad \text{(A2.10)}$$

Which is the deviatoric part of L_{ij}, Eq. A2.6

$$L_{ij}^r = L_{ij} - \frac{1}{3}\delta_{ij}L_{ij} \qquad \text{(A2.11)}$$

This information can be used to determine the value of the Smagorinsky coefficient for which the model L_{ij}^S provides the best approximation to L_{ij}^r, as shown by Lilly (1992), the mean square error is minimized in order to obtain the function of the Smagorinsky coefficient.

Defining

$$Q = \left(L_{ij} - \tfrac{1}{3}\delta_{ij}L_{ij} + 2cM_{ij}\right)^2 \qquad \text{(A2.12)}$$

Upon setting $\partial Q/\partial c = 0$, c is evaluated as

$$c = -\frac{1}{2}\frac{L_{ij}M_{ij}}{M_{ij}M_{ij}} \tag{A2.13}$$

This represents the minimum of Q, since $\partial^2 Q/\partial c^2 > 0$. Note that the isotropic term $1/3\delta_{ij}L_{ij}$ does not appear in the numerator of A2.13 because $\bar{S}_{ii} = 0$ in an incompressible flow.

APPENDIX A3 - BOUNDED CENTRAL DIFFERENCING SCHEME

The bounded central differencing scheme is essentially based on the normalized variable diagram (NVD) approach, Leonard (1991), together with convection boundedness criterion (CBC), Gaskell and Lau (1988). According to FLUENT (2007), the bounded central differencing scheme is a composite NVD scheme that consists of a pure central differencing, a blended scheme of the central differencing and the second-order upwind and first-order upwind schemes. It should be noted that the first-order scheme is used only when the CBC is violated. The bounded central differencing scheme is the default convection scheme for LES. Only the Normalized Variable Diagram and some aspects of the Convection Boundedness Criterion are described here. No information is available about how the central differencing and the second order upwind scheme used in FLUENT are blended. For more details, refer to the work of Leonard (1991) and Gaskell and Lau (1988).

A3.1 Normalized Variable Diagram (NVD)

In the NVD the variables are transformed into normalized variables defined by:

$$\tilde{\phi}(x,t) = \frac{\phi(x,t) - \phi_U}{\phi_D - \phi_U} \qquad \text{(A3.1)}$$

where ϕ_D is the downstream value, ϕ_U is the upstream value and ϕ_C is centrally located between the other two as shown in Fig A3.1.

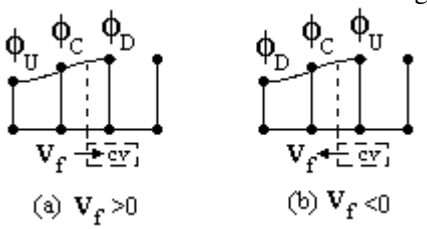

Figure A3.1 – Definition of Upstream (U), Downstream (D) and Central (C) node values, depending on the sign of v_f, Leonard (1991).

Note that with this normalization, $\tilde{\phi}_U = 0$ and $\tilde{\phi}_D = 1$. The use of the normalized variable simplifies the definition of the functional

relationships of high resolution schemes. For example, the QUICK scheme for steady flow is given by:

$$\phi_f = \frac{1}{2}(\phi_C + \phi_D) - \frac{1}{8}(\phi_D - 2\phi_C + \phi_U) = \frac{3}{8}\phi_D + \frac{3}{4}\phi_C - \frac{1}{8}\phi_U \qquad \text{(A3.2)}$$

Using the normalization proposed in A3.1 in A3.2:

$$\tilde{\phi}_f = \frac{3}{8} + \frac{3}{4}\tilde{\phi}_C \qquad \text{(A3.3)}$$

Some numerical schemes are given in the Tab. A3.1 according to the normalization A3.1

Tab. A3.1 – Normalized relationship for different numerical schemes.

Scheme	Functional Relationship	Normalized Relationship
First Order Upwind	$\phi_f = \phi_C$	$\tilde{\phi}_f = \tilde{\phi}_C$
Second Order Upwind	$\phi_f = \frac{3\phi_C - \phi_U}{2}$	$\tilde{\phi}_f = \frac{3}{2}\tilde{\phi}_C$
Second Order Central	$\phi_f = \frac{\phi_D + \phi_C}{2}$	$\tilde{\phi}_f = \frac{1 + \tilde{\phi}_C}{2}$
QUICK	$\phi_f = \frac{3}{8}\phi_D + \frac{3}{4}\phi_C - \frac{1}{8}\phi_U$	$\tilde{\phi}_f = \frac{3}{8} + \frac{3}{4}\tilde{\phi}_C$

The normalized variable diagram is shown in Fig A3.2 for the normalized relationship described in Tab A3.1.

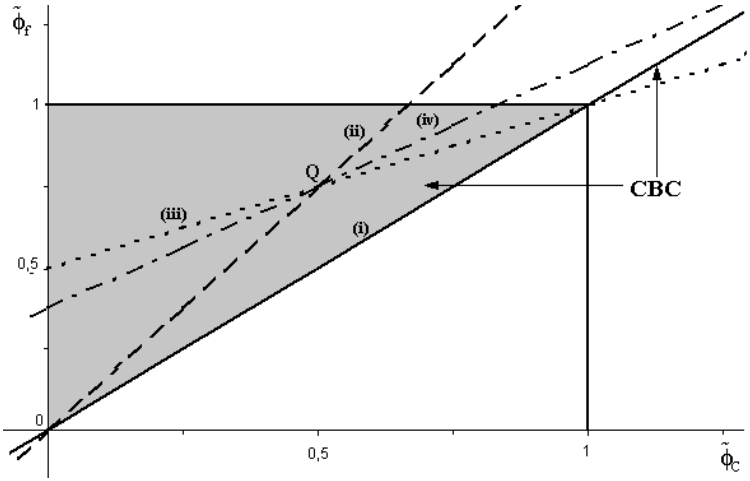

Figure A3.2 – Normalized variable diagram $\tilde{\phi}_f$ as a function of $\tilde{\phi}_C$ for the numerical schemes described in Tab A3.1, also it is represented the Convection Boundedness Criterion. (i) First Order Upwind; (ii) Second Order Upwind; (iii) Second Order Central and (iv) QUICK

Leonard (1991) has shown that any scheme that passes through the point Q in Fig A3.2 is at least second order accurate.

The Convection Boundedness Criterion (CBC) is defined for a continuous function relating the modeled normalized face value, $\tilde{\phi}_f$, in accordance to Eq. A3.1. The CBC states that for a scheme to have a boundedness property, its functional relationship should be continuous and bounded from below by the first order upwind, from above by unity and passes through the points (0,0) and (1,1) in the range of $0 < \tilde{\phi}_C < 1$. Also, for $\tilde{\phi}_C > 1$ or $\tilde{\phi}_C < 0$ the functional relationship should be equal to $\tilde{\phi}_C$, Gaskell and Lau (1988). If this criterion is satisfied in every point of the domain, the entire solution will be free of non physical oscillations.

The various straight lines in Fig. A3.2 represents the basic schemes. Clearly only the first order upwind satisfies the CBC and only a non linear function in the NVD can represent a bounded scheme of order higher than unity.

APPENDIX A4 - HEAT TRANSFER WITH MODIFIED BOUNDARY CONDITIONS

Gas rarefaction is taken into account through the temperature jump boundary condition for Kn ≈ 1, where the rarefaction effects cannot be neglected and the solution of the Boltzmann equation can still be avoided. As shown by Sharipov and Kalempa (2005), the temperature of the gas near the surface, for Kn = 0.23, can be calculated by:

$$T_g = T_w + \zeta_T \frac{\mu}{p}\left(\frac{2\kappa_B T_w}{M}\right)^{1/2} \left.\frac{\partial T_g}{\partial x}\right|_{x=0} \qquad \text{(A4.1)}$$

where x is the coordinate normal to the surface directed towards the gas with origin at the surface, μ is the viscosity of the gas, p is the local pressure, M is the molecular mass of the gas, κ_B is the Boltzmann constant, ζ_T is the temperature jump coefficient, T_w is the surface temperature and T_g is the gas temperature near the surface.

In order to get into the effects of the gas rarefaction, a thin gas layer between two boundaries at T_1 and T_2, Fig A4.1 is considered

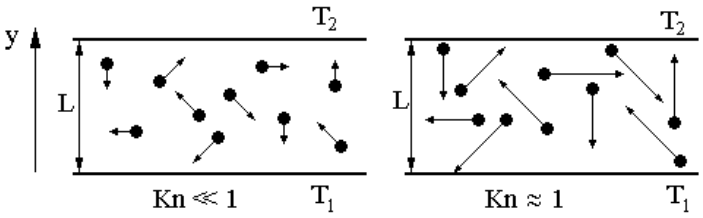

Figure A4.1 – Thermal conduction of a thin layer for $\mathrm{Kn} \ll 1$ (hydrodynamic regime) and $\mathrm{Kn} \approx 1$ (rarefaction regime).

The difference between the two cases illustrated in Fig A4.1 is for instance the low pressure for the rarefaction regime. For one dimension with no energy generation, under a steady state condition with a constant thermal conductivity, the energy equation is reduced to:

$$\frac{d}{dy}\left(\frac{dT}{dy}\right) = 0 \qquad \text{(A4.2)}$$

That reads as:

$$T = Ay + B \tag{A4.3}$$

This approach can be applied to both regimes and the only difference relays on the boundary condition. For the hydrodynamic regime, the boundary conditions are:

$$\begin{aligned} &y = 0; \quad \rightarrow \quad T_H = T_1 \\ &y = L; \quad \rightarrow \quad T_H = T_2 \end{aligned} \tag{A4.4}$$

Resulting in:

$$T_H = \left(\frac{T_2 - T_1}{L} \right) y + T_1 \tag{A4.5}$$

where T_H is the temperature distribution in the hydrodynamic regime. For the case of rarefaction the modified boundary conditions are:

$$\begin{aligned} &y = 0; \quad \rightarrow \quad T_R = T_1 + \zeta_T \lambda_L \frac{dT_R}{dy} \\ &y = L; \quad \rightarrow \quad T_R = T_2 - \zeta_T \lambda_L \frac{dT_R}{dy} \end{aligned} \tag{A4.6}$$

where T_R is the temperature in the rarefaction regime and λ_L stands for a quantity of order of the mean free path defined as:

$$\lambda_L = \frac{\mu \nu_0}{p} \tag{A4.7}$$

And ν_0 is the most probable molecular velocity at the local temperature:

$$\nu_0 = \left(\frac{2\kappa_B T}{M} \right)^{1/2} \tag{A4.8}$$

From Eq. A4.3:

$$\frac{dT_R}{dy} = A \tag{A4.9}$$

Substituting Eq A4.9 in the boundary conditions A4.6, after some algebraic, the resulting temperature distribution is:

$$T_R = \frac{(T_2 - T_1) y + T_1 L}{L(1 + 2\zeta_T Kn)} + \frac{2LT_1 \zeta_T Kn + L\zeta_T Kn (T_2 - T_1)}{L(1 + 2\zeta_T Kn)} \tag{A4.10}$$

The numerator of the first term of the high hand side of Eq. A4.10 is the temperature distribution from the hydrodynamic regime, which after some simplifications results in:

$$T_R = \frac{T_H + \zeta_T Kn (T_2 + T_1)}{(1 + 2\zeta_T Kn)} \tag{A4.11}$$

And the effective thermal conductivity of the rarefaction media under T_1 and T_2 is:

$$-k_{eff}\frac{(T_2 - T_1)}{L} = -k_g \frac{dT_R}{dy} \tag{A4.12}$$

which results in:

$$\frac{k_{eff}}{k_g} = \frac{1}{1 + 2\zeta_T Kn} \tag{A4.13}$$

Figure A4.2 shows the temperature distribution of the thin layer under the hydrodynamic and rarefaction regime:

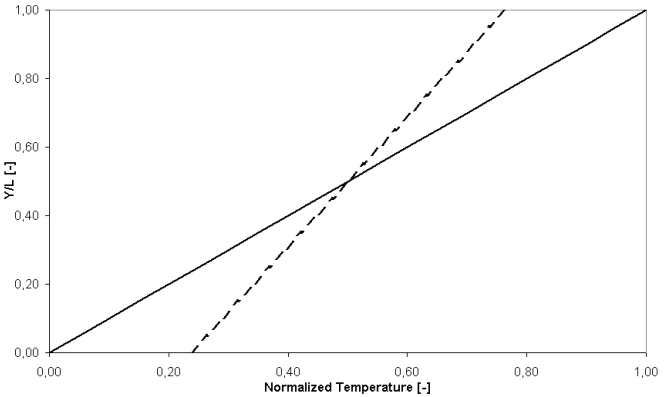

Figure A4.2 – Temperature distribution for different regimes, straight line for the hydrodynamic regime and dashed line for the rarefaction regime.

In Fig. A4.2 the temperature was normalized as:

$$T^* = \frac{T(y) - T_1}{T_2 - T_1} \tag{A4.14}$$

As shown in Fig. A4.2, the rarefaction jumps the gas temperature near the wall by lowering the heat flux under the same temperature difference. This influence is expressed in terms of an effective thermal conductivity from the Eq. A4.13.